Flow induced by collective vertical migration: impact of swimmer distribution, buoyancy, and wake interactions

Thesis by
Nina Mohebbi

In Partial Fulfillment of the Requirements for the
Degree of
Doctor of Philosophy

CALIFORNIA INSTITUTE OF TECHNOLOGY
Pasadena, California

2025
Defended 2025 May 27

Nina Mohebbi
ORCID: 0000-0003-4014-6111

ACKNOWLEDGEMENTS

ABSTRACT

Various animal species exhibit collective motion, characterized by coordinated movement within groups of organisms. One of the most prominent examples in the ocean is diel vertical migration (DVM), wherein zooplankton migrate from deeper waters during the day to shallower regions at night, often covering vertical distances of approximately 1 kilometer. Despite field measurements, laboratory observations, and theoretical estimates of biogenic mixing resulting from collective swimming, the scale of fluid mixing induced by DVMs remains unresolved. A key challenge is linking the behavior and flows created by large numbers of individual organisms to the collective-scale fluid dynamics. Because most swimmers involved with DVMs operate at intermediate Reynolds numbers, the dynamics of this system are nonlinear and encompass a wide range of spatiotemporal scales.

This thesis investigates the scaling of flows generated by vertical migration of brine shrimp (*Artemia salina*) aggregates and parameterizes them through a combination of laboratory measurements and semi-analytical modeling. First, a volumetric, laser scanning system measured swimmer behaviors and flow interactions during vertical migrations induced in a laboratory setting. Swimmers demonstrated consistent vertical swimming velocities in varying environmental conditions and exhibited a Gaussian distribution within the tank cross-section while displaying a tendency to move inward toward the center of the tank, where illumination was brightest. A scaling relationship between swimmer buoyancy, ascent speeds, and the resulting flow speed was developed to contextualize these results. Finally, a semi-analytical model was developed to estimate the flow generated by the wakes of multiple swimmers in proximity. The behaviors of individual swimmers were informed by the empirical results of the previous section and superposed using an iterative method that conserves mass and momentum to solve for the aggregation-scale flow. Numerical results suggested that the induced flow upstream in the aggregation was insensitive to the presence of downstream swimmers, the average flow speed tended to reach a plateau beyond a threshold aggregation length, and that closer swimmer spacing led to higher induced flow speeds.

PUBLISHED CONTENT AND CONTRIBUTIONS

[1] N. Mohebbi, J. Hwang, M. Fu, and J. Dabiri. "Measurements and modelling of induced flow in collective vertical migration". In: *Journal of Fluid Mechanics* 1001 (2024). *N.M., J.H., M.K.F., and J.O.D. designed research and were involved in discussions to interpret the results; N.M. performed research and analyzed results; M.K.F. developed the method and original analysis; J.H. wrote software and analyzed data; N.M. drafted the paper, and all authors helped edit and review.*, A50. DOI: 10.1017/jfm.2024.1102.

TABLE OF CONTENTS

LIST OF ILLUSTRATIONS

LIST OF TABLES

Chapter 1

INTRODUCTION

"The behavior of large and complex aggregates... is not to be understood by simple extrapolation... Instead, at each level of complexity entirely new properties appear."

– Philip W. Anderson, *More is different. Science, 1972*

1.1 Collective motion and emergent phenomenon

Many emergent properties and large-scale patterns of collective phenomena can only be fully appreciated at the collective level, where behavior and organization among individuals give rise to phenomena that do not and sometimes cannot exist in isolation. As systems scale up in complexity, new properties may emerge that cannot be predicted from individual behaviors alone [5].

Aggregations of animals display properties that are only meaningful at the collective level, such as predator avoidance, enhanced sensory integration, and emergent decision making [6]. The emergence and transition between collective and individual animal states have been modeled as analogous to phase transitions observed in equilibrium statistical physics due to the broken symmetry of the system, in which the underlying laws governing individual interactions are symmetrical, meaning that there is no preferred direction of motion in a group of animals, yet the system as a whole spontaneously adopts a specific organized state of direction [7]. For example, in a school of fish or a flock of birds, each individual initially does not have an intrinsic preference for a particular swimming or flying direction; this situation is perfectly symmetric. However, as individuals interact locally (aligning movements, responding to neighbors), a critical threshold or key interaction may exist at which the entire group will spontaneously move coherently in a single direction, thus "breaking" the original directional symmetry. This is analogous to how magnetic domains spontaneously align in a ferromagnet, even though the underlying atomic spins have no intrinsic directional bias until external or internal interactions push the system past a critical point.

In the aforementioned examples of schooling fish and flocking birds, the collective dynamics are significantly influenced by interactions with their fluid environment.

On the organismal scale, coordination is mediated by fluid signals, known as fluid stigmergy [8], and hydrodynamic advantages have been identified by which fish schools reduce energy expenditure by aligning their movements in specific formations to exploit wake interactions and vortex structures left by neighbors [9, 10].

Just as hydrodynamics on the organismal scale significantly influences collective behavior, these collective behaviors can have substantial effects on the surrounding fluid environment on the aggregation scale. Prairie et al. (2012) illustrate the interconnectedness between biological processes and physical oceanography, emphasizing that physical processes like turbulence and internal wave dynamics feed back to shape biological distributions and collective behaviors. Simultaneously, microscale biological activities, such as fluid disturbances generated by individual plankton, can scale upward, cumulatively affecting mesoscale mixing patterns and even large-scale ocean circulation processes, termed biogenic mixing. This integrated perspective underscores the necessity of adopting a multiscale framework to understand how organismal behaviors scale up to influence their fluid environment and how larger-scale physical processes shape organismal behavior.

The emergent hydrodynamics of collective motion affects flow-mediated communication [11], fluid transport in the ocean, and thus the distribution of nutrients, planktonic food webs and carbon cycling [12], and the hydrodynamic performance of collectives [9, 13]. The principles of these fluid mechanics have applications in control mechanisms for robotic swarms [14] and climate modeling [15].

1.2 Does Diel Vertical Migration mix the ocean?

Since early speculations in *Abyssal recipes* [16], the idea that biogenic mixing could be a significant input to ocean mixing has received high degrees of interest and skepticism [17–22].

One of the most common manifestations of collective behavior in the ocean is diel vertical migration (DVM). Prevalent among freshwater and marine zooplankton taxa globally, DVM involves the migration of zooplankton from deep regions in the water column during the day to shallower depths at night over a vertical distance on the order of 1 km. It is the largest migration on Earth by mass [23], however; the scale of flow induced by a DVM event remains unresolved despite numerous field measurements [20, 24–26], laboratory observations [22], and theoretical estimates [19, 20] of biogenic mixing due to collective swimming.

The energy produced during a DVM event could rival or complement other recog-

nized physical mixing mechanisms, such as tidal and wind-driven processes [20]. However, experimental validation is required to understand the parameters, on an individual and collective scale, that influence the aggregate induced flow.

The link between animal behavior (group organization, orientation, and swimming modes) and aggregation-scale flow is missing, and common modeling assumptions, such as isotropy and homogeneity of the system, do not accurately represent biological systems. To better understand this relationship, it will require both bottom-up approaches, which involve scaling individual animal fluid dynamics to larger aggregations, and top-down approaches, which are based on field measurements of these aggregations [12].

The field measurements required for a top-down approach are complex to disambiguate from background ocean turbulence and other mixing processes [27, 28], and therefore have been limited to unplanned chance encounters with dense aggregations [24, 29]. New strategies, such as measuring vertical flow currents in the Earth's geomagnetic field remotely, could increase the availability of vertical flow data [30] and improve the search for this connection.

In the bottom-up approach, bridging the gap between individual behavior and hydrodynamics with broader collective outcomes will require multidimensional, multiscale experimental methods. Such approaches will facilitate tracking animal behavior while capturing detailed measurements of the resultant flow fields.

1.3 Mulit-scale multi-dimensional approaches

The metrics used to characterize swimmer aggregations, such as packing density or average animal spacing, lack information about the spatial structure and distribution within the group. In addition, common analyses that quantify individual swimmer performance, such as thrust production, typically neglect detailed characterization of wake structures, such as the spatial structure, coherence, and persistence of individual wakes, which determine how these fluid disturbances interact with neighboring swimmers and consequently shape emergent collective-scale hydrodynamic behaviors. For a better understanding of the multiscale coupling between collectives and induced fluid dynamics, methods and models must move beyond these overgeneralized metrics and explicitly resolve spatial patterns, wake structures, and individual swimmer interactions.

Studies of individual organism flow include a comprehensive set of experimental [31, 32], theoretical [33, 34], and computational [35, 36] estimates. Flow mea-

surements around individual swimmers were traditionally limited to 2-dimensional (2-D) planar slices using techniques like particle image velocimetry (PIV). The evolution in both high-speed camera capabilities [37] and analysis methods [38, 39] has led to an increase in volumetric (3-D) flow measurements. The main techniques are synthetic aperture PIV [40, 41], tomographic PIV [42], and defocusing digital particle tracking velocimetry [43–45]. With a few exceptions [1, 46], these have mainly continued to focus on individual organism flows.

3-D direct numerical simulation (DNS) has been used to extrapolate the hydrodynamics of individual swimmers to the hydrodynamics of collective motion [47, 48]. However, the full hydodynamic interactions in many-body systems make simulations very computationally expensive and have restricted the number of swimmers to tens of swimmers (fewer at high Reynolds). Although DNS of large-scale events remains computationally intractable due to the necessary resolution and computational resources, GPU-accelerated CFD codes suggest that this could be on the horizon. Currently, reduced-order models may be more suitable for investigating collective swimmer dynamics. However, due to the nonlinear coupling between individual and collective flow fields at intermediate and high Reynolds numbers, connecting these individual flows to the fluid dynamics on the collective scale remains an open challenge using a modeling approach short of DNS.

Similarly to 3-D flow measurements, tracking the 3-D movements of aquatic animal swarms has received increased attention in recent years, driven by advances in digital imaging and computer vision [49–52]. Multicamera setups enable photogrammetric reconstruction of fish positions in 3-D. This method often uses two or more synchronized cameras from different viewpoints and can track tens of swimmers simultaneously. These methods have been extended to field settings and have been used to triangulate 3-D positions of animals in open water [53].

The simultaneous tracking of swimmers and their surrounding 3-dimensional fluid flows presents a considerable technical challenge in experimental fluid dynamics, constraining most studies to relatively small measurement scales.

Adhikari et al. [54] employed an advanced dual method system that integrated infrared tomographic particle image velocimetry (PIV) and visible-light 3-D particle tracking velocimetry (PTV) to investigate the interactions between zooplankton (copepods, Acartia tonsa, ~1 mm in size) and complex turbulent flows within a measurement volume of approximately 60 cm^3. Simultaneously, copepod trajectories and surrounding fluid velocities captured small-scale fluid deformation around

individual copepods (mm scale) and eddy structures in a turbulent wake behind a cylinder (cm scale). This method revealed distinct behavioral responses of copepods to different flow conditions: copepods executed escape jumps at moderate fluid strain rates in uniform, laminar flow, yet exhibited surprisingly passive behavior in a turbulent wake, even at much higher local strain rates. Furthermore, the study demonstrated significant inertial drift of copepods relative to passive fluid particles, emphasizing the importance of simultaneously tracking both swimmers and fluid to accurately interpret animal-fluid interactions.

Fu, Houghton, and Dabiri [1] uses a single-camera, 3-D scanning velocimetry approach by capturing sequentially illuminated image slices to reconstruct 3-dimensional swimmer morphologies (*Artemia salina*, 5–10 mm length) and trajectories alongside fluid velocity fields in a volume of about 50 cm^3. This scale of measurement enabled the resolution of coherent flow structures generated by individual swimmers and the centerline velocity of the aggregate scale flow produced by the collective. Notably, the approach was able to track swimmers in dense aggregations (up to $\sim 8 \times 10^5$ animals per m^3) despite the significant occlusions, complicating optical imaging and resulting in reconstruction artifacts that would be prohibitive in other methods.

1.4 Aims and objectives of the dissertation

The previous sections outline the various modeling, experimental, and analytical tools used to study induced flows in collective motion. However, significant questions remain regarding the reciprocal influence between organism-scale behaviors and larger aggregation-level flow dynamics. This dissertation aims to quantify how organism-scale behaviors and hydrodynamics affect the scaling of induced fluid flows during collective vertical migration, using an integrated approach combining experimental, theoretical, and semi-analytical methods.

Using 3-dimensional particle tracking velocimetry (PTV) and particle image velocimetry (PIV), chapter 2 quantifies the responses of individual brine shrimp (*Artemia salina*) to local flow conditions during their vertical migration. The distributions, trajectories, and local flow interactions of the swimmers show that these swimmers largely respond passively to the velocities of the surrounding fluid, with consistent and dominant upward swimming.

Chapter 3 examines the impact of changes in individual swimmer buoyancy on induced flow structures. This chapter combines empirical measurements with the-

oretical predictions derived from an actuator disk model, clarifying the physical mechanisms that connect variations in buoyancy to collective-scale hydrodynamics. Increased swimmer buoyancy significantly reduces induced flow velocities, which aligns closely with theoretical expectations calculated from an actuator disk model. This emphasizes how buoyancy-driven thrust generation at the organismal level can influence larger-scale flows.

Building upon these empirical insights, Chapter 4 presents a semi-analytical model to systematically predict collective-scale induced flows based on swimmer configurations and individual wake structures. By conserving mass and momentum within groups, this model establishes a framework for understanding how variations in swimmer spacing, group dimensions, and individual wake structures translate to aggregation-level flow dynamics. This chapter illustrates that induced flow velocities reach asymptotic levels beyond a certain aggregation length and that closer swimmer spacing significantly enhances flow speeds, potentially impacting aggregation stability.

The conclusions and implications of these studies, as well as potential opportunities for future research, are laid out in Chapter 5

Chapter 2

SWIMMER RESPONSE TO INDUCED FLOW

[1] N. Mohebbi, J. Hwang, M. Fu, and J. Dabiri. "Measurements and modelling of induced flow in collective vertical migration". In: *Journal of Fluid Mechanics* 1001 (2024). *N.M., J.H., M.K.F., and J.O.D. designed research and were involved in discussions to interpret the results; N.M. performed research and analyzed results; M.K.F. developed the method and original analysis; J.H. wrote software and analyzed data; N.M. drafted the paper, and all authors helped edit and review.*, A50. DOI: 10.1017/jfm.2024.1102.

ABSTRACT

This study explores the interactions between environmental factors and collective swimming behaviors in brine shrimp, *Artemia salina*, during induced vertical migration. Individual swimmers' time-resolved 3-dimensional spatial tracks and simultaneous 3-dimensional 2-component particle image velocimetry (PIV) were measured using a recently developed laser scanning system. Swimmers maintained stable relative vertical velocities despite variable flow conditions, indicating predominantly passive interactions with flow structures rather than active compensatory responses. An inward radial directional preference, likely driven by positive phototaxis, contrasts with a Gaussian spatial distribution, indicating a dynamic equilibrium between attractive and dispersive forces shaped by inter-individual interactions. Additionally, the swimmers' turning behavior demonstrated radial dependence, showing frequent reorientations and higher curvature in the center of the tank and lower curvature and thus smoother trajectories further from the center. Strong spatial correlations were observed between light intensity, vertical flow velocity, and swimmer concentration, complicating the analysis of these interactions.

2.1 Introduction

Previous research has explored how individuals within fish schools and other aquatic groups respond to hydrodynamic cues, focusing largely on 2-D experimental setups or 3-D numerical models. 2-D particle image velocimetry (PIV) has been used to measure wake interactions among schooling fish and has revealed local hydrodynamic benefits such as energy savings through vortex-mediated swimming [10]. Additionally, numerical and computational modeling has explored 3-dimensional wakes and collective swimming patterns, uncovering potential emergent structures such as coherent jets or large-scale vortex formations [55, 56]. However, these computational studies often lack direct empirical validation, especially at scales significantly larger than individual organisms. Empirical studies that incorporate 3-dimensionality have typically focused exclusively on swimmer positions without simultaneous fluid measurements [57], or measure flows within restricted spatial volumes on the order of a single individual [1, 43].

To address this limitation, we significantly expanded and adapted a 3-dimensional scanning method by Fu, Houghton, and Dabiri [1] to simultaneously track individual swimmers during an induced vertical migration of brine shrimp and measure the 3-dimensional (3-D) two-component flow induced by the migration using PIV. This experiment extends previous approaches to an observational volume 100 times larger. This allows direct measurement of large-scale flow features, such as coherent jets with a diameter of more than 20 body lengths, which have been found in experiments [22] and predicted by theory and simulations [56].

The swimmers are found to have exclusion zones of about 1 body length (BL) limiting the total packing of the swimmers. In addition, the swimmers were distributed throughout the tank in a 2-D Gaussian spread, a structure which was matched by the resulting flow induced by the swimmers. By capturing simultaneous individual swimmer trajectories and fluid flow, we find that swimmers do not adjust their vertical swimming speed in the face of oncoming flow or flow gradients. Finally, swimmers are found to change swimming pattern in the horizontal plane with changing radial distance from the center of the tank.

2.2 Experimental methods

General experimental setup

Experiments were conducted in a 1.2 m tall tank with a cross section of 0.5 m x 0.5 m (figure 2.1), filled with artificial seawater prepared using Instant Ocean Sea Salt

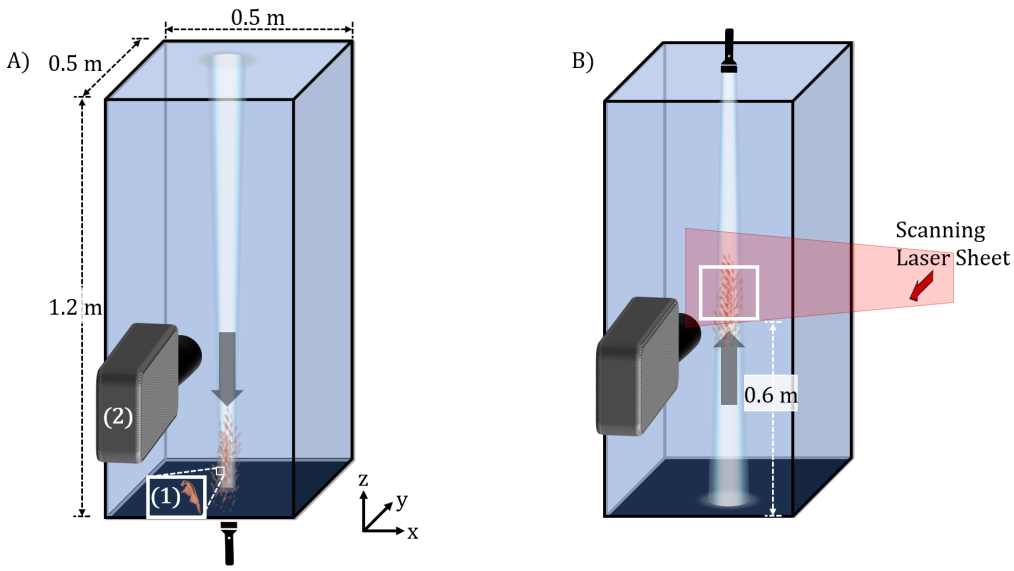

Figure 2.1: Schematic of experimental protocol for 3-dimensional scanning during induced vertical migration using the phototactic response of brine shrimp. A) Brine shrimp (1) were gathered at the bottom of a 1.2 m tall tank using a flashlight positioned at the base. B) To induce vertical migration, the bottom flashlight was turned off, and the top flashlight was turned on. A laser sheet sweeps through the depth of the tank progressively illuminating thin slices of the tank y dimension. A high speed camera is set-up to capture an x-z square halfway up in the tank.

(Spectrum Brands) and DeIonized (DI) water. Salinity ranges between 15 and 35 ppt are used throughout this work depending on the experiment type. The nominal thank temperature was 68°F (20°C) and insulating foam (closed-cell polyethylene foam, McMaster-Carr 9349K5, 0.5" thick, thermal conductivity $\approx$ 0.27 W/m·K) was added to the outer walls of the tank to limit heat exchange with the surrounding environment. The tank was also covered with an acrylic lid and the same insulating foam to reduce evaporative cooling at the surface and prevent other environmental temperature disturbances. Even modest temperature differences on the order of 2°F (1.1°C) can generate Rayleigh numbers that exceed the threshold for the onset of natural convection. To facilitate imaging of fluid flow, the tank was filled with 10 μm silver coated glass spheres (CONDUCT-O-FIL, Potters Industries, Inc.).

Animal preparation and induced vertical migration procedure

All experiments use *Artemia salina* (brine shrimp) and were carried out within 24 hours after the acquisition of the animals. Brine shrimp do not naturally inhabit oceanic environments but instead thrive in hypersaline inland habitats such as salt lakes, coastal lagoons, and brine pools [58]. Despite this ecological distinction, brine

shrimp are intermediate Reynolds-number swimmers, operating in a fluid dynamic regime similar to that of most zooplankton involved with diel vertical migration (DVM) [12], such as copepods and krill, which typically swim at Reynolds numbers between 1 and 1000. In addition, brine shrimp exhibit a strong positive phototaxis, or movement toward light sources, which enables controlled vertical migrations in laboratory settings. Brine shrimp are 1 cm long and we will often use this body length (BL= 1 cm) to normalize length measurements.

The animals were added to the tank in densely packed increments of 0.25 teaspoon (1.23 ml) (approximately 125 swimmers). Before starting each trial, the animals were gathered at the bottom of the tank using a flashlight. Brine shrimp are positively phototactic, which means that they are attracted to and will swim towards light. A minimum settling time of 15 minutes was allowed between each upward migration. Following the settling time, every 5 minutes the tank quiscence was evaluated by a 25 second video taken of the laser sheet illuminated tank. This was repeated until particle image velocimetry (PIV) analysis (PIVLab version 3.09 in Matlab) found that the maximum time-averaged vertical velocity was below 0.02 cm s^{-1} and thus was deemed quiescent. Once the tank was found to be quiscent, vertical migration was initiated by turning off the bottom flashlight and activating a top-positioned target flashlight (PeakPlus LFX1000, 1000 lumens), as illustrated in Figure 2.1.

The target flashlight creates a concentrated beam approximately 7 cm wide in the field of view of the camera. Although this spatially restricted illumination differs from the broad diffuse light gradients experienced in the open ocean, other environmental drivers of diel vertical migration, such as oxygen concentration, food availability, and predator presence, exhibit strong spatial and temporal patchiness [59, 60]. Therefore, the behavioral responses observed in these laboratory-controlled migrations may still provide valuable insights into how organisms respond to steep, localized resource gradients analogous to those found in stratified or patchy marine environments.

3-dimensional scanning setup

To reconstruct the 3-dimensional (3-D) swimming trajectories of brine shrimp during induced vertical migration, a 3-D particle tracking velocimetry (PTV) method was used (figure 2.2), using scanning optics and a single high-speed camera (Photron FASTCAM SA-Z). A 671 nm continuous wave laser (5 W Laserglow LRS0671 DPSS Laser System) was directed by a rotating mirror through a condenser lens (McMaster Carr 370 mm back focal length) and a sheet-forming glass rod to ensure

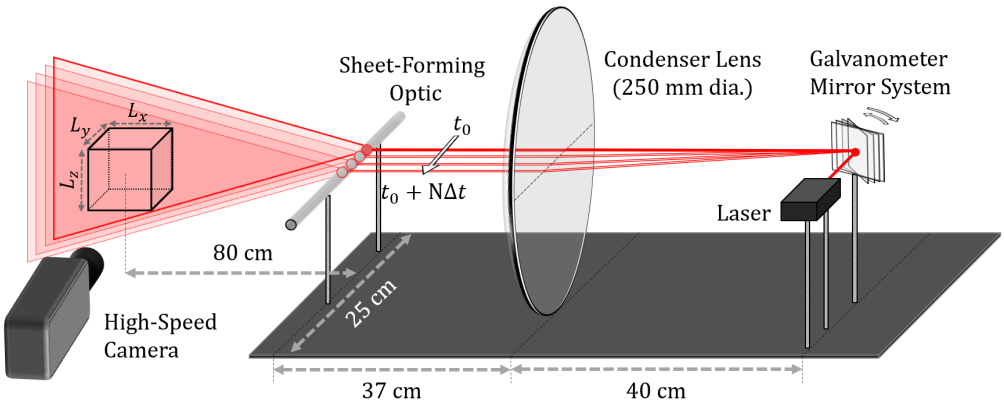

Figure 2.2: Schematic of the scanning system, modified from Fu, Houghton, and Dabiri [1]. The laser beam was directed at a mirror whose angle was controlled by a galvanometer. Following reflection by the mirror, the beam was passed through a condenser lens and glass rod in order to generate a laser sheet parallel to the camera field of view.

parallel beams. The distance between the laser plane and the high-speed camera was adjusted by rotating the mirror which was mounted on a galvanometer (Thorlabs GVS211/M) controlled by a voltage signal from an arbitrary function generator (Tektronix AFG3011C).

The system was validated and calibrated using a custom-fabricated 3-D calibration cube (UCrystal) containing a laser-engraved grid of 1.6 mm spherical markers spaced 1 cm apart in a 6×6×6 array, embedded in an 8 cm cube. The calibration cube was suspended in the imaging volume and scanned to generate 3-D image volumes, which were then processed in MATLAB. These known positions were then used to map image voxels to real-world coordinates, accounting for optical distortions.

This setup was previously validated in the same facility using a free laminar jet at Re = 50 compared to the direct numerical simulation of synthetic particle fields, confirming the system's ability to accurately resolve velocity fields Fu, Houghton, and Dabiri [1].

Experiment parameters

In setup A per table 2.1, each laser sheet sweep covered 6.6 cm of tank depth and took 0.1 seconds to complete. The high-speed camera captured 295 2-dimensional (2-D) 22 cm x 22 cm (1024 pixel x 1024 pixel) slices during this period. The scanned volume was centered on the tank cross section and was positioned 0.5 m from the tank floor. The swimmers move at approximately 1 cm s^{-1}; therefore, during the

duration of a scan (0.1 seconds), the swimmers will have moved approximately 0.1 cm. Given their body size of 1 cm, we effectively treated each scan as a still frame for the purposes of the current analysis. In addition, this combination of the scanning rate and the frame rate of the camera results in approximately 48 image sheets per cm in the scanning direction (y) and 48 pixels per cm in the camera plane (x and z). This level of resolution for detecting swimmers 1 cm long results in well-formed and easily identifiable swimmers, as shown in Figure 2.3A. A video of 3-D reconstructed swimmers for 6 seconds is in the supplementary materials. Three vertical migrations were induced for each test case. Throughout vertical migration, the center of the tank was scanned for 6 seconds every 50 seconds, totaling 7.5 minutes, to assess configuration changes over time. For setup A, the tank salinity is 30 ppt.

In setup B per table 2.1, each laser sheet sweep covered 10 cm of tank depth and took 0.2 seconds to complete. The high-speed camera captured 395 2-dimensional (2-D) 22 cm x 22 cm (1024 pixel x 1024 pixel) slices during this period. The scanned volume was located at the same location as Method A, and during the length of a scan (0.1 seconds), the swimmers will have moved approximately 0.2 cm. This combination of scanning rate and camera frame rate results in approximately 36 image sheets per cm in the scanning direction (y) and 36 pixels per cm in the camera plane (x and z). This results in lower resolution swimmers in the y-dimension but is enough to identify swimmer bodies. Three vertical migrations were induced for each test case. The volume was scanned for 43 seconds, 3 minutes after the start of the migration. For setup B, the tank salinity is 20 ppt.

	Recording length(s)	Capture rate(fps)	Depth (cm)	Scanning rate(Hz)	Scans/cm	Swimmers added(tbs)
A	6	3000	6.6	10	48	0.5–7
B	40	2000	11	5	36	12

Table 2.1: Settings used for two 3-D scanning experiments. Method A has better spatial and temporal resolution when compared to method B, while method B has a recording length 5 times longer than method A.

Data processing and analysis

A 3-D volume was constructed from the 2-D slices for each laser sweep (figure 2.3A). A custom MATLAB script was used to segment the 3-D volume and identify centroids. The volumetric data were median and Gaussian filtered to reduce noise

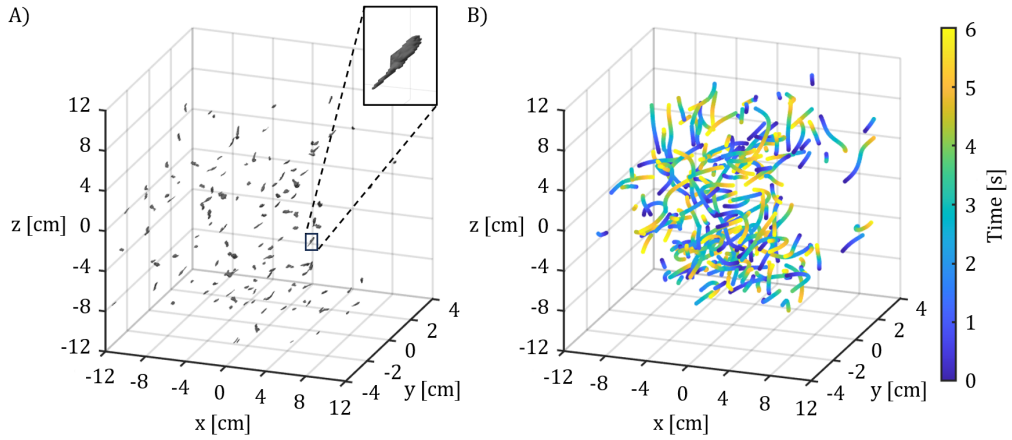

Figure 2.3: Volumetric (3-D) body reconstruction and animal tracking during an induced vertical migration in the positive z direction. A) 3-D scanned reconstruction of 100 animal bodies. A close-up of an individual animal shown for reference. B) Six-second 3-D swimming trajectories, with color transition from blue to yellow represent progression in time, illustrating the trajectory of each swimmer within the tank.

and enhance object visibility. The filtered data were then binarized and morphological operations were applied, including opening with a spherical structuring element and hole filling, to refine the binary mask. This preprocessing ensured a clean and noise-reduced dataset for object detection. Through object detection, properties such as centroid, principal axis, and volume were identified for each connected component within the volume. Subsequently, a forward and backward nearest neighbor search was applied in time to centroid locations to identify and label swimming trajectories (figure 2.3B).

2.3 Results

3-D sampling over migration duration time

From setup A in table 2.1 the components of the swimming velocity were computed by first calculating each swimmer's instantaneous velocity based on the trajectory data. The velocity was then averaged per individual swimmer over a maximum of 6.5 seconds of data recorded. Next, all swimmer velocity vectors were averaged across trials at each sample time spaced 45 seconds apart. The average velocity vector for each sample time is then normalized by the magnitude of the average velocity to arrive at the velocity cosines (2.4A). The results show that the swimmers have achieved highly directed vertical swimming by 96 seconds in the migration. In addition, the dominance of the positive z-component indicates a strong, consistent

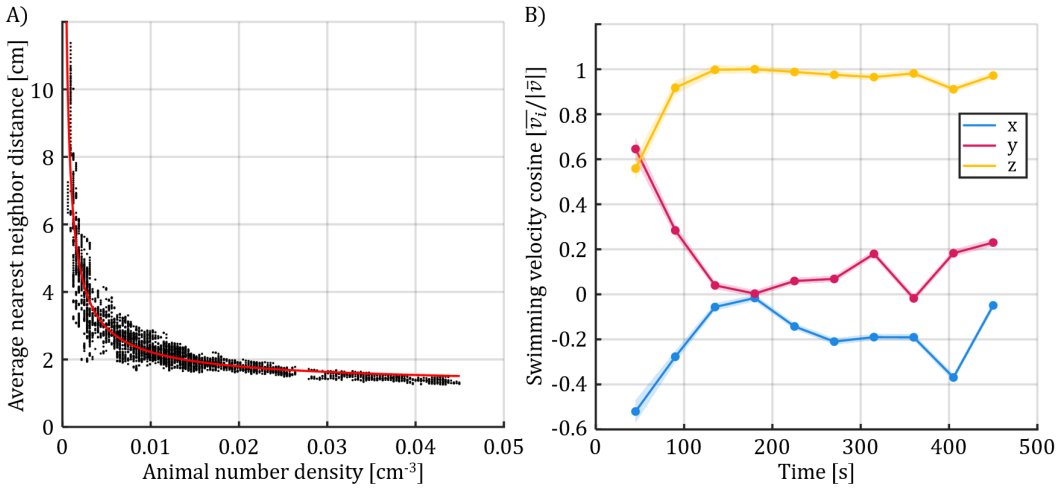

Figure 2.4: Data extracted from 3-D brine shrimp trajectories. A) Changes in average nearest neighbour distance during an induced vertical migration with increasing number of brine shrimp within the scanned volume. Power law best fit plotted in red, $y = 0.031x^{0.74} + 1.16$, with R^2 value of 0.85. B) Average swimming velocity components from brine shrimp trajectories over the course of an induced migration, with shaded areas representing the standard error. The target flashlight is located at positive z, above the tank.

upward motion among the swimmers towards the target flashlight (located at positive z). Thus, we may treat momentum addition entirely on the z -axis for modeling.

As the number of swimmers within the scanned volume increases, the average nearest neighbor distance decreases to an apparent limiting value, consistent with the presence of exclusion zones (figure 2.4B). The asymptotic average nearest neighbor distance at large animal number density is empirically estimated using a least-squares fit to a power-law relationship. The modeled power-law fit is calculated using $y = ax^b + c$, where x is the animal number density, y is the nearest neighbor distance, and a,b, and c are fitting parameters. The fit yielded an asymptotic value (c) of approximately 1.16 cm, corresponding closely to one swimmer body length. Given that the swimmers have an approximately elliptical cross-sectional shape, with a width around 0.5 cm, this nearest neighbor distance of approximately 1 cm represents a meaningful physical gap rather than merely a geometric inevitability. If swimmers were spherical and had a diameter close to 1 cm, maintaining a nearest neighbor distance of one body length would be trivial. However, due to their narrower elliptical shape, the observed exclusion zone of roughly one body length clearly indicates active spacing behaviors or hydrodynamic interactions rather than purely geometric constraints.

Simultaneous 3-D PIV and trajectory analysis
Spatial distribution of swimmers

Using the longer trajectories collected with set-up B in table 2.1, the spatial distribution of the swimmers was examined by analyzing their positions at the midpoint of each recorded trajectories, projected onto the horizontal (x-y) plane. Since swimmer trajectories vary in their start times, end times, and overall durations, this location data was extracted from different timesteps. The midpoint location was selected as a representative measure because simple time averaging or including all tracked points could bias toward slower swimmers or areas with increased background flow. The highest concentration of swimmers was found in the center of the tank, coinciding with the position of the target flashlight (figure 2.5).

To statistically assess whether the distribution of swimmer locations conforms to a known theoretical distribution, a Kolmogorov-Smirnov (KS) test [61] was used. The KS statistic is defined as the maximum distance between the empirical cumulative distribution function (CDF) and the CDF predicted by the theoretical distribution. The horizontal (x) and vertical (y) distributions of the swimmers exhibited strong statistical alignment with the Gaussian distribution, as indicated by the KS statistics of 0.0392 and 0.0347, and the p values of 0.1376 and 0.2421, respectively (figure 2.5). Alternative distributions—namely, lognormal, gamma, Weibull, and Nakagami—were rejected ($p < 0.05$), further reinforcing the appropriateness of the Gaussian distribution for characterizing swimmer positions.

The fitted Gaussian distributions produced spatial standard deviations in x and y of $\sigma_x = 3.73$ cm and $\sigma_y = 2.47$ cm, along with the corresponding center positions $x_0 = 0.74$ cm and $y_0 = 0.07$ cm, suggesting an approximately 50% greater horizontal spread and moderate offset of the x axis. However, performing separate fit analyzes in each dimension separately may overstate the perceived anisotropy by overlooking correlations between the x and y coordinates, and in addition the reduced depth dimension in y results in limited sampling at the tails. A 2-dimensional Gaussian fit would more accurately assess anisotropy, so, the swimmer location data were fitted to a 2-dimensional Gaussian function of the form:

$$f(x, y) = ae^{-\left(\frac{x^2}{2\sigma_x^2}+\frac{y^2}{2\sigma_y^2}\right)} + b. \tag{2.1}$$

To ensure robustness against spatial binning, the fitting process was repeated across a range of grid resolutions, from 0.25× to 1.5× the PIV data resolution (63 × 17

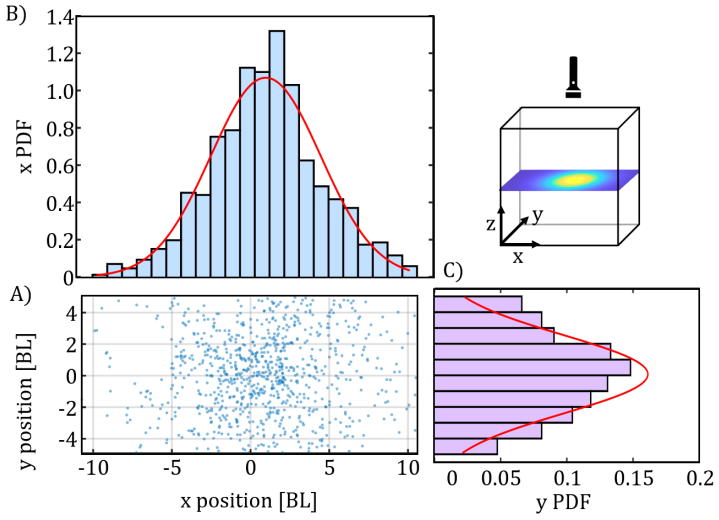

Figure 2.5: A) Scatter plot illustrating swimmer positions in the horizontal (x-y) plane, representing midpoint locations of measured trajectories. Marginal histograms depict the probability density functions (PDFs) of B) x and C) y swimmer positions along with the corresponding Gaussian fits used for K–S statistical testing. The inset orientation diagram shows the tank volume (22 cm × 22 cm × 10 cm in x, y, and z, respectively), highlighting the central location of the target flashlight at positive z, indicating the swimmers' upward migration direction.

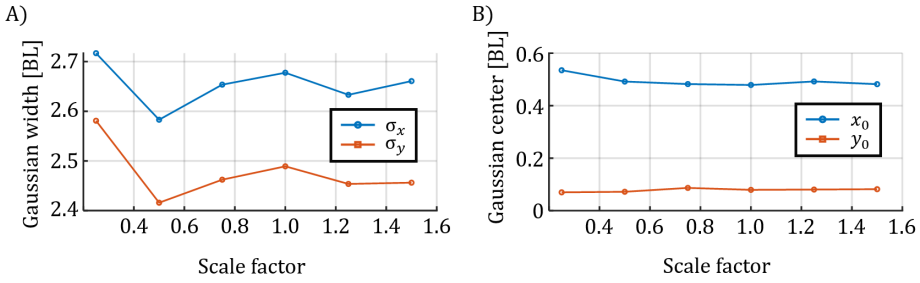

Figure 2.6: Insensitivity of 2-dimensional Gaussian fit parameters to varying bin resolutions: A) Gaussian widths and across scale factors; B) Gaussian distribution centers and across scale factors.

bins in x and y, respectively). The findings demonstrated remarkable stability in the Gaussian width parameters ($\sigma_x \approx 2.93$, $\sigma_y \approx 2.54$) and the distribution center ($x_0 \approx 0.54$, $y_0 \approx 0.06$), with variations of ±6% (figure 2.6). However, bin resolution significantly affected swimmer counts per bin, affecting the amplitude A) and baseline B) parameters, which were subsequently excluded from analysis.

A modest anisotropy of approximately 8% between σ_x and σ_y may still be due to the difference in the sampling ranges between x and y, or may reflect the behavior

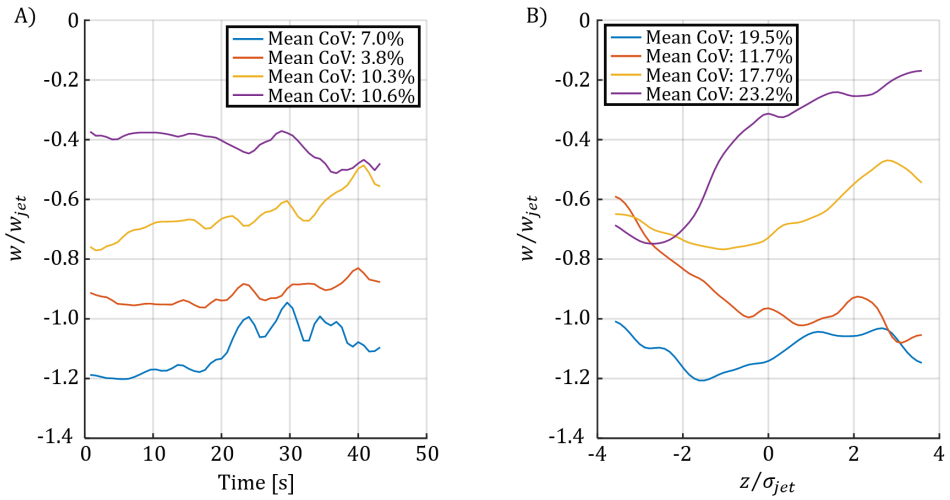

Figure 2.7: Evaluation of flow stability in terms of temporal and spatial variations. A) Vertical flow velocity (w) plotted against time, with coefficient of variation (CoV) provided in the legend, illustrating the steadiness of flow over the measurement duration. B) Vertical flow velocity (w) plotted against vertical position (z), with CoV in the legend indicating spatial variability along the vertical direction.

of the swimmer. Although brine shrimp show heightened sensitivity to blue and shorter wavelengths, they still maintain some limited sensitivity to red light and longer wavelengths. Consequently, the red laser sheet cutting across the tank along the x-axis could have led to a slightly wider distribution of swimmers along this axis.

Induced flow structure

Simultaneous to swimmer trajectories, the vertical component of the fluid velocity was measured using particle image velocimetry (PIV). To assess the temporal and spatial stability of the flow, the coefficient of variation (CoV), defined as the ratio of the standard deviation to the mean velocity, was calculated at four representative points (center, top, bottom left, and right). The mean and standard deviation were first calculated over time and the CoV values ranged from approximately 7% to 10% (figure 2.7 A), indicating low temporal fluctuations, suggesting that the flow can be treated as steady. Vertical (z) variability was evaluated by calculating the CoV with respect to z at these same points, yielding values between 11% and 23% (figure 2.7B), reflecting low to moderate spatial variability. Consequently, the vertical velocity field may be represented by its time-averaged and vertically averaged mean vertical velocity distribution within the horizontal (x-y) plane.

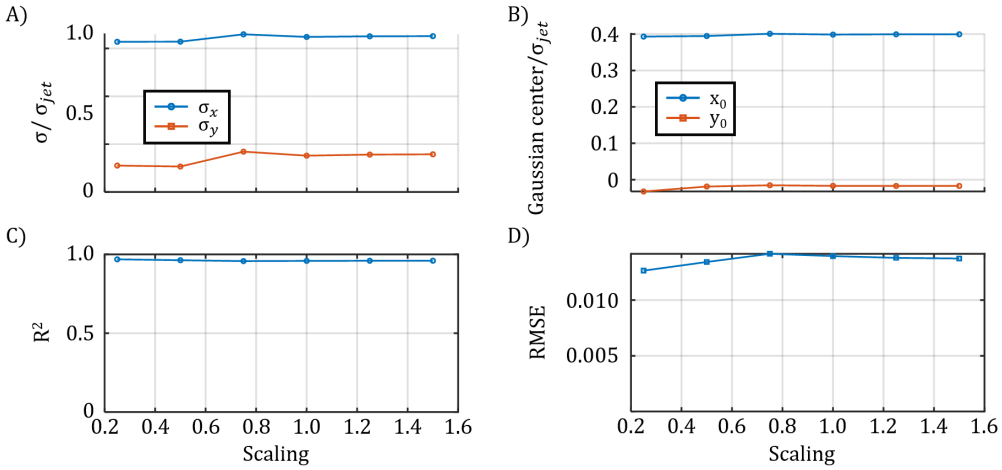

Figure 2.8: Stability and statistical robustness of the Gaussian fit across bin resolutions. A) Stability of Gaussian widths: σ_x, σ_y. B) Stability of Gaussian distribution center coordinates: x_0, y_0. (c) Goodness-of-fit metrics R^2. (d) Root mean square error.

The averaged velocity distribution exhibited a distinctly Gaussian-like shape, suggesting an axisymmetric jet-like structure (figure 2.9). The mean velocity distribution was fitted using the two-dimensional Gaussian function from 2.1 to quantify this observation. Again, to evaluate the stability of this Gaussian fit, spatial bin resolution was systematically varied from 0.25× to 1.5× the original PIV data resolution (63 × 17 bins for x and y, respectively).

The parameters obtained from the Gaussian fit, including the spread widths (σ_x, σ_y) and the coordinates of the distribution centers (x_0, y_0), demonstrated remarkable stability, exhibiting variations less than 2% on all scales tested (figure 2.8). Furthermore, goodness-of-fit metrics were consistently strong, with R^2 values greater than 0.95, and the root mean square error (RMSE) remained low, ranging from 0.012 to 0.014.

The Gaussian velocity fit (figure 2.9) demonstrated a slight elliptical anisotropy ($\sigma_x \approx 3.16$ cm, $\sigma_y \approx 2.78$ cm) and a center offset ($x_0 \approx 1.19$ cm, $y_0 \approx -0.05$ cm). The similarity in distribution characteristics between swimmer positions and the induced flow, particularly this slight anisotropy, indicates a direct connection through the swimmers acting as localized momentum sources.

For subsequent analyzes, we define an average Gaussian width, $\sigma_{jet} = 2.97$ cm, which is the mean of σ_x and σ_y from the Gaussian fit with the lowest total residual. This value serves as the characteristic normalization length scale. The centerline

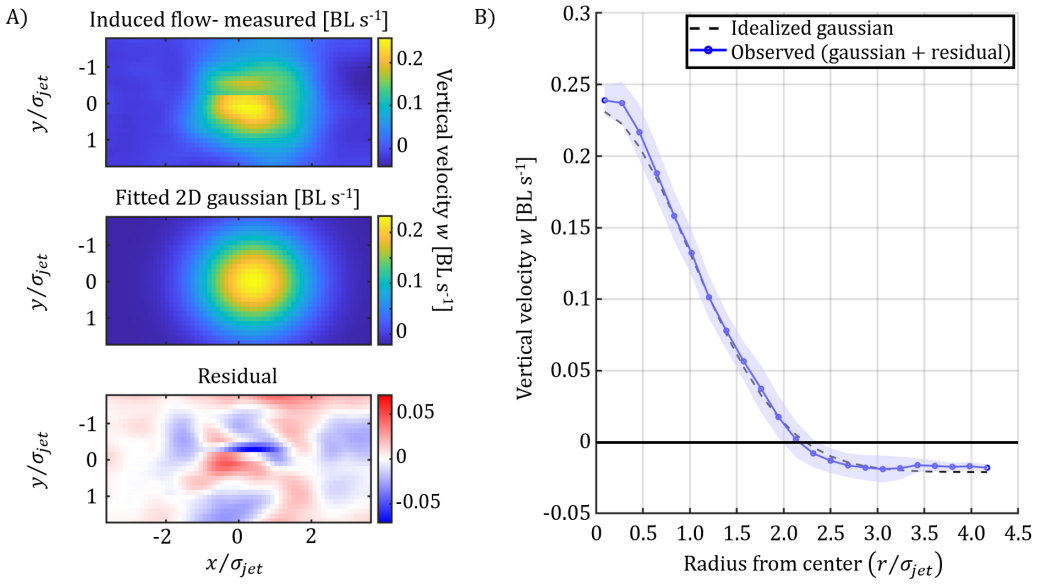

Figure 2.9: Gaussian fit analysis of induced vertical flow. A) Measured induced flow distribution displayed as a color map, where color intensity represents vertical velocity magnitude (absolute values used for clarity). B) 2-dimensional Gaussian fit to the observed velocity distribution, showing close correspondence to measured data. (c) Residuals between measured and Gaussian-fitted velocity distributions, highlighting regions of deviation. (d) Radial distribution of velocity magnitude from the tank center, comparing an idealized Gaussian profile (based on) and the observed velocity distribution (ideal Gaussian plus mean residual with shaded standard deviation).

flow speed derived from this optimal fit ($a + b$) is designated as the characteristic jet centerline flow speed, $w_{jet} = 0.23$ cm s^{-1}.

Using this length and speed scale, we calculated the jet Reynolds number:

$$\mathrm{Re}_{jet} = \frac{w_{jet}\sigma_{jet}}{\nu} = 65 \tag{2.2}$$

where ν is the kinematic viscosity of 15 parts per thousand salt water at 68°F (20°C), 1.05×10^{-2} cm^2 s^{-1}. This calculation places the induced jet within the intermediate Reynolds number regime ($1 < Re < 1000$). In this regime, inertial effects become significant enough to induce some coherent vortices and unsteadiness, while viscous effects continue to maintain clearly defined spatial gradients.

To further characterize the induced flow structure, we derived the magnitude of shear rate was derived from the spatial gradient of the vertical velocity field. Specifically, the instantaneous shear magnitude was computed using the following formula:

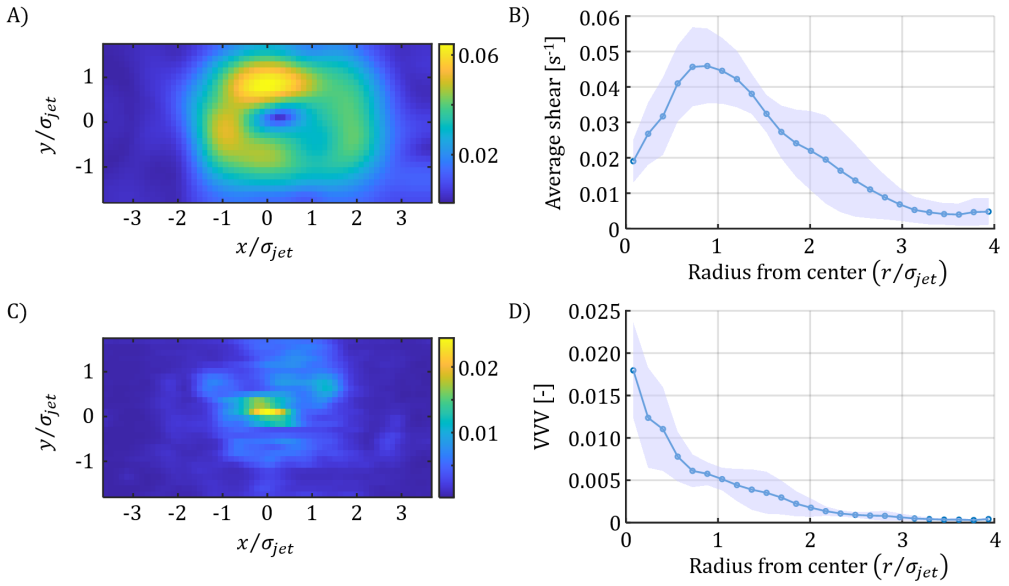

Figure 2.10: Spatial characterization of shear and vertical velocity variance(VVV). A) Color map of shear magnitude, highlighting peak shear forming a distinct annular region. B) Radial distribution plot of shear magnitude versus radius, with shaded region representing mean ± standard deviation within each radial bin showing peak values approximately one characteristic jet radius from the center. (c) Color map of vertically-averaged VVV distribution, illustrating highest variability near the jet center. (d) Radial distribution plot of vertically-averaged VVV versus radius, with shaded regions indicating mean ± standard deviation, showing rapid radial decay in unsteadiness.

$$|\nabla w| = \sqrt{\left(\frac{\partial w}{\partial x}\right)^2 + \left(\frac{\partial w}{\partial y}\right)^2} \tag{2.3}$$

This calculation was performed at each time step and the results were subsequently time-averaged to produce a representative shear magnitude distribution (figure 2.9 A). Using the center coordinates of the 2-dimensional Gaussian fit as a reference point, the shear magnitudes were binned radially. Radial bins were defined as approximately one-quarter of the original horizontal grid bin resolution. The mean shear values and the corresponding standard deviations within each radial section were calculated to quantify the spatial variability and the uncertainty of the measurement (figure 2.10 B).

The shear magnitude reached peak values of approximately 0.04–0.06 s^{-1} at a radial distance that roughly corresponds to the characteristic radius of the jet, creating a distinct annular region. This spatial distribution of shear is closely aligned with

typical jet behavior, where significant velocity gradients form near the jet boundary as a result of momentum exchange between the moving fluid core and the stationary surrounding fluid.

The vertical velocity variance (VVV) was derived from the fluctuations of the vertical velocity component around its mean. It is defined as:

$$\mathrm{VVV} = \frac{1}{2}\frac{w'^2}{w_{jet}^2}, \tag{2.4}$$

where w' denotes the variance of vertical velocity, or velocity fluctuations around the mean in time, and w_{jet} is the characteristic jet centerline velocity previously defined. The variance of velocity fluctuations was evaluated over time, averaged vertically (z), and then radially binned similarly to the shear analysis (figure 2.10).

The results revealed that VVV peaked at values between approximately 0.015 and 0.025 near the center of the jet, with a sharp decline to around 0.005 at distances corresponding to about one characteristic jet radius.

Swimmer flow interaction

The four-dimensional vertical velocity field $w(x, y, z, t)$, planar shear $|\nabla w(x, y, t)|$, and vertical velocity variability $\mathrm{VVV}(x, y)$ were interpolated onto the individual trajectories of the swimmers at each corresponding time step to explore the interactions between the swimmers and the induced flow structures. A relative vertical swimming speed was calculated by subtracting the local flow velocity from the swimmer's vertical speed in the lab frame.

Given the distinct radial symmetry of the flow structures, the swimmer metrics were analyzed with respect to radial position. To reduce the potential bias of slower swimmers, whose longer residence times could skew the results, the metrics were averaged per swimmer. For radial analyzes, the trajectories were classified based on characteristic jet radii, σ_{jet}: $< 1\sigma$, 1–2σ, 2–3σ, and $> 3\sigma$. The swimmer trajectories were segmented at these radial boundaries while preserving unique swimmer identifiers to avoid duplication in the swimmer count. Only trajectory segments exceeding 10 time steps (equivalent to 2 seconds) were included in the analysis. The resulting swimmer counts for each radial bin were as follows: 118 for $< 1\sigma$, 199 for 1–2σ, 71 for 2–3σ, and 21 for $> 3\sigma$.

To statistically evaluate differences in swimmer metrics across radial bins, a one-way ANOVA was performed, with pairwise comparisons using the Tukey-Kramer multiple comparison test. Statistical significance was annotated on the basis of p-values: *** for $p < 0.001$ and ** for $p < 0.01$.

An initial analysis of the vertical swimming speed in the laboratory frame suggested that the swimmers could exhibit an increasing vertical swimming speed with an increasing radial distance from the center of the tank (figure 2.11 A). However, when accounting for local flow velocity, the relative vertical swimming speeds remained consistently within the 0.4 to 0.5 cm s^{-1} range in all radial bins (Figure 2.11 B). This indicates that swimmers do not actively adjust their speeds in the face of reverse flow conditions or flow gradients.

There was no expected directional preference in the horizontal plane; this is evaluated by looking at the velocity unit vector in the radial and azimuthal components (figure 2.12). Although azimuthal velocity showed no significant directionality, indicating symmetrical or random swimming around the tank's vertical axis, radial velocity revealed a pattern. Average radial velocities start at 0, indicating no directional preference, at the center but have increasingly negative radial direction at larger radii, indicating a clear preference for movement toward the tank center. This behavior likely stems from the positive phototaxis of brine shrimp, since they may sense the radial gradient in illumination created by the target flashlight. Interestingly, despite the inherent inward radial bias, the spatial distribution of swimmers has maintained a Gaussian-like profile. This stability in distribution may be a balance between inward-directed swimming driven by phototaxis and outward-directed dispersive behaviors, such as random reorientation, collisions, and interactions among swimmers.

An analysis of the magnitudes of the velocity components revealed that the radial speeds did not differ significantly between the various bins (figure 2.13 A). However, a slight decrease in azimuthal velocity near the center and a visual trend indicating an increase in azimuthal velocity with radial distance were observed (figure 2.13 B).

To further elucidate these directional behaviors, the curvature of swimmer trajectories in the horizontal plane was computed as:

$$\kappa_{xy} = \frac{|u_x a_y - u_y a_x|}{(u_x^2 + u_y^2)^{\frac{3}{2}}}, \tag{2.5}$$

where u_x,u_v are horizontal velocity components and a_x, a_y are horizontal accelera-

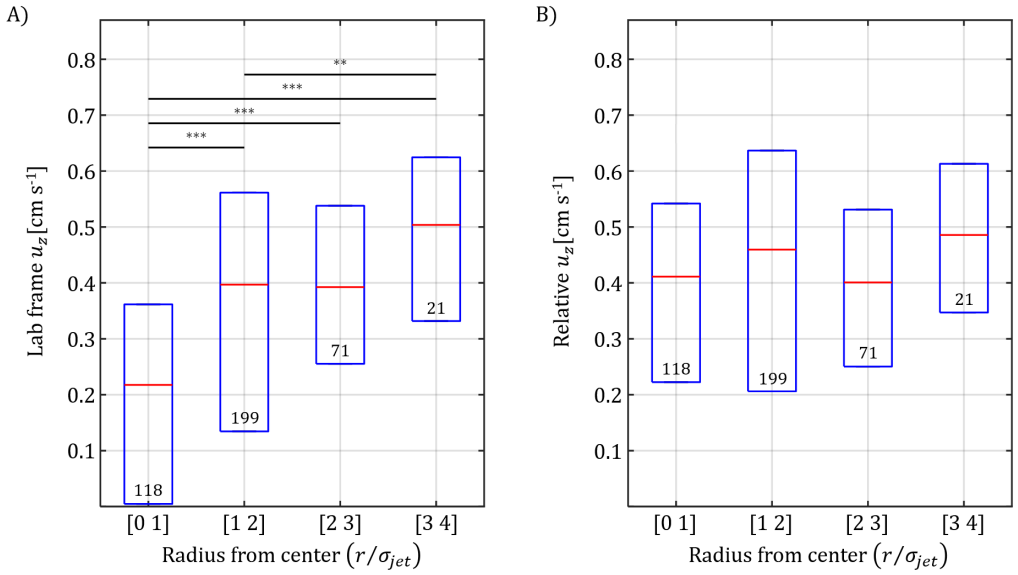

Figure 2.11: Analysis of swimmer vertical speeds as a function of radial position in the experimental tank. A) Box plots of laboratory-frame vertical swimming speeds (cm s^{-1}) across different radial bins. Boxes indicate the inter-quartile range, horizontal lines denote median values, whiskers represent minimum and maximum values excluding outliers, and outliers are shown as individual points. B) Corresponding box plots of relative vertical swimming speeds, computed by subtracting the local vertical flow velocity from the swimmers' lab-frame speed. Relative swimmer speeds remained consistently between 0.4 and 0.5 cm s^{-1} across radial positions, demonstrating that the observed radial differences in panel A) were primarily due to local fluid velocities rather than active adjustments by swimmers to varying environmental conditions. Statistical significance between radial bins was assessed using one-way ANOVA and Tukey-Kramer multiple comparisons, with significant pairwise differences denoted by asterisks (** for p<0.01, *** for p<0.001). Sample sizes (n) for each radial bin are indicated below each box plot.

tion components. The radius of curvature, R_{xy}, was derived from the curvature:

$$R_{xy} = \frac{1}{\kappa_{xy}}. \tag{2.6}$$

The radius of curvature increased with radial distance, indicative of straighter trajectories further from the center. Coupled with increasing azimuthal velocities at larger radii, this suggests potential helical motion, characterized by larger, faster circles at outer radii coupled with consistent inward movement (figure 2.14 A).

To validate whether swimmers participated in organized vortical behavior [62], instantaneous curvature centers (x_0, y_0) were calculated by identifying intersections

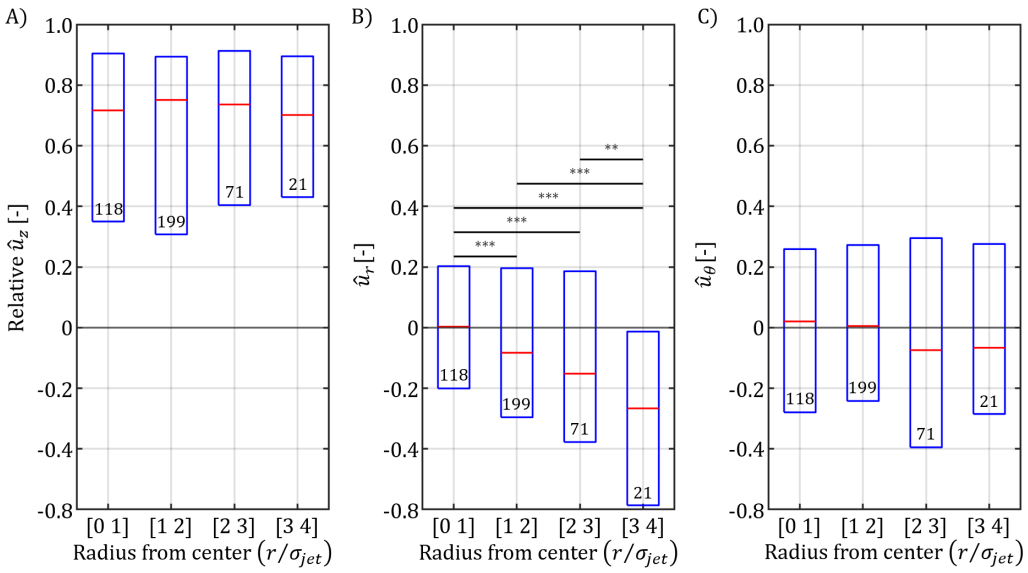

Figure 2.12: Analysis of directional swimming behavior of brine shrimp. Box plots represent velocity unit vectors decomposed into vertical, radial, and azimuthal components across different radial bins from the tank center. A) Relative vertical unit vector components, indicating a clear and consistent vertical swimming. B) Azimuthal unit vector components, indicating no significant directional preference and consistent symmetrical or random swimming about the tank's central vertical axis. C) Radial unit vector components, showing a clear pattern of increasingly negative (inward-directed) radial velocities with greater radial distances from the tank center. This inward-directed swimming behavior suggests positive phototaxis toward the centrally placed target flashlight, potentially in response to the radial illumination gradient. Despite this inward bias, swimmers maintained a stable Gaussian-like radial distribution, possibly due to a balance between phototaxis-driven inward movement and dispersive processes such as random reorientation, collisions, and swimmer-swimmer interactions. Statistical significance between radial bins was assessed using one-way ANOVA and Tukey-Kramer multiple comparisons, with significant pairwise differences denoted by asterisks (** for p<0.01, *** for p<0.001). Sample sizes (n) for each radial bin are indicated below each box plot.

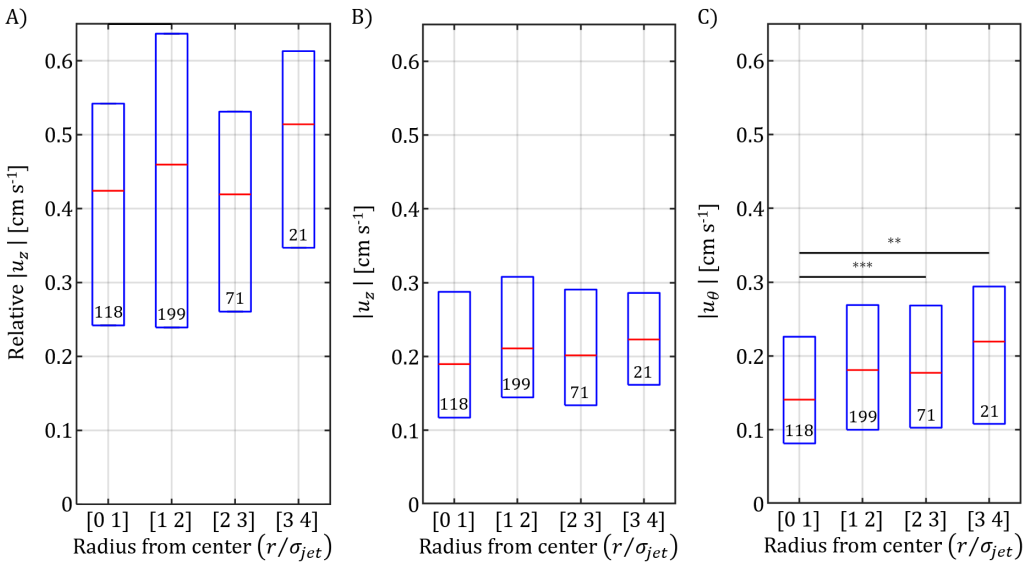

Figure 2.13: Magnitude analysis of horizontal swimming velocity components of brine shrimp as a function of radial distance from the tank center. A) Vertical velocity magnitudes, showing no statistically significant differences across radial bins, indicating uniform vertical swimming throughout the observed region. B) Radial velocity magnitudes, showing no statistically significant differences across the radial bins, indicating uniform radial swimming activity throughout the observed region. C) Azimuthal velocity magnitudes, revealing a slight but noticeable decrease in swimmer velocity near the tank center, with a visual trend of increasing velocity magnitude at greater radial distances. Statistical significance between radial bins was assessed using one-way ANOVA and Tukey-Kramer multiple comparisons, with significant pairwise differences denoted by asterisks (** for p<0.01, *** for p<0.001). Sample sizes (n) for each radial bin are indicated below each box plot.

of perpendicular bisectors drawn from sets of three sequential trajectory points. Specifically, for three consecutive points p_1, p_2, p_3, the perpendicular bisectors were calculated from the midpoints of the segments connecting p_1 to p_2 and p_2 to p_3. The intersection of these bisectors provides the center of instantaneous curvature. Collinear points were excluded due to undefined curvature centers. The center of curvature was converted to a radial position $r_{xy} = \sqrt{x_0^2 + y_0^2}$, such that if the swimmers collectively orbited a central vortex, the centers of curvature would cluster around the center of the tank ($r_{xy} = 0$) across all radii. However, the curvature centers diverged significantly from the midpoint with increasing r moving outward radially (figure 2.14 B).

This analysis reveals that swimmers do not exhibit collective swirling or globally organized vortical motion. Instead, their trajectories represent locally organized but

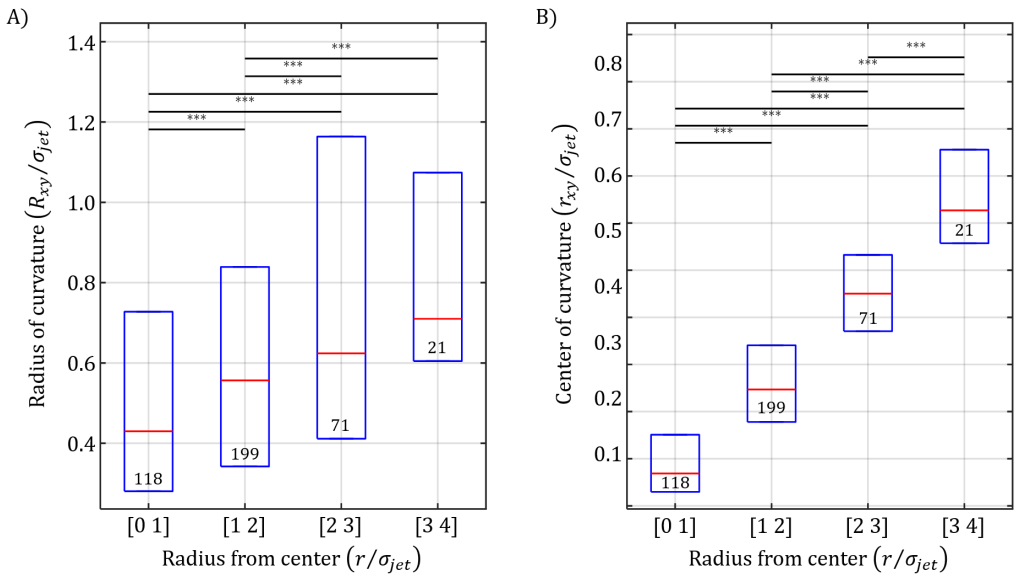

Figure 2.14: Analysis of instantaneous curvature centers calculated from swimmer trajectories to identify potential collective vortical behavior. For each set of three sequential trajectory points, perpendicular bisectors of line segments connecting consecutive points were computed, with their intersection defining the instantaneous curvature center. Collinear points were excluded from this analysis due to undefined curvature. A) Normalized radius of curvature, R_{xy}/σ_{jet}, as a function of swimmer radial position, showing increasing large circles formed by swimmers with increasing distance from the center. B) Radial position of instantaneous curvature centers, r_xy/σ_{jet} as a function of swimmer radial position, showing increasing deviation from the tank midpoint as swimmers move further from the center. Statistical significance between radial bins was assessed using one-way ANOVA and Tukey-Kramer multiple comparisons, with significant pairwise differences denoted by asterisks (** for p<0.01, *** for p<0.001). Sample sizes (n) for each radial bin are indicated below each box plot.

independent turning behaviors, which differ distinctly with radius. Closer to the center of the tank, swimmers demonstrate a higher curvature (frequent directional changes) at lower azimuthal speeds. At greater radial distances, swimmers move in smoother, less frequent turns at higher azimuthal speeds. These findings underscore autonomous local motion behaviors, ruling out large-scale coordinated vortical motion as the primary driver of observed swimmer trajectories.

2.4 Discussion

Despite encountering varying local flow velocities and a range of variability conditions, the swimmers consistently maintained a stable relative vertical swimming speed. This consistency suggests a predominantly passive interaction with vertical

flow structures, indicating limited or no active compensation in vertical swimming speed to counteract adverse flow or shear layers.

An inward radial directional preference was observed among the swimmers, most likely influenced by their known positive phototaxis. This preference for movement toward the illuminated tank center contrasts intriguingly with the consistent Gaussian-like horizontal distribution, highlighting a dynamic balance between attractive and dispersive behaviors. The Gaussian spatial distribution implies that inward phototactic attraction may be balanced by outward dispersive factors, including random turning events, collisions, or hydrodynamic repulsion among neighboring swimmers. The presence of exclusion zones, approximated at around 1 cm, further supports the notion that direct inter-individual interactions substantially influence collective spatial structure. This balance between attraction toward favorable environmental conditions and avoidance behaviors driven by inter-individual interactions warrants further investigation, particularly in the context of collective decision-making processes.

The horizontal curvature of the swimmer's trajectory exhibited distinct radial dependencies, characterized by higher curvature and lower azimuthal speeds near the center of the tank, transitioning to smoother, less curved paths with increased azimuthal velocities at larger radial distances. Such behaviors suggest a potential transition in swimming modes, from erratic and frequent reorientation near areas of high swimmer density and flow shear, to more directed and streamlined trajectories at the periphery. Although this behavior could have indicated the presence of collective global vortical motion, instantaneous curvature centers diverged significantly from the tank midpoint with increasing radial distance. Thus, swimmers appear to exhibit locally organized but individually autonomous turning behaviors rather than coordinated large-scale swirling motions. This finding contributes to ongoing discussions in the collective behavior literature regarding the scale at which the organization emerges and underscores the importance of resolving both spatial and temporal scales when interpreting collective swimming behaviors.

For this experiment, light intensity, flow speed, velocity variability, and high swimmer concentration are spatially colocated and directly correlated with the radial distance from the tank center. Consequently, disentangling the specific environmental factor driving observed behavioral differences among swimmers proves challenging. However, comparing the characteristic spreading lengths derived from Gaussian fits of the swimmer positions (σ = 2.7 cm), fluid flow structure (σ = 2.9 cm), and

the illuminated region of the tank (beam radius = 3.5 cm) the close alignment of these spatial scales suggests a hierarchical causality: swimmers respond primarily to the spatial structure of the illumination, forming a characteristic spatial distribution, and in turn, the induced fluid flow closely mirrors this swimmer distribution. Given the improbability of direct fluid response to illumination alone, the observed flow structure is most plausibly interpreted as a consequence of swimmer behavior. This alignment underscores the dominant role of swimmers in shaping their fluid environment and emphasizes the need for further investigation into how behavioral responses to environmental stimuli propagate into collective fluid dynamical patterns.

Future research directions can explore these responses by explicitly focusing on decoupling correlated environmental variables to identify specific mechanisms driving behavioral differences. Experimentally separating environmental conditions would clarify individual influences on swimming behaviors and the thresholds and decision-making rules governing collective vertical migration for brine shrimp.

Chapter 3

INDUCED FLOW RESPONSE TO SWIMMER BUOYANCY

ABSTRACT

Marine organisms undergoing diel vertical migration traverse substantial vertical distances. In this chapter, we experimentally investigate how variations in buoyancy between actively swimming organisms, specifically brine shrimp (*Artemia salina*), influence collective hydrodynamic patterns. The salinity of the fluid environment is changed, resulting in a variable buoyant force on the swimmers. Simultaneous swimmer tracking alongside particle image velocimetry (PIV) is used to quantify the impact of buoyancy on induced flow velocities. These results demonstrate that increased swimmer buoyancy is correlated with decreased collective jet velocities. The experimental results align well with the theoretically estimated induced flow predicted by an actuator disk model that is negatively buoyant and vertically climbing at a steady rate. Understanding the connection between organism buoyancy and collective-induced flows is important for predicting ecological consequences of vertical migrations, particularly their role in ocean mixing, nutrient distribution, and broader biological-physical interactions.

3.1 Introduction

Many marine organisms possess tissues that are denser than water, leading to the evolution of various adaptations to manage buoyancy for vertical movement in the water. These adaptations include swim bladders in teleost fish, oil-rich livers in sharks, and gas-filled chambers in cephalopods [63]. A nonmotile phytoplankton, *Pyrocystis noctiluca*, has been found to use rapid cell inflation to achieve buoyancy changes that enable long-distance vertical migration without the use of swimming appendages [64]. In contrast, many small planktonic animals depend solely on swimming upward to maintain their vertical position in the water [63]. For example, krill species, such as *Euphausia superba*, remain negatively buoyant throughout their lives, necessitating continuous active swimming or employing intermittent sinking behavior to maintain or adjust their vertical position [29]. This persistent negative buoyancy in krill is primarily due to their limited lipid reserves and dense exoskeletal structure, obligating constant locomotion or controlled sinking behaviors.

These planktonic animals make up the majority of the biomass in DVM, traversing vertical distances that span hundreds of meters [23]. These distances often coincide with permanent pycnoclines, ocean layers that separate lighter surface waters from denser deep waters, which range from depths of approximately 200 to 800 meters and have density changes between 1 and 2 percent [65, 66]. Therefore, swimmers are likely to encounter changes in surrounding fluid density on the order of several percent, and understanding the relationship between swimmer buoyancy and the induced hydrodynamic patterns is crucial for predicting the impact that vertical migrations have on ocean mixing and nutrient transport.

In this chapter, we explore how variations in buoyancy influence aggregate hydrodynamic structures, specifically focusing on the flow speeds induced by collective vertical migrations. In experiments using brine shrimp (*Artemia salina*), the salinity of the surrounding water was varied to modulate the relative buoyancy of the swimmer. Simultaneous swimmer tracking and 2-component particle image velocimetry (PIV) were used to quantitatively determine how animal buoyancy affects the speed of the induced flow. The results show that increases in swimmer buoyancy correlate with a decrease in resulting flow speed. An actuator disk model is used to support the impact that swimmer bouyancy has on flow. According to actuator disk theory, negatively buoyant swimmers moving upward must generate sufficient thrust to overcome their downward buoyancy force. This thrust transfers momentum to the surrounding fluid, producing induced flow. Consequently, as swimmer buoy-

ancy increases (becoming less negatively buoyant), swimmers require less thrust to ascend, thus transferring less momentum to the fluid, resulting in reduced induced flow speeds.

3.2 Experimental methods

Experimental Setup and Migration Induction

Experimental organisms (*Artemia salina*) were prepared following the procedures described in Section 2.2. The experimental setup, including tank dimensions, seeding with tracer particles, and induction of vertical migration using bottom and top flashlights, was completed according to the procedures in Section 2.2. For these buoyancy experiments, 6 tsp (30 ml) of swimmer were added and the recording began when the top flashlight was activated and continued uninterrupted for a total of 200 seconds. Four trials were conducted at each salinity level.

The imaging and 3-D scanning method was similar to that section 2.2. However, in these experiments, the scanning laser sheet was confined to a depth of 2 cm of the tank, resulting in effectively 2-D swimmer trajectories in x and z, with limited y dimension (swimmers are induced to migrate toward positive z which is the vertical direction). Although the resulting trajectories were 2-dimensional, the 2 cm scanning thickness facilitated reliable identification of swimmers and accurate tracking over time using the same processing methods described in Section 2.2. Simultaneously, PIV was used to measure 2-component 2-dimensional flow data from the mid-slice of this scanned volume (figure 3.1). These changes enabled a recording duration that was more than 6 times longer than with the full 3-D scanning protocol (250 vs. 40 s). Therefore, the trade-off in 3D trajectories was made in order to allow analysis of changes in the development of the induced flow.

Salinity treatments and density measurement

Four salinities were chosen to test swimmer buoyancy as a variable: 15, 17, 19, and 22 parts per thousand (ppt). These salinities correspond to densities of 1009, 1011, 1012.5, and 1014.5 kg m^{-3}, respectively, which span approximately a 1% change in fluid density. This range of density variation is representative of natural density gradients that organisms may encounter during diel vertical migrations in stratified aquatic environments, and the magnitude of densities was selected based on previous tests in which a visible jet was produced. Salinity levels were adjusted by dissolving Instant Ocean Sea Salt (Spectrum Brands) into DI water (Type II, ChemWorld) and measured using a CastAway Conductivity, Temperature and Depth Profiler (CTD)

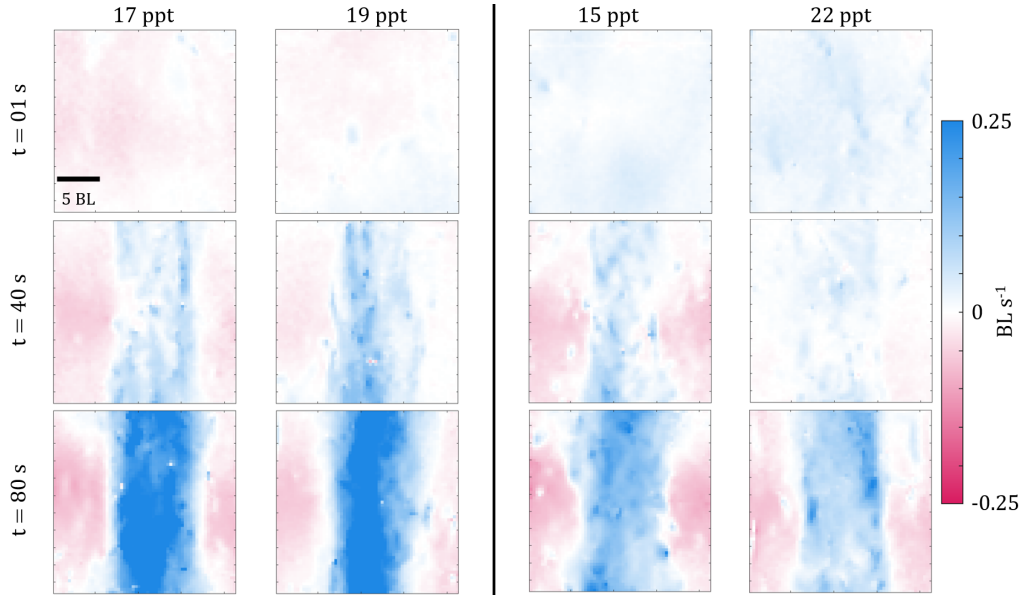

Figure 3.1: Formation and evolution of induced flow jet during brine shrimp vertical migration at salinities of 15, 17, 19, and 22 ppt. Images are arranged in columns corresponding to each salinity condition and rows showing snapshots at times t=0, 40, 80 s. Jet formation is visualized through [insert visualization method, e.g., particle image velocimetry (PIV), dye visualization, or velocity contour plots], illustrating how jet strength and scale vary across salinity conditions and evolve over time. The observed jet weakens progressively with increasing salinity, reflecting changes in swimmer buoyancy and resulting induced flows. Due to differences in the number of swimmers the 15 and 22 ppt cases are compared and the 17 and 19 ppt cases are compared independently.

(salinity range = 0-42 ppt, precision = 0.10 ppt, resolution = 0.01 ppt, temperature range = -5-45 °C, accuracy = 0.05°C, resolution = 0.01°C, www.sontek.com). For each test, water of the desired salinity was prepared the night before brine shrimp was received. Final measurements were taken with the CTD at 5 locations in the tank (4 corners and center) the following morning immediately before the animals were loaded into the tank. The average and standard deviation of the salinity and density recorded by the CTD over the depth of the tank are shown in figure 3.2. The measurements for the four conditions, averaged in depths and tank locations, were: 15.07 ±.10, 17.26 ±.11, 19.48 ±.10, and 21.84 ±.10 ppt and 1009.3 ±.02, 1010.9 ±.04, 1012.7 ±.02, and 1014.4 ±.03 kg m^{-3}. For readability, in the remainder of the writing these four conditions will be referred to as 15, 17, 19, and 22 ppt.

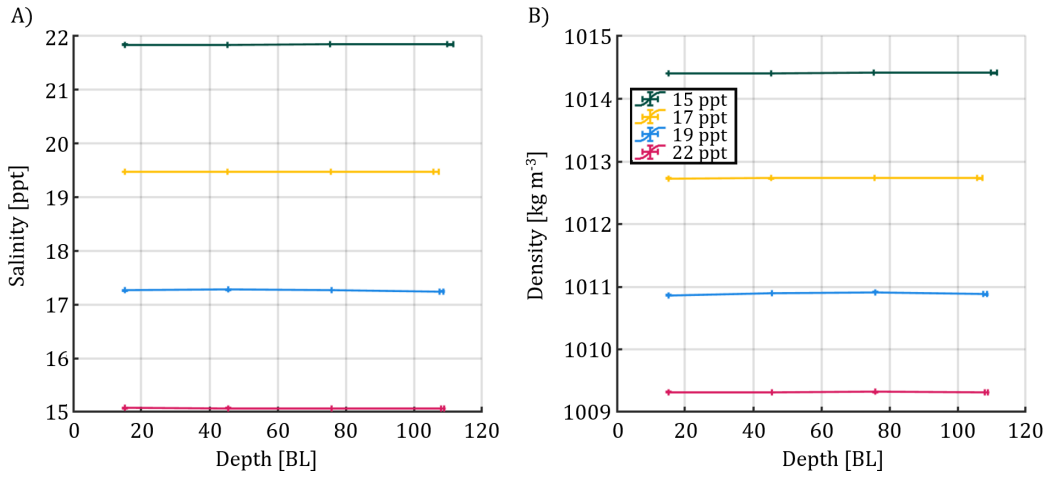

Figure 3.2: Measured A) salinity and B) density values for the four experimental conditions vs depth. Salinity was adjusted to four target values—15, 17, 19, and 22 ppt and salinity and density were verified using a CastAway CTD profiler (SonTek, USA), with five measurements taken from different locations in the tank immediately before loading animals. Salinity and density values are are shown as the average ± (accuracy + standard deviation) across these five tank locations for each condition.

3.3 Results

Using the PIV measurement and swimmer tracks that are collected simultaneously, the relative swimming speed was calculated for each swimmer as the swimmer's velocity in the laboratory frame minus the local fluid velocity interpolated at each swimmer's location. To visualize the consistency and variability in repeated trials, the raw data is plotted, and although clear trends were observed in each variable, there are apparent timing differences between the trials (figure 3.3). These timing differences may obscure direct comparisons. To address this, the data was temporally aligned by shifting each trial so that their peak relative swimmer speeds coincided (figure 3.4). This alignment facilitated clearer comparisons of common trends and enabled accurate averaging across trials. Subsequent analyzes and statistical comparisons were performed using this aligned data.

To determine whether the number of swimmers vertically migrating differed significantly between salinity treatments, a one-way analysis of variance (ANOVA) test was conducted on swimmer counts at the final recorded time (170 seconds). The swimmer counts were grouped by salinity. Subsequent pairwise comparisons using the Tukey-Kramer multiple comparison test identified no statistically significant differences in swimmer number between 17 and 19 ppt conditions or between the 15 and 22 ppt conditions; however, a significant difference in swimmer number was

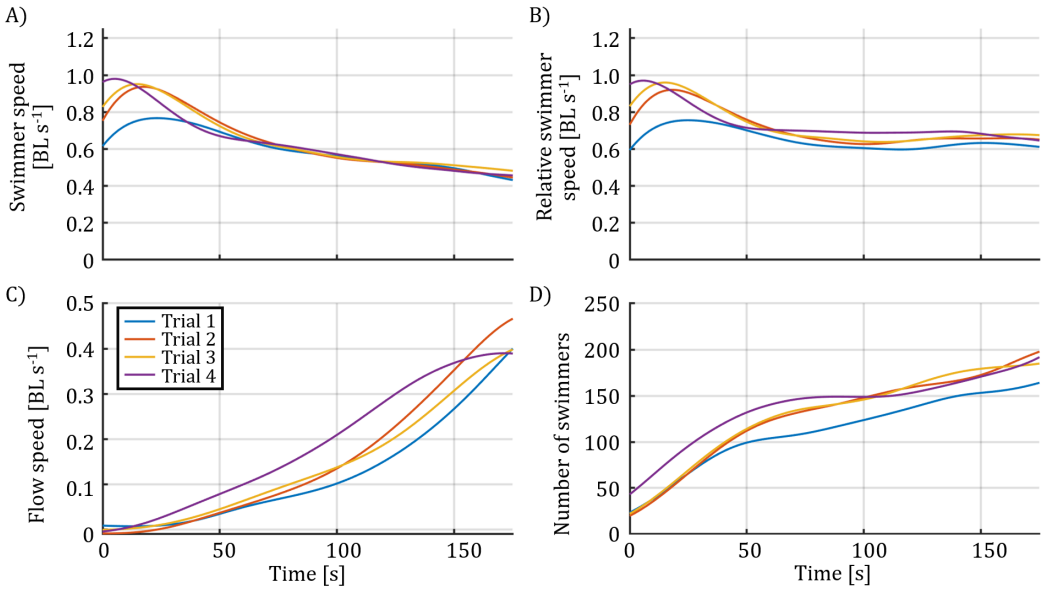

Figure 3.3: Unshifted mean data for each of the four trials conducted at 17 ppt salinity. A) Swimmer speed over time; B) Relative swimmer speed (swimmer speed plus flow speed at each swimmer location) over time; (c) Peak flow speed within the aggregation over time; (d) Number of swimmers visible within the field of view over time.

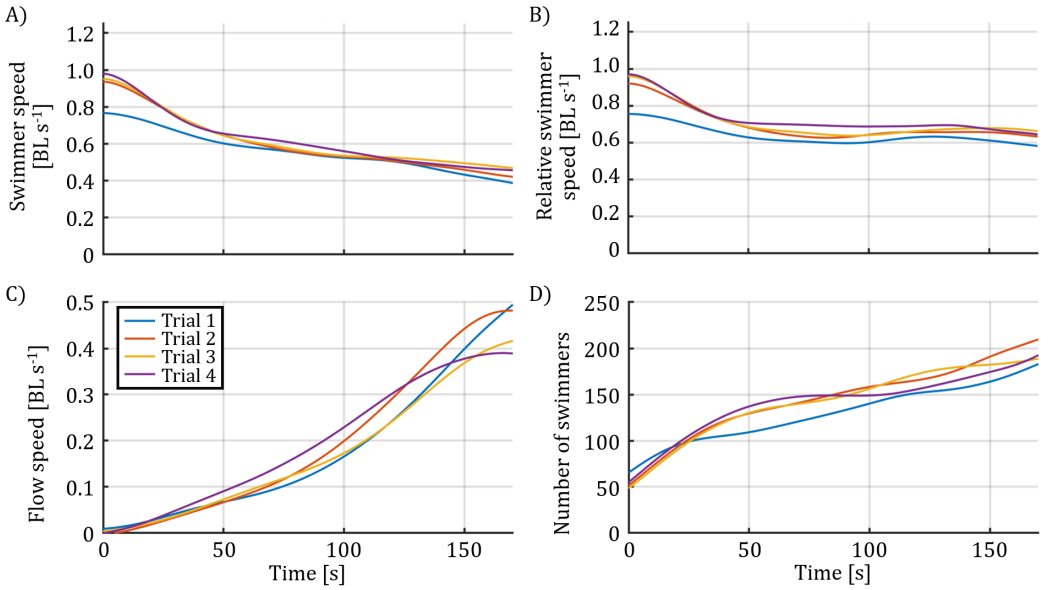

Figure 3.4: Time-shifted mean data for the four trials at 17 ppt salinity, aligned such that peak relative swimmer speed occurs simultaneously. A) Swimmer speed over time; B) Relative swimmer speed (swimmer speed plus flow speed at each swimmer location) over time; (c) Peak flow speed within the aggregation over time; (d) Number of swimmers visible within the field of view over time. This alignment facilitates direct comparison of temporal patterns across trials.

observed when comparing these two pairs of conditions (figure 3.5). This difference was likely introduced as a combination of human handling errors in the addition of swimmers to the tank and varying animal conditions upon arrival. Therefore, means that direct comparisons between these two salinity pairs for other measured variables were confounded, and consequently, subsequent statistical analysis is focused on comparisons within the pairs (15 vs. 22 and 17 vs. 19 ppt), rather than between them.

The same ANOVA and multiple comparison test was used to determine significant differences in the final maximum jet flow velocity, used to represent the centerline velocity, between treatments. There was a significant difference between the 17 and 19 ppt pair, but not between the 15 and 22 ppt pair. However, the trend between the two pairs is qualitatively consistent: it shows a decrease in induced flow with increasing salinity (figure 3.6).

Furthermore, to determine whether the observed differences in the induced jet velocity may be due to variations in swimmer speed, the same statistical analysis was applied to the relative swimming speeds. Again, there was a significant difference between the 17 and 19 ppt pair, but not between the 15 and 22 ppt pair (figure 3.7). However, if each swimmer was considered statistically independent, these differences in means would be considered significant. Therefore, in further analysis, we will still consider the impact of these differences for completeness.

To better contextualize our experimental findings and assess the physical basis of the observed variations in induced flow, we compared the experimental results directly with predictions from an actuator disk model that estimates induced flow velocities based on the conservation of momentum [67]. The actuator disk model assumes uniform thrust distribution across a hypothetical disk, an idealization previously applied effectively to model collective organism swimming [4, 30] according to the following equation:

$$\Delta W = \frac{-u_z}{2} + \sqrt{\frac{u_z^2}{4} + \frac{F_b}{2\rho A_D}}, \tag{3.1}$$

where W_0 is the induced velocity in the centerline directly behind the actuator disk, u_z is the speed of the actuator disk, A_D is the area of the actuator disk, ρ is the fluid density and F_b is the buoyant force acting on the actuator disk. In order to translate this to our collective vertical migration, a representative vertical swimming velocity

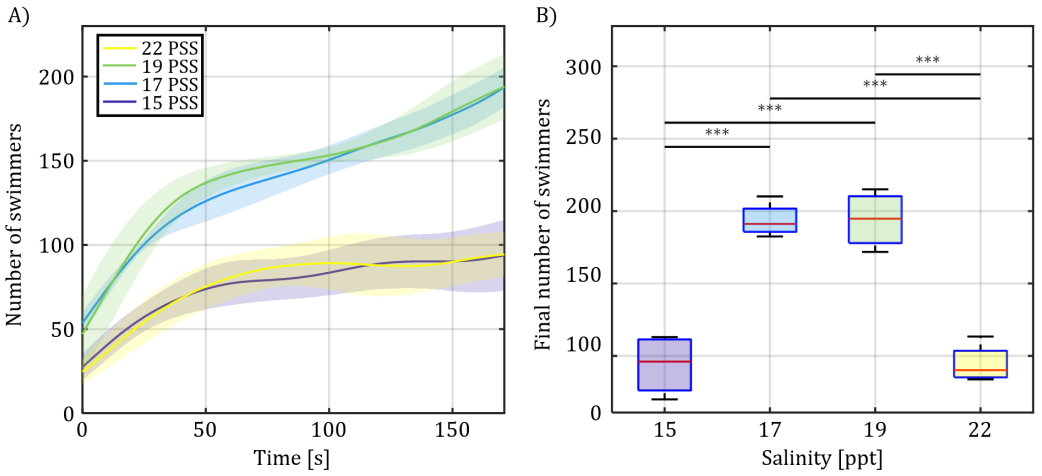

Figure 3.5: Swimmer counts for each salinity condition during induced vertical migration. A) Average swimmer number throughout the migration, plotted as mean values (solid lines) with shaded regions indicating standard deviation. B) Box plots showing the distribution of swimmer number at the final recorded time step for each salinity condition (15, 17, 19, and 22 ppt). Due to differences in the number of swimmers the 15 and 22 ppt cases are compared and the 17 and 19 ppt cases are compared independently. Boxes represent the inter-quartile range, with the central line indicating the median, and whiskers extending to the minimum and maximum data points. Statistical significance was evaluated using pair-wise ANOVA with n=4 trials per condition. Significant differences between groups are denoted by asterisks (* for $p < 0.05$, ** for $p < 0.01$, *** for $p < 0.001$).

will be used for u_z, and the buoyancy will be set equal to the net buoyant force on all swimmers, defined as:

$$F_b = N\Delta\rho g V_s, \tag{3.2}$$

where N is the number of swimmers, $\Delta\rho$ is the difference in density between a swimmer and the surrounding fluid, g is gravitational acceleration and V_s is the volume of each swimmer.

Upon plugging 3.2 into 3.1, the induced flow is modeled as:

$$\Delta W = \frac{-u_z}{2} + \sqrt{\frac{u_z^2}{4} + \frac{N\Delta\rho g V_s}{2\rho A_D}} \tag{3.3}$$

The number of swimmers is projected to a 3-D estimate by assuming the spread of swimmers is axisymmetric about the center of the tank and dividing the scanned volume into k shells,

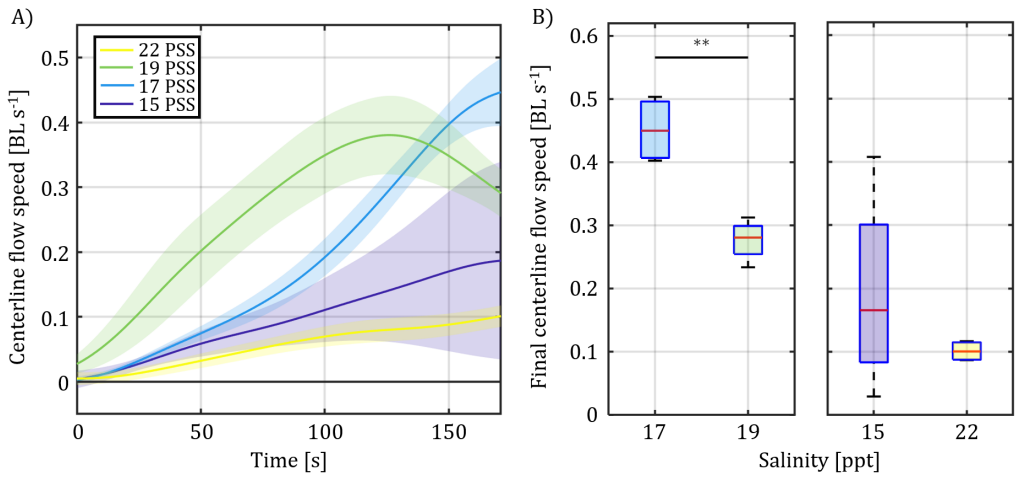

Figure 3.6: A) Mean flow velocity at 170 s, averaged spatially and and across four trials per salinity condition. Solid lines indicate the mean, with shaded regions representing the standard deviation. B) Box plots illustrating the distribution of measured flow velocities at swimmer locations at the final recorded timestep for each salinity condition (15, 17, 19, and 22 ppt). Due to differences in the number of swimmers the 15 and 22 ppt cases are compared and the 17 and 19 ppt cases are compared independently. Boxes indicate the inter-quartile range, horizontal lines denote median values, and whiskers extend to minimum and maximum data points excluding outliers. Significant differences between conditions were determined using one-way ANOVA, with pairwise post-hoc comparisons. All pairwise differences shown are statistically significant, indicated by asterisks (* for $p < 0.05$, ** for $p < 0.01$, *** for $p < 0.001$). Due to the aggregation of velocity data from each swimmer location, the sample size n for each condition is shown below each condition.

$$\Delta V_k = \pi(r_{k+1}^2 - r_k^2)\Delta y \tag{3.4}$$

where Δy is the depth scanned, 2 cm. The number of swimmers in each volume, n_k, is then used to calculate the animal number density per shell,

$$n_k = \frac{N_k}{\Delta V_k} \text{ [swimmers cm}^{-3}\text{]}. \tag{3.5}$$

This animal number density is then multiplied by the full volume of each cylindrical shell to get the final number of swimmers:

$$N = \sum_k n_k \pi(r_{k+1}^2 - r_k^2). \tag{3.6}$$

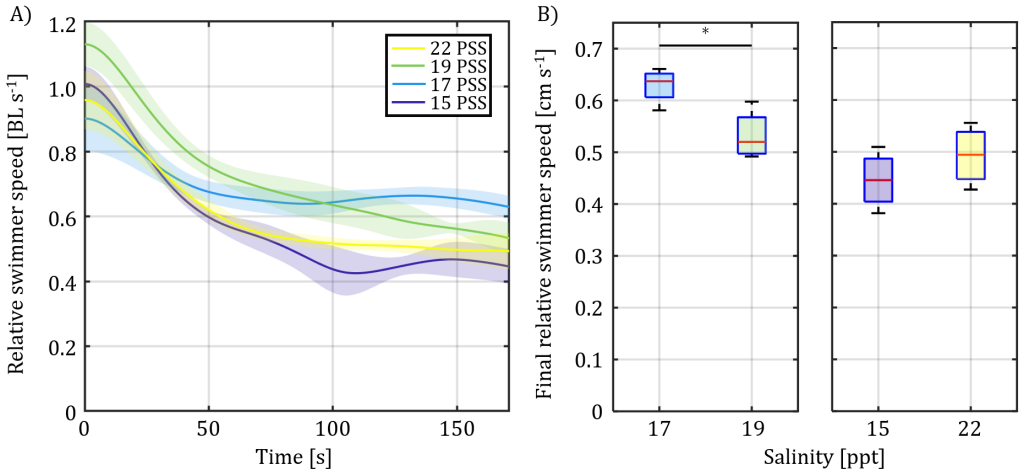

Figure 3.7: A) Mean vertical swimming velocity at 170 s, averaged spatially and and across four trials per salinity condition. Solid lines indicate the mean, with shaded regions representing the standard deviation. B) Box plots illustrating the distribution of measured flow velocities at swimmer locations at the final recorded timestep for each salinity condition (15, 17, 19, and 22 ppt). Due to differences in the number of swimmers the 15 and 22 ppt cases are compared and the 17 and 19 ppt cases are compared independently. Boxes indicate the inter-quartile range, horizontal lines denote median values, and whiskers extend to minimum and maximum data points excluding outliers. Significant differences between conditions were determined using one-way ANOVA, with pairwise post-hoc comparisons. All pairwise differences shown are statistically significant, indicated by asterisks (* for $p < 0.05$, ** for $p < 0.01$, *** for $p < 0.001$). Due to the aggregation of velocity data from each swimmer location, the sample size n for each condition is shown below each condition.

The number of swimmers, the median speed of ascent of the swimmer, and the fluid density were used as input parameters to estimate the induced flow using an actuator disk model. The predictions of the model are made and compared for each individual trial rather than averaging all the trials in each salinity treatment (figure 3.8). Additional variables defined are listed in table 3.1. These values were approximated to be of the order of observations made during laboratory experiments using brine shrimp. In general, the actuator disk model captures the observed experimental trends. However, notable deviations were identified at the 15 ppt salinity condition, where the predicted induced flow of the model substantially exceeded the experimentally measured values.

This discrepancy in the 15 ppt trials is likely attributed to variance in animal behavior, for example, the pronounced skew towards lower swimming velocities is visualized in figure 3.9).

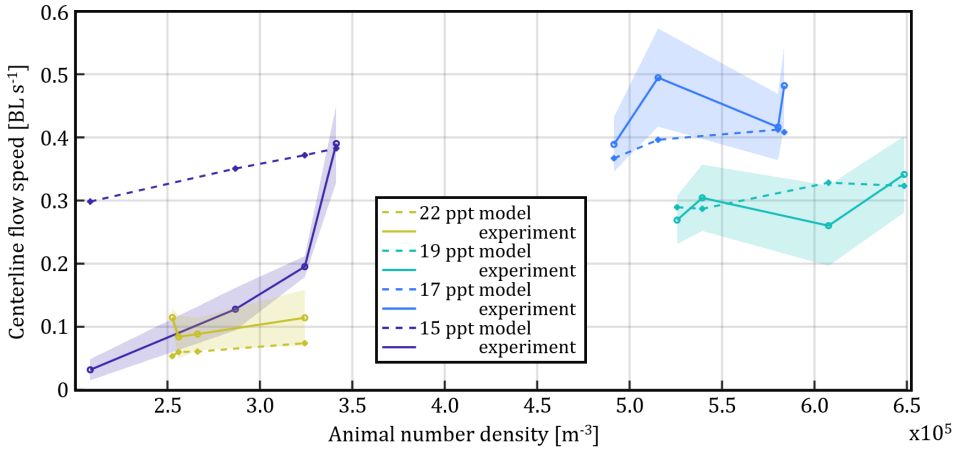

Figure 3.8: Measured induced centerline flow velocities versus animal number density for each salinity condition (15, 17, 19, and 22 ppt). Due to differences in the number of swimmers the 15 and 22 ppt cases are compared and the 17 and 19 ppt cases are compared independently. Each data point represents an individual trial, with shaded regions indicating the standard deviation of measured flow speeds at 170 s. The dotted line denotes the prediction from the actuator disk model, scaled by a factor of 0.5 for qualitative comparison with the measured velocities.

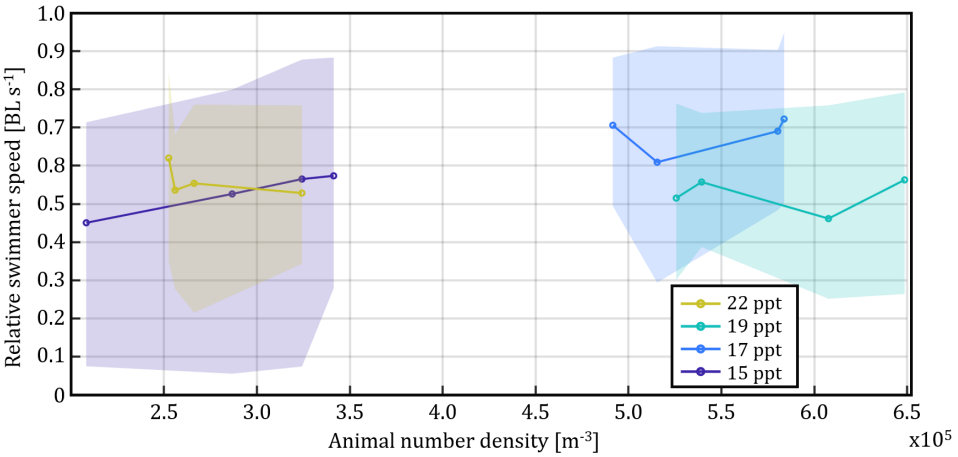

Figure 3.9: Median swimmer ascent velocity versus animal number density for each salinity condition (15, 17, 19, and 22 ppt). Due to differences in the number of swimmers the 15 and 22 ppt cases are compared and the 17 and 19 ppt cases are compared independently. Each data point corresponds to the median of one of the four replicate trials conducted per salinity condition, shaded areas represent the range of data between the 25th and 75 quantile .

Symbol	Variable	Value	Unit
u_z	swimming velocity	taken from data	cm/s
g	gravitational acceleration	9.8	m/s^2
V_s	swimmer volume	0.1	cm^3
ρ_s	swimmer density	1015	kgm^{-3}
ρ	seawater density	taken from data	kg m^{-3}
A_D	actuator disk area	20	cm

Table 3.1: Variables used in wake superposition model for induced flow in vertical migration.

To explore how induced flow scales with the dominant variables (number of swimmers, density difference, and swimming speed), we defined a dimensionless parameter, Λ, analogous to a Froude number, which compares inertial foces due to swimmer ascent speed with the buoyancy-driven momentum input from swimmer thrust. This dimensionless parameter characterizes the flow regime and determines the dominant physics:

$$\Lambda = \frac{\rho A_d u_z^2}{2N\Delta\rho g V_s,} << 1 \text{ [buoyancy-dominated]} \tag{3.7}$$

$$\Lambda = \frac{\rho A_d u_z^2}{2N\Delta\rho g V_s,} >> 1 \text{ [momentum-dominated]} \tag{3.8}$$

When $\Lambda << 1$, the buoyancy-driven thrust dominates over inertial corresponding to a low-speed regime, analogous to a low Froude number regime. Under these conditions, the scaling relationship for induced flow simplifies to

$$\Delta W \propto \sqrt{N\Delta\rho}. \tag{3.9}$$

At high swimmer ascent speeds, $\Lambda >> 1$, inertial forces associated with swimmer ascent speed dominate over buoyancy-driven thrust, indicating a momentum-dominated regime analogous to a high Froude number regime. In this limit, the swimmer-induced thrust term becomes small relative to the background velocity squared term, allowing a binomial approximation of the induced flow:

$$\Delta W = \frac{-u_z}{2} + \sqrt{\frac{u_z^2 + 2N\Delta\rho g V_{swimmer}}{\rho A_D}}. \tag{3.10}$$

We can rewrite this expression:

$$\Delta W = \frac{-u_z}{2} + \sqrt{\frac{u_z^2}{4}\left(1 + \frac{4N\Delta\rho g V_{swimmer}}{\rho A_D u_z^2}\right)}, \tag{3.11}$$

and factor out the now linear u_z term:

$$\Delta W = -\frac{u_z}{2} + \frac{u_z}{2}\sqrt{1 + \frac{4N\Delta\rho g V_{swimmer}}{\rho A_D u_z^2}}. \tag{3.12}$$

In the high-speed limit ($\Lambda >> 1$), the swimmer thrust term is very small compared to the swimmer speed term. Therefore, we can use the binomial approximation for small x in the form $\sqrt{1+x}$:

$$\sqrt{1+x} \approx 1 + \frac{x}{2}, \text{ when } |x| << 1. \tag{3.13}$$

Applying this to 3.12 gives the following:

$$\Delta W = -\frac{u_z}{2} + \frac{u_z}{2}\left(1 + \frac{4N\Delta\rho g V_{swimmer}}{\rho A_D u_z^2}\right). \tag{3.14}$$

$$\Delta W = \frac{N\Delta\rho g V_{swimmer}}{2\rho A_D u_z}. \tag{3.15}$$

$$\Delta W \propto \frac{N\Delta\rho}{u_z}. \tag{3.16}$$

All trials for the 15 ppt condition fall in the buoyancy-dominated regime. Therefore, although the median swimmer speed used in model predictions did not fully capture this skewed velocity distribution, the magnitude of the change would be trivial relative to the impact of the number of swimmers and buoyant forces, and if it explicitly accounted for slower swimmers, would theoretically yield even higher predictions of induced velocity. This outcome arises from the inverse relationship between the induced flow velocity and the swimmer ascent speed described by the actuator disk model scaling. However, this unexpected mismatch underscores a critical limitation in the actuator disk analogy as applied here: the model assumes uniform momentum transfer across the disk area, neglecting variations in wake interactions that occur due to swimmer velocity differences. In reality, swimmers moving at higher

ascent speeds produce stronger, more coherent wakes, potentially increasing local wake interactions and altering the scaling relationship between swimmer speed and induced flow velocity. Thus, the assumption of uniform momentum distribution fails to capture the increased complexity of hydrodynamic interactions within the collective migration, particularly in cases where swimmer velocity distributions are skewed or nonuniform.

Moreover, it is important to note that the dimensionless parameter Λ, which characterizes the relative importance of inertial versus buoyancy-driven momentum inputs, is calculated to be approximately unity for the 22 ppt condition. This places the experiment in a transitional regime, neither clearly buoyancy-dominated nor momentum-dominated. However, this calculation of Λ only accounts for swimmers within the 20 cm tall measurement section of the tank, omitting a significant number of swimmers distributed above and below this region within the full 1.2 m tank height. Including these additional swimmers would significantly increase the total buoyant force acting on the fluid, substantially reducing the value of Λ and placing the flow firmly within the buoyancy-dominated regime. This would consequently predict even higher induced flow velocities, thus amplifying the magnitude discrepancy between the measured flow and actuator disk predictions; however, this does not impact the qualitative match in trends as the actuator disk prediction has already been scaled. Despite these complexities and quantitative mismatches, qualitatively the actuator disk model effectively captures the fundamental relationship between the induced flow and key parameters such as buoyant force and the number of swimmers. Consequently, the observed trends support the theoretical scaling derived from the actuator disk framework, suggesting that for swimmers operating in the low-speed, buoyancy-dominated regime ($\Lambda \ll 1$), the induced flow velocity is expected to scale approximately with $(N\Delta\rho)^{1/2}$.

3.4 Discussion

This chapter investigated how variations in the buoyancy of an organism influence the hydrodynamic structures generated by collective vertical migrations. By modulating the buoyancy of brine shrimp through controlled variations in surrounding fluid density via fluid salinity, we quantified the effects on the induced flow velocity using simultaneous swimmer tracking and PIV. Our experimental results clearly demonstrate an inverse correlation between swimmer buoyancy and induced jet velocities.

The actuator disk model provided a theoretical framework that effectively captured experimental trends. However, discrepancies appeared at the lowest salinity tested (15 ppt). Here, the actuator disk model significantly overpredicted the experimentally measured induced flow velocities. This discrepancy likely arises from the skewed distribution of swimming speeds observed under these conditions, where many swimmers exhibited substantially slower ascent velocities than the median values used for model input. This suggests the importance of detailed swimmer velocity distributions rather than simplified representative statistics when predicting collective hydrodynamic phenomena.

Field measurements and modeling results [3, 22, 28, 30, 68, 69] estimate induced vertical flows on the order of a few centimeters per second during diel vertical migration. The nonlinear dependence of the induced flow velocity on density differences underscores how even modest environmental changes in the fluid density—on the order of 1-2% across ocean pycnoclines—can substantially influence the intensity of biologically driven mixing.

To facilitate a broader ecological and oceanographic application of these results, we define a nondimensional density difference parameter, $\Delta\rho^*$, using the average density of the ocean ($\rho_0 = 1036$ kg m^{-3}) [70] as a reference and selecting a swimmer's density to be equal to the densest parts of the ocean ($\rho_s = 1060$ kg m^{-3}) [70] so that the swimmer is always negatively buoyant. We then define

$$\Delta\rho^* = \frac{\rho_s - \rho}{\rho_s - \rho_0}. \tag{3.17}$$

The induced flow is similarly nondimensionalized by the baseline induced flow (ΔW_0):

$$W^* = \frac{\Delta W}{\Delta W_0}. \tag{3.18}$$

where ΔW_0 is calculated from 3.3 at the reference density condition. Therefore, W^* is 0 at the maximum ocean density (1060 kg m^{-3}) and 1 at the average ocean density (1036 kg m^{-3}). Based on the analysis above, the relationship between the induced velocity and normalized density can be described by the dimensionless parameter Λ, which is restated here.

$$\Lambda = \frac{\rho A_d u_z^2}{2N\Delta\rho g V_s}, \tag{3.19}$$

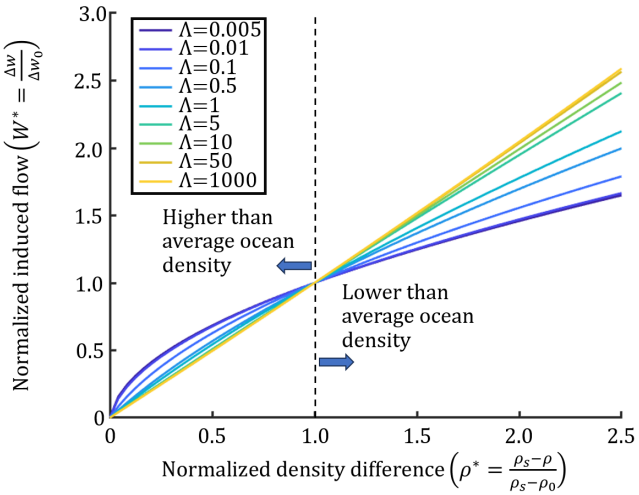

Figure 3.10: Normalized induced flow velocity, W^*, is plotted against the normalized density difference, ρ^*, illustrating how induced flow velocity changes across typical oceanographic density conditions. Curves are labeled with different values of the dimensionless parameter Λ, representing the relative importance of swimmer momentum versus buoyancy-driven thrust. The left region ($\rho^* < 1$) indicates fluid denser than the average ocean reference, resulting in reduced induced flows ($W^* < 1$). The right region ($\rho^* > 1$) corresponds to lighter fluid, enhancing induced flows ($W^* > 1$). Curves transition from buoyancy-dominated regimes ($\Lambda \ll 1$), scaling approximately as $(\Delta\rho^*)^{1/2}$, to momentum-dominated regimes ($\Lambda \gg 1$), exhibiting linear scaling with density difference.

which is analogous to a Froude number, compares the inertial forces due to the swimmer ascent speed with the buoyancy-driven momentum input from the swimmer thrust. The plot of normalized induced flow velocities, W^* against $\rho*$ at a varying order of magnitude of Λ, represents the transition from a buoyancy-dominated regime ($\Lambda \ll 1$), where induced flow scales as $(\Delta\rho^*)^{1/2}$, to an inertia-dominated regime ($\Lambda \gg 1$), where induced flow scales as $\Delta\rho^*$ (figure 3.10).

The induced flow velocity can be substantially reduced, approaching zero in significantly denser conditions such as in the deep ocean or strongly stratified regions. This highlights that field measurements taken in denser regions of the ocean would inherently underestimate the induced flows expected in more typical ocean conditions if extrapolated without adjustment. Conversely, induced flow velocities can increase significantly, linearly with changing density, however, is limited to up to 2.5 times greater based on the limits of realistic ocean densities. This means that extrapolating measurements from lighter-density environments would overestimate the mixing potential at average or deeper depths. Future studies could validate these

dimensionless scaling predictions using field data from vertical migration events across different ocean regions and densities.

However, it is worth noting that more complex distributions of swimmer speeds and positions could be explored, reflecting realistic aggregation heterogeneity, to further refine scaling relationships. The importance of spatial distribution is clear when examining the factors that impact Λ. The Lambda could be greatly skewered towards large numbers by artificially inflating A_d, the area of the actuator disk, and analogous to the width of the swarm. Although common sense in modeling would dictate that A_d would be defined as the minimum area to encompass all swimmers in the swarm, it is not explicitly defined as such and therefore an area of any size could be used.

In addition, there could be changes to swimming modes and behavior as a response to changing fluid density. Brine shrimp exhibit notable adaptability across diverse salinities, from dilute coastal waters to hypersaline inland lakes, which requires precise physiological control of buoyancy to manage dramatically variable water densities [71]. However, it is unknown how this directly affects their swimming behavior, body orientation, and stability. This could potentially be an additional factor contributing to the deviation between the flows measured in the later trials of the 15 ppt case and the flows predicted by the actuator disk model.

Chapter 4

MODELING OF INDUCED FLOW IN COLLECTIVE VERTICAL MIGRATION

[1] N. Mohebbi, J. Hwang, M. Fu, and J. Dabiri. "Measurements and modelling of induced flow in collective vertical migration". In: *Journal of Fluid Mechanics* 1001 (2024). *N.M., J.H., M.K.F., and J.O.D. designed research and were involved in discussions to interpret the results; N.M. performed research and analyzed results; M.K.F. developed the method and original analysis; J.H. wrote software and analyzed data; N.M. drafted the paper, and all authors helped edit and review.*, A50. DOI: 10.1017/jfm.2024.1102.

ABSTRACT

Hydrodynamic interactions between swimming or flying organisms can lead to complex flows on the scale of the group. These emergent fluid dynamics are often more complex than a linear superposition of individual-organism flows, especially at intermediate Reynolds numbers. This paper presents an approach to estimate the flow induced by multiple swimmer wakes in proximity using a semi-analytical model that conserves mass and momentum in the aggregation. The key equations are derived analytically, while the implementation and solution of these equations are carried out numerically. This model was informed by and compared with empirical measurements of induced vertical migrations of brine shrimp, *Artemia salina*. The response of individual swimmers to ambient background flow and light intensity was evaluated. In addition, the time-resolved 3-dimensional spatial configuration of the swimmers was measured using a recently developed laser scanning system. Numerical results using the model found that the induced flow at the front of the aggregation was insensitive to the presence of downstream swimmers, with the induced flow tending towards asymptotic beyond a threshold aggregation length. Closer swimmer spacing led to higher induced flow speeds, in some cases leading to model predictions of induced flow exceeding swimmer speeds required to maintain a stable spatial configuration. This result was reconciled by comparing two different models for the near-wake of each swimmer. The results demonstrate that aggregation-scale flows result from a complex, yet predictable interplay between individual organism wake structure and aggregation configuration and size.

4.1 Introduction

At low Reynolds numbers, Stokesian dynamics [72] can be used to estimate hydrodynamic interactions through linear superposition [73–75]. For organisms characterized by high Reynolds number dynamics, the linearity of potential flow theory allows for approaches based on linear superposition to estimate the combined effect of flow within a group [9, 76]. However, for swimmers operating in an intermediate Reynolds regime, such as the majority of vertically migrating swimmers in the ocean [12], neither Stokesian nor potential flow assumptions accurately capture the dominant hydrodynamic forces, resulting in nonlinear governing dynamical equations that are not readily suitable for linear superposition.

Although not strictly justified from first principles, superposition has been successfully applied to estimate wake interactions in wind farms without using potential flow assumptions. Initial efforts, exemplified by the linear superposition model proposed by Lissaman [77], assumed a large wind turbine spacing and weak wake interactions to linearly sum wake velocity deficits. Subsequent critiques highlighted the potential overestimates of the wake deficit within densely arranged wind turbine arrays, where there are significant wake interactions [78]. In response to this limitation, several alternative superposition methods have been proposed. Katic, Højstrup, and Jensen [79] posited that the combined velocity deficit in the wake overlap regions can be estimated by a sum of the squares of individual velocity deficits. Voutsinas, Rados, and Zervos [80] proposed a model that assumes that the total energy loss in the superposed wake is equal to the sum of the energy losses of each turbine upwind. Each of the aforementioned models demonstrated improved agreement with the measurement data, especially with stronger wake interactions. However, each model lacks a theoretical justification based on the conservation of mass and momentum in the wake. Recently, Zong and Porté-Agel [81] introduced a model that explicitly conserves mass and momentum in regions of wake overlap. This approach demonstrated superior performance over previous models compared with experimental and large-eddy simulation data.

Here, we adapt the approach of Zong and Porté-Agel [81] to develop an analytical model that estimates the 3-dimensional (3-D) flow induced by wake interactions of swimmers using brine shrimp as a model organism. The model was developed to conserve mass and momentum, drawing empirical parameters from the swimming trajectories of brine shrimp during induced vertical migration. We introduced an estimated convection velocity term to calculate mass flux in a linearized momentum

equation. This was used to develop an analytical wake superposition model based on each swimmer's local flow and the geometric configuration of the collective group.

We found supporting evidence to our experiments, showing that the induced flow can be significantly stronger than the flow associated with an individual swimmer. In addition, we found that the aggregate-scale induced flow was a function of the individual wake shape, length of the group, and animal number density. In addition,

4.2 Analytical model

Individual swimmer wake model

This section introduces an analytical model to compute the flow field generated by many individual wakes in close proximity while conserving mass and momentum. This method is inspired by the approach adopted by Zong and Porté-Agel [81] to superpose wind turbine wakes. Unlike previous formulations, which prescribe a drag coefficient and calculate momentum deficits, the present formulation prescribes the net force generated by the swimmers and calculates momentum excess. Importantly, this formulation did not assume a priori that the convective velocity would trend towards a plateau.

We assume that a vertical swimmer generates a downstream wake defined in the swimmer-fixed frame $u_w(x, y, z)$ to generate a net force F_z that counteracts negative buoyancy and thus maintains a constant swimming speed u_0 through a fluid with constant density ρ. These assumptions allow for the simplification of the integral form of the momentum equation,

$$F_z = \rho \iint_{wake} u_w(x, y, z)(u_w(x, y, z) - u_0)\ dxdy. \tag{4.1}$$

By introducing the wake velocity surplus, $u_s = u_w - u_0$, and substituting this definition into equation 4.1 we obtain the following:

$$F_z = \rho \iint_{wake} u_w(x, y, z)u_s(x, y, z)\ dxdy. \tag{4.2}$$

We introduce an effective wake convection velocity, $u_c(z)$, which varies with downstream distance from the swimmer, but is constant in the spanwise directions. Consequently, the net vertical force can be rewritten as

$$F_z = \rho u_c(z) \iint_{wake} u_s(x, y, z)\ dxdy. \tag{4.3}$$

The wake convection velocity effectively represents the average speed at which the local velocity surplus is advected in the wake of the swimmer. To derive a mathematical expression for u_c, we substitute 4.3 into 4.2 to get

$$u_c(z) = \frac{\iint_{wake} u_w(x,y,z)u_s(x,y,z)\ dxdy}{\iint_{wake} u_s(x,y,z)\ dxdy}. \tag{4.4}$$

The numerical evaluation of equation 4.4 is described in §4.3.

Wake superposition

To calculate the flow field at the aggregate scale, we define U_∞ as the swimming speed of all organisms in the volume, or the free stream velocity in a swimmer-fixed frame. Furthermore, we introduce $U_w(x,y,z)$ as the global flow field generated by the swimmers. Lastly, U_s is defined as the velocity surplus generated by the swimmers expressed as $U_s(x,y,z) = U_w(x,y,z) - U_\infty$. Following a procedure analogous to that in §4.2, the effective convection velocity of the combined wakes is given by the following:

$$U_c(z) = \frac{\iint U_w(x,y,z)U_s(x,y,z)\ dxdy}{\iint U_s(x,y,z)\ dxdy}. \tag{4.5}$$

The force exerted by the ith swimmer in the streamwise direction is denoted F_z^i. To conserve momentum in the wake, we require

$$\sum_i F_z^i = \rho U_c(z) \iint U_s(x,y,z)\ dxdy. \tag{4.6}$$

Substituting the left-hand side of 4.6 with 4.3 yields the following:

$$\sum_i \rho u_c^i(z) \iint u_s^i(x,y,z)\ dxdy = \rho U_c(z) \iint U_s(x,y,z)\ dxdy. \tag{4.7}$$

The velocity experienced by the ith organism is denoted u_0^i and defined as $U_w(x^i, y^i, z^i)$ based on upstream swimmers. The wake velocity induced by the ith organism is u_w^i, and the wake velocity surplus for the ith organism, u_s^i, is expressed as $u_w^i - u_0^i$. The

rearrangement of these terms and the subsequent application of the analysis across the entire volume lead to the derivation of an expression for the global wake surplus,

$$U_s(x, y, z) = \sum_i \frac{u_c^i(z)}{U_c(z)} u_s^i(x, y, z). \tag{4.8}$$

In light of 4.5, which describes U_c as a function of U_s and 4.8, which characterizes U_s as a function of U_c, an iterative methodology is used to solve for U_s and U_c. The procedure begins with the assumption $U_c = U_\infty$, where U_∞ denotes the velocity of the free stream. This is an underestimate, as U_c will increase from the free stream velocity with added momentum provided from the swimmers. Thus, in the first iteration, 4.8 is used to evaluate U_s, and will result in an overestimate since its value is inversely related to that of U_c. As the iterative process continues, this overestimate of U_s is used in 4.5 to refine the calculation of U_c, increasing the estimate from the initial guess. In this way U_c will continue increasing from the initial guess and U_s will continue decreasing until the value of U_c converges, satisfying condition $|U_c - U_c^*|/U_c^* \leq \epsilon$, where U_c is calculated from the preceding iteration, U_c^* is calculated from the ongoing iteration, and $\epsilon = 0.01$. The iterative development of local and global estimated convective velocities captures inherent nonlinearity and ensures the conservation of momentum in the establishment of the final 3-D flow field.

4.3 Modelling assimilation

Wake profile models

Two models for the individual wake structure were studied to explore the impact of local flow geometry on the aggregation-scale flow. The local flow was defined as a function of the radial distance, $r = \sqrt{x^2 + y^2}$, and the characteristic width of the wake, $\sigma(z)$, at each value of z. First, a Gaussian model was implemented, consistent with the wake models previously used for wind turbine modelling,

$$\xi_{gaussian}\left(\frac{r}{\sigma(z)}\right) = e^{-\frac{r^2}{2\sigma(z)^2}}. \tag{4.9}$$

Second, a Ricker wavelet model was used to represent a local flow both in the direction of swimming and in the opposite direction of swimming,

$$\xi_{wavelet}\left(\frac{r}{\sigma(z)}\right) = -\left(1 - \frac{r^2}{2\sigma(z)^2}\right) e^{-\frac{r^2}{3\sigma(z)^2}}. \tag{4.10}$$

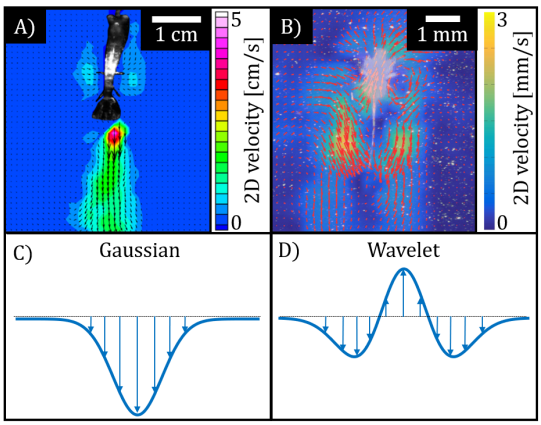

Figure 4.1: Comparative analysis of flow fields generated by different swimmer types and corresponding wake models. A) The PIV results showing the flow field generated by a single free-swimming Pacific krill, adapted from Catton et al. [2] with the permission of the *Journal of Experimental Biology*. The colour map represents the velocity magnitude, with arrows indicating flow direction. B) PIV results for a brine shrimp, highlighting the flow characteristics generated by its swimming motion, adapted from Wilhelmus and Dabiri [3], with the permission of AIP Publishing. C) A schematic representation of how a Gaussian distribution qualitatively captures the flow behind Pacific krill, which utilizes a single primary propulsor. D) A schematic representation of a wavelet model that qualitatively captures the flow behind a brine shrimp, characterized by two sets of propulsors and a drag region immediately behind the body that induces backflow. The panels illustrate the differences in flow structures arising from distinct swimming mechanisms and motivate the comparison between a Gaussian and wavelet wake superposition model.

These models will be referred to as the Gaussian and wavelet models, respectively. The Gaussian model, commonly employed in wind turbine modelling [81], represents the flow behind the swimmer as a single downward jet. As evidenced by the qualitative match between figure 4.1A and the schematic in figure 4.1C, the Gaussian wake function effectively captures the flow characteristics behind a swimmer utilizing a single main propulsor, generating a distinct single-lobed jet. The wavelet model, derived from the modified Ricker wavelet, is based on the second derivative of a Gaussian function, with an adjusted prefactor in the exponent denominator in order to create a function with a non-zero integral. As illustrated by the quantitative similarity between 4.1B and the schematic in figure 4.1D, the wavelet wake function captures the flow distribution generated by a swimmer with two sets of propulsive appendages, producing a double-lobed jet and a region of backflow immediately behind the swimmer due to the drag created by the body.

We modeled the spatial evolution of the propulsive jet as a self-similar, axisymmetric

jet,

$$u_s = u_0 \; c(z) \; \xi\left(\frac{r}{\sigma(z)}\right), \tag{4.11}$$

In the following derivation u_0, $\xi(r/\delta(z))$ and F_z are prescribed, and 4.11 is plugged into simplified momentum,

$$F_z = \rho \iint_{wake} u_w(x,y,z) u_s(x,y,z) \; dxdy, \tag{4.12}$$

to arrive at

$$F_z = \rho \iint u_0^2 \; \left(c(z) \; \xi(r,z) - [c(z) \; \xi(r,z)]^2\right) \; drd\theta, \tag{4.13}$$

to derive an expression for $c(z)$ that conserves momentum by definition. Next, $\xi(r/\delta(z))$ is defined as follows for each of the two wake models, and $\delta(z)$ is defined to be the standard deviation at each value of z, $\sigma(z)$. Note that when these functions are used in signal processing and analysis, a normalized version is used, ensuring that the total energy or power is conserved across different scales, which is important for accurate signal analysis. In this derivation, the prefactor $c(z)$ is constructed to conserve momentum directly, negating the need for commonly used normalization prefactors. To solve for $c_g(z)$ and $c_w(z)$, the prefactors for the Gaussian and wavelet wake models, respectively, the two wake shapes,

$$\xi_{gaussian}\left(\frac{r}{\sigma(z)}\right) = e^{-\frac{r^2}{2\sigma(z)^2}}, \tag{4.14}$$

$$\xi_{wavelet}\left(\frac{r}{\sigma(z)}\right) = -\left(1 - \frac{r^2}{2\sigma(z)^2}\right) \; e^{-\frac{r^2}{3\sigma(z)^2}} \tag{4.15}$$

are substituted into 4.13,

$$F_z = \rho \iint u_0^2 \; \left(c_g(z) e^{-\frac{r^2}{2\sigma(z)^2}} - \left(c_g(z) e^{-\frac{r^2}{2\sigma(z)^2}}\right)^2\right) \; drd\theta, \tag{4.16}$$

$$F_z = \rho \iint u_0^2 \; \left(c_w - \left(1 - \frac{r^2}{2\sigma(z)^2}\right) \; e^{-\frac{r^2}{3\sigma(z)^2}} - \left(c_w(z) - \left(1 - \frac{r^2}{2\sigma(z)^2}\right) \; e^{-\frac{r^2}{3\sigma(z)^2}}\right)^2\right) \; drd\theta \tag{4.17}$$

and then integrated in the streamwise direction over a circular cross-section with infinite radius. For each shape, there are two solutions for $c(z)$. We select the solution that is negative and tends to 0 with increasing positive z values,

$$c_g(z) = 1 - \sqrt{1 + \frac{F_z}{\pi\rho\sigma(z)^2 u_0^2}}, \tag{4.18}$$

$$c_w(z) = \frac{4}{5} - \frac{4}{5}\sqrt{1 + \frac{5F_z}{12\pi\rho\sigma(z)^2 u_0^2}}. \tag{4.19}$$

Combining 4.14 with 4.18 and 4.15 with 4.19 and plugging into 4.11 to derive the final expressions for u_s, as follows:

where $c(z)$ is a scaling factor and the shape of the wake is determined by $\xi(r/\sigma(z))$.

An expression for $c(z)$ that conserves momentum by definition was derived by prescribing u_0, $\xi(r/\sigma(z))$, and F_z

$$u_{s,gaussian}(x,y,z) = u_0\left(1 - \sqrt{1 + \frac{F_z}{\pi\rho\sigma(z)^2 u_0^2}}\right) e^{-\frac{r^2}{2\sigma(z)^2}}. \tag{4.20}$$

$$u_{s,wavelet}(x,y,z) = u_0\left(\frac{4}{5} - \frac{4}{5}\sqrt{1 + \frac{5F_z}{12\pi\rho\sigma(z)^2 u_0^2}}\right)\left(-1\left(-\frac{r^2}{2\sigma(z)^2}\right)\ e^{-\frac{r^2}{3\sigma(z)^2}}\right), \tag{4.21}$$

Finally, substituting the above equations 4.21 and 4.20 into the wake convection velocity, u_c,

$$u_c(z) = \frac{\iint_{wake} u_w(x,y,z)u_s(x,y,z)\ dxdy}{\iint_{wake} u_s(x,y,z)\ dxdy}, \tag{4.22}$$

integrating in the streamwise direction over a circular cross section with infinite radius, the expressions for u_c are obtained.

$$u_{c,gaussian}(z) = \frac{u_0}{2}\left(1 + \sqrt{1 + \frac{F_z}{\pi\rho\sigma(z)^2 u_0^2}}\right). \tag{4.23}$$

Symbol	Variable	Value	Unit
U_∞	swimming velocity	1	cm/s
g	gravitational acceleration	9.8	m/s^2
V_s	swimmer volume	0.2	cm^3
ρ_s	swimmer density	1055	kg m^{-3}
ρ	seawater density	1025	kg m^{-3}
L_s	body length	1	cm

Table 4.1: Variables used in wake superposition model for induced flow in vertical migration.

$$u_{c,wavelet}(z) = \frac{u_0}{2}\left(1 + \sqrt{1 + \frac{5F_z}{12\pi\rho\sigma(z)^2 u_0^2}}\right), \tag{4.24}$$

A swimmer moving vertically at constant velocity must overcome the negative buoyancy that arises from the swimmer having a greater density, ρ_s, than sea water. The balance of force on the swimmer is expressed as follows:

$$F_{thrust} = gV_s(\rho_s - \rho) \tag{4.25}$$

The thrust is introduced over some distance and not at an exact point in the flow. Therefore, we amended this expression to

$$F_{thrust}(z) = gV_s(\rho_s - \rho)\frac{1 + \mathrm{erf}\left(\frac{z}{L_s}\right)}{2}, \tag{4.26}$$

for a more gradual development of the wake, where L_s is the length of the swimmer's body length (BL). Similarly, an empirical model for the effective diameter of the wake as a function of the streamwise distance from the swimmer was used to capture the wake expansion,

$$\sigma(z) = 0.25 + 0.25\log(1 + e^{(z-1.5)/L_s}) \tag{4.27}$$

The variables defined for the numerical implementation of this wake model are listed in table 4.1. These values were approximated to be of the order of observations made during laboratory experiments using brine shrimp. We normalize all length measurements by the BL of a swimmer, L_s.

Collective flow field calculations

Model flow fields for various swimmer configurations were calculated to identify the impact of aggregate characteristics on induced flow. First, changes due to group length were examined. The length of the group was increased in each test, while animal number density and width remained constant (table 4.2A). To maintain constant animal number density and width of the group, the number of swimmers increased linearly with increasing length of the group. Second, to test the impact of animal number density on the resulting flow, the number of swimmers and the length of the group were kept constant while increasing the cross-sectional area in the spanwise dimensions (table 4.2B). This resulted in an animal number density that decreased with increasing width as $1/W^2$, where W is the width of the group. For each calculation with a selected set of parameters, three iterations of swimmers were placed randomly with these specifications while maintaining a minimum nearest neighbour distance of one BL

4.4 Results

The parameters derived experimentally above were used to inform the wake models for the individual swimmers. These modeled wakes were then applied to various swimmer configurations using the wake superposition framework from §4.2 to characterize the collectively induced flow. All calculations were done in the swimmer-fixed reference frame. However, for the sake of clarity, the results presented here are depicted and discussed in the laboratory-fixed frame.

Dependence on aggregation size

In the first set of calculations, we examine the flow induced by groups with the same animal number density, 0.4 animals per BL^3, but different lengths (figure 4.2). Three configurations of each group length were generated with randomly placed swimmers. The average convection velocity and standard deviation of each group length was plotted (figure 4.3). The convection velocity generated within the groups were found to overlap each other. This indicated that the upstream portion of the flow generated within a group was not affected by the downstream flow. Furthermore, the induced flow ceased to exhibit a discernible dependence on the group length beyond a certain threshold, estimated at around 20-30 BL in this case. Consequently, we found that the dynamics of both longer and shorter groups can be approximated by studying the flow generated by any group longer than this threshold length.

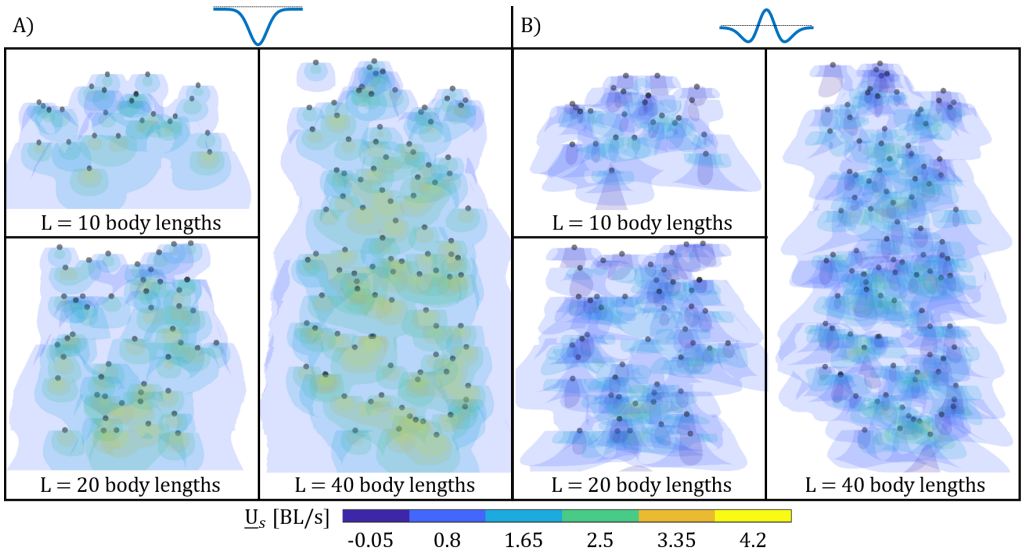

Figure 4.2: The 2-D projection of group geometry and induced flow contour map for groups with an animal number density of 0.2 animals per BL^3, shown for increasing group lengths. Black spheres represent positions of swimmers. Five isosurfaces of the 3-D flow field output generated from the semi-analytical model are superimposed, with the colour indicating the flow magnitude. Results are shown side by side from A) the Gaussian model and B) the wavelet model.

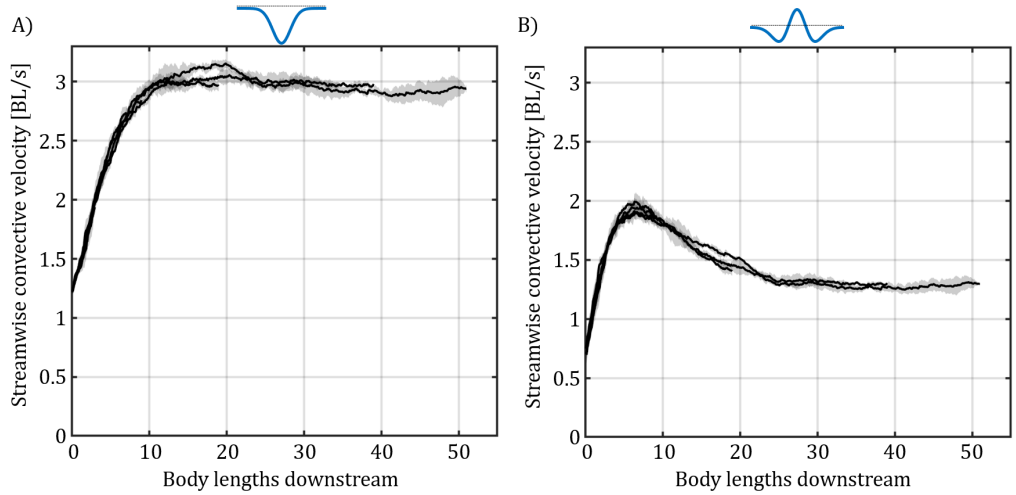

Figure 4.3: Laboratory frame convection velocity, $U_c(z) - U_\infty$ measured in BL s^{-1}, plotted against streamwise distance from start of group, z. Each plot represents three randomized iterations, with the line indicating the average value and the shaded areas indicating the standard deviation. Results for five group lengths (4, 10, 20, 40, and 52 BL) are superimposed for comparison using A) the Gaussian model and B) the wavelet model.

A)	Length tests			
Test	Number (N)	Length (L)	Width (W)	Number density
	swimmers	body length	body length	swimmers/body length^3
1	40	4	5	0.4
2	100	10	5	0.4
3	200	20	5	0.4
4	400	40	5	0.4
5	520	52	5	0.4

B)	Animal number density tests			
Test	Number (N)	Length (L)	Width (W)	Number density
	swimmers	body length	body length	swimmers/body length^3
1	100	20	2.2	1
2	100	20	3	0.6
3	100	20	4	0.3
4	100	20	7	0.1
5	100	20	10	0.05
6	100	20	19	0.01

Table 4.2: Parameters to be examined are the number of swimmers in the group, N, the length of the group, L, and the width of the group, W. Together, these three parameters result in a group metric that we refer to as the animal number density, measured in animals per BL^3 and calculated as $N/(W^2L)$. These parameters are used to examine the impact of changes in A) group length, and B) animal number density.

Dependence on swimmer spacing

In the second set of simulations, we investigate the influence of swimmer spacing on the flow generated by the collective. We randomly placed 100 swimmers within a volume of constant length but varying widths, resulting in changes in animal number densities (figure 4.4). Three simulations were initiated for each case. Although the truncated swarm length results in less distinct asymptote values, a positive correlation between induced convective flow and animal number density was observed (figure 4.5). Specifically, for groups with animal number densities exceeding 0.05 animals per BL^3 using the Gaussian model, a consistent trend emerged: the flow increased steadily with length until reaching a threshold length, beyond which the dependence on length decreased to a near-stable state. Groups with animal number densities below 0.05 animals per BL^3 with the Gaussian model and all number densities for the wavelet model exhibited peak flow early in the aggregation process,

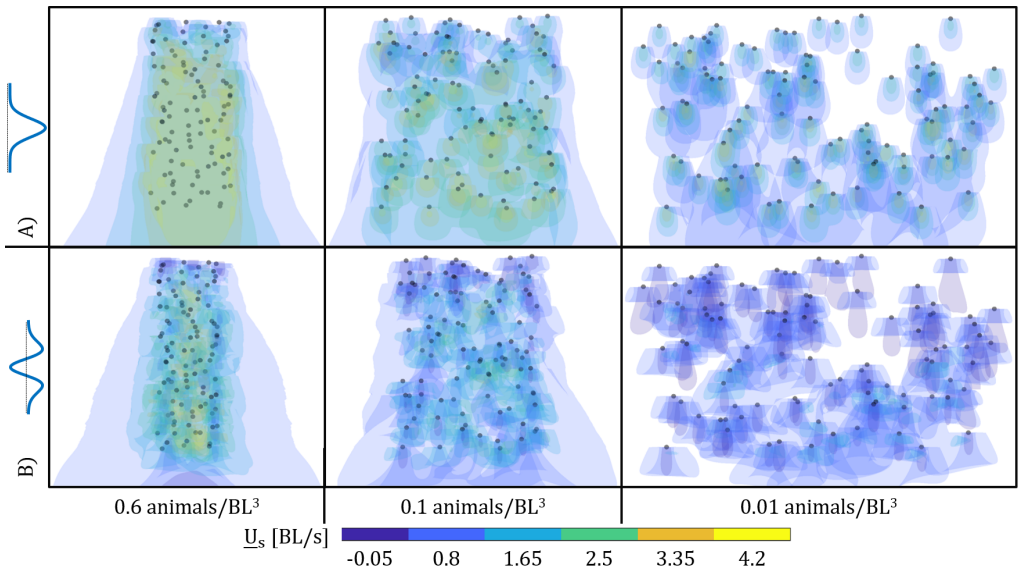

Figure 4.4: 2-D projection of group geometry and induced flow contour map for 100 swimmers with increasing group width, resulting in decreasing animal number density. Black spheres represent positions of swimmers. Five isosurfaces of the 3-D flow field output generated from the semi-analytical model are superimposed, with the colour indicating the flow magnitude. Results are shown side by side from A) the Gaussian model and B) the wavelet model.

followed by substantial decreases in flow. For the sparsest cases, 0.01 animals per BL^3, the flow at 25 BL downstream was lower than that generated at the beginning of the aggregation. In all cases, at some threshold length, the dependence of flow on length is greatly reduced.

We also observe that in many cases the estimated convection velocity exceeds the velocity prescribed to swimmers in this model, which was set at 1 BL s^{-1}. Although this model captures an instantaneous snapshot in time for a specific configuration of swimmers, in reality, swimmers facing a flow exceeding 1 BL s^{-1} would be pushed in the opposite direction to their swimming motion. Thus, these configurations are paradoxical since we have initialized a configuration of swimmers that creates a flow that would make this animal number density impossible to maintain.

To further investigate the stability of the aggregation, we analysed the flow experienced by individual swimmers within the collective. The distribution of flow velocities for varying animal number densities (figure 4.6) revealed that a significant proportion of swimmers in groups denser than 0.1 animals per BL^3 experience a flow exceeding 1 BL s^{-1} per second. The magnitude and range of these flows experienced, especially in denser groups, indicate an unsustainable configuration.

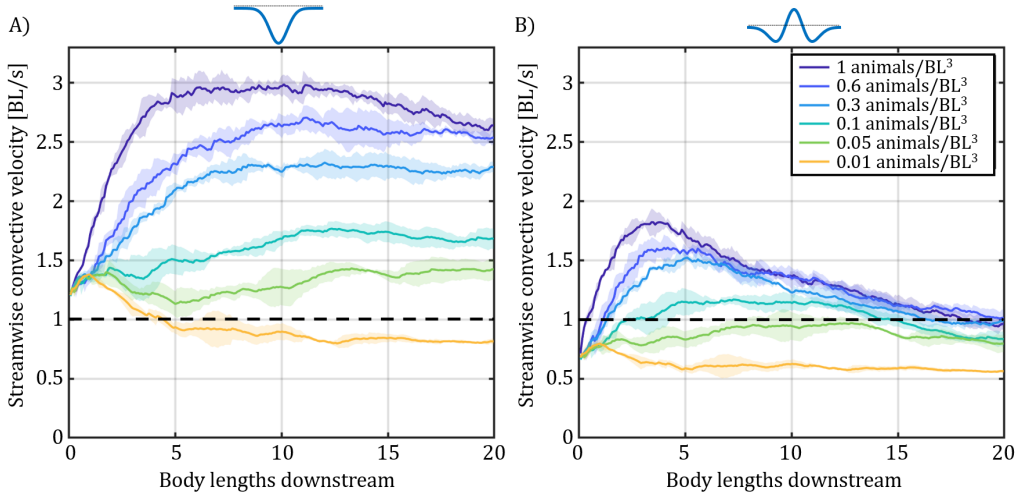

Figure 4.5: Laboratory frame convection velocity, $U_c(z) - U_\infty$ measured in BL s^{-1}, plotted against streamwise distance from start of group, z. Each plot represents three randomized iterations, with the line indicating the average value and the shaded areas indicating the standard deviation. Six animal number densities (0.01, 0.05, 0.1, 0.3, 0.6, and 1 animal per BL^3) are plotted with A) the Gaussian model and B) the wavelet model. DA dashed line indicates the swimming speed prescribed in the model, set at 1 BL s^{-1}.

In this type of individual scale analysis, we observe that in flows generated with the wavelet wake model, some swimmers experience a negative flow, getting a boost by being in the drag-dominated region of an upstream swimmer. It follows that it is also important to examine the flows experienced in relation to the position within the swarm, which may contribute to the range of flow velocities observed between swimmers.

Comparison with experimental data

In all previous simulations, the swimmers were randomly placed within specified parameters. To provide context to these findings, we conducted a test by initializing the computational model with three swimmer configurations obtained by 3-D PTV of induced brine shrimp migrations from chapter 2. We used three cases in which 100 brine shrimp were scanned and reconstructed within the volume (L= 22 cm, W_1= 6.6 cm, W_2= 22 cm), resulting in an animal number density of 0.03 animals per BL^3 (figure 4.7). This was compared with three simulations initialized with the same volume and number of swimmers, placed randomly. Figure 4.8 shows that the flow derived from the simulation with experimentally obtained swimmer configuration resulted in a higher convection magnitude than the randomly initialized simulations.

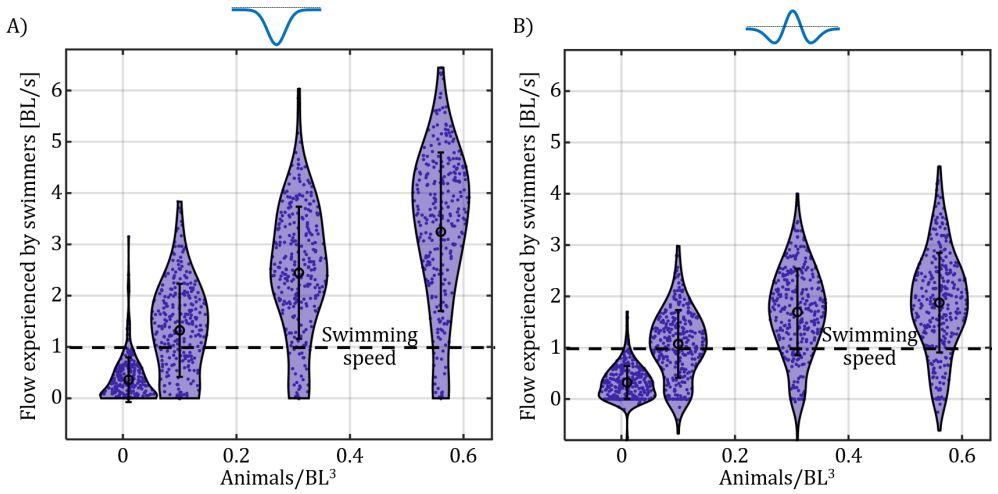

Figure 4.6: Distribution of flow experienced by swimmers, $u_0^i - U_\infty$, at different animal number densities. The distributions are shown using A) the Gaussian model and B) the wavelet model.

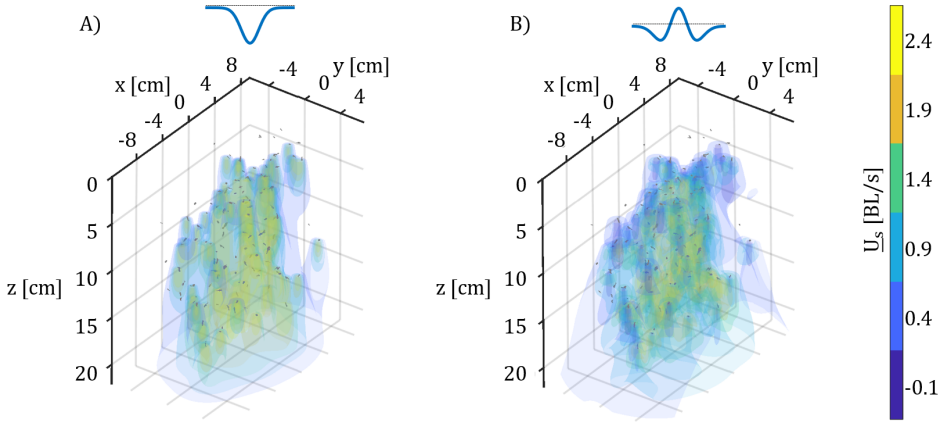

Figure 4.7: Scanned and reconstructed brine shrimp from 3-D PTV overlaid with flow field, $U_s(x, y, z)$ generated by A) the Gaussian wake model and B) the wavelet wake model.

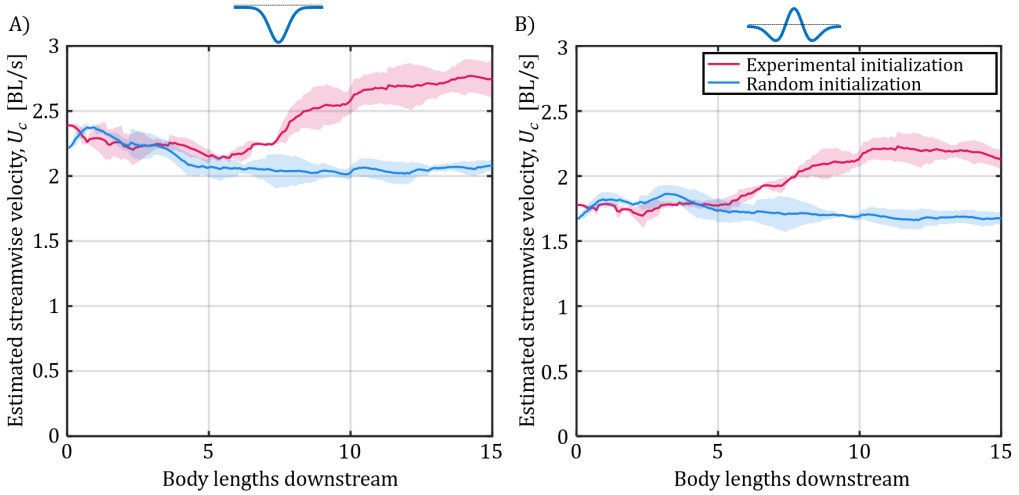

Figure 4.8: Comparing convective velocity generated by randomly distributed swimmer locations and experimentally initialized swimmer locations using A) the Gaussian model and B) the wavelet model. Estimated convection velocity plotted against streamwise distance from start of group, z for randomized simulations and for a simulation initialized with locations of brine shrimp during induced vertical migration.

A portion of this difference can be attributed to the fact that the animal number density is overly generalized, failing to capture the spatial variations in the swimmers' configuration. As shown in figure 4.9, the concentration of swimmers is significantly higher towards the centre of the tank when experimentally initialized. The increased concentration in the centre of the volume likely results in more frequent swimmer wake interactions, leading to larger induced flow. While it may not be surprising, given that the flashlight was centrally positioned in the tank, attracting the brine shrimp towards the light, it is noteworthy that the swimmers do not avoid or alter their swimming paths to mitigate the higher flow regions created by these interactions.

To further explore the relationship between animal number density and the induced flow velocity, we plotted induced flow from experimental data in Houghton and Dabiri [4] against the computational simulations on a normalized scale (figure 4.10). This comparison highlights the scaling behaviour of the induced flow as a function of animal number density. While the magnitudes differ, the general trend is consistent across the experimental and simulated data. The power law fit was calculated as $y = ax^b + c$, where b controls the rate at which induced flow velocity changes as a function of animal number density. By comparing the values of b between the experimental ($b = 0.61$) and simulated datasets (Gaussian, $b = 0.5$;

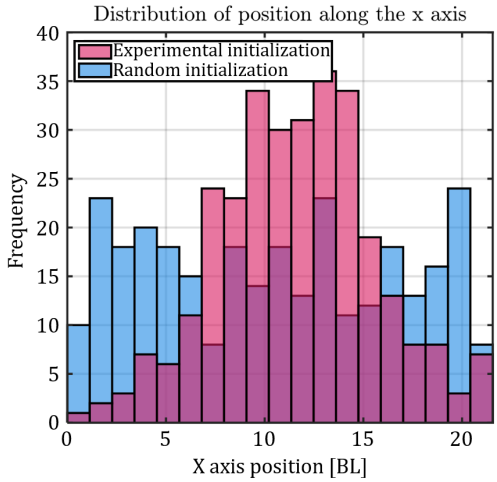

Figure 4.9: Comparison of the distribution of swimmer positions between experimentally initialized (pink bars) and randomly initialized groups (blue bars). Swimmers in the experimental set-up are concentrated in the centre, while those initialized randomly are distributed more evenly throughout the volume. The illuminated positions in the tank correspond roughly to the region between $X = [7, 13]$.

wavelet, $b = 0.3$), we see that the Gaussian wake model produces flow magnitude growth rates with animal number density.

4.5 Discussion

We have developed an analytical wake superposition model for groups of hydrodynamically interacting organisms. This model was implemented numerically with parameters derived from empirical observations of brine shrimp, incorporating observed responses to light and flow as well as 3-D swimming trajectories. Numerical simulations with this model produce a 3-D flow field and an estimated convection velocity. This semi-analytical model provides a quantitative framework for understanding hydrodynamic interactions within swimming aggregations at intermediate Reynolds numbers.

Our findings highlight the intricate interplay between wake kinematics, swimmer spacing, and overall group size and arrangement in inducing flows within swimming collectives. Notably, the wavelet wake model, when compared with the Gaussian wake model, generates lower-magnitude convective velocities, resulting in swimmers within the group experiencing slower flows. The positive flow regions in the wavelet have an annular shape with the maximum flow value reached over a circle in space. In contrast, the Gaussian wake reaches a maximum value at a single point. Thus, the wavelet model has a more spread-out region of positive flow. In

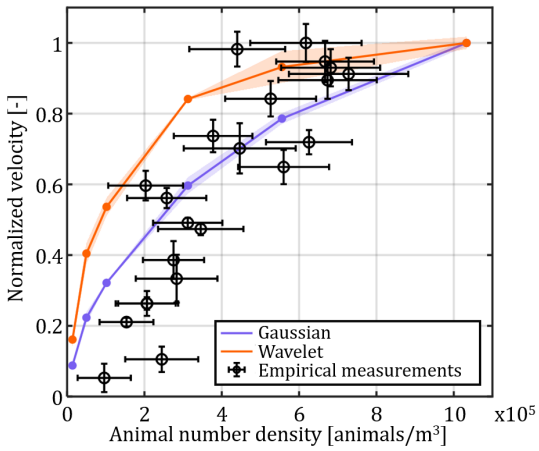

Figure 4.10: Comparison of normalized velocity induced by varying densities of swimmers between experimental data and model predictions. Normalized flow velocity as a function of animal number density, comparing experimental data from Houghton and Dabiri [4] (black circles with standard deviation bars) with the average and standard deviation (shaded area) from triplicate simulations at corresponding densities using the Gaussian and wavelet models.

addition, the negative flow region was averaged when looking at the convective velocity. The differences between the flow induced by Gaussian and wavelet wake models exemplify the importance of local flow kinematics and thus motivate continuing work to measure and model individual organism-level flows. Compared to experimental data, the wavelet model predicts flow magnitudes in closer quantitative agreement; however, when normalized by the maximum flow, the Gaussian model more effectively captures the dependence on animal number density.

By comparing groups of different lengths, we found that the flow within the group exhibits decreased sensitivity to the length of the group beyond a threshold. With a uniform distribution of swimmers, there was a constant infusion of momentum to the flow with streamwise distance from the start of the group. However, the velocity of the induced flow increases within the group length only until the mass flux term of the momentum balance dominates, and each individual adds less velocity to the flow than those upstream. The impact of this added velocity decreases further with diffusion before reaching downstream swimmers. In addition, we found that the upstream portion of the flow within the group was not affected by the group downstream. Thus, the dynamics of shorter groups can be extracted from the dynamics of groups longer than a certain threshold.

Simulating different group densities, we found that the collective convective ve-

locity increased with the animal number density. Dense configurations resulted in flows that exceeded the swimming speed of the organism, resulting in unstable structures. This observation raises questions about the apparent stability of swimmer aggregations in field observations, where these high-density configurations are known to persist. The contrast between simulated results and observed natural behaviour prompts inspiration for future model improvements to explore mechanisms used by organisms to navigate and thrive in environments characterized by dynamic collective swimming. For example, there is evidence that animals exploit fluid structures to improve locomotion [82, 83]. In randomized simulations, positions were initialized by placing swimmers in a prescribed volume swimming directly upward. For vertically swimming negatively buoyant swimmers, momentum excess in the vertical direction is a reasonable generalization. To extend this model beyond constant-speed, unidirectional swimming, the impact of non-aligned trajectories and flow-response behaviours is needed. Similar models for wind turbines have found that wake deflection impacts wake spreading and thus affects aggregate flow characteristics [84]. However, applying these methods to animal behaviour and modelling requires further investigation to determine the suitability. The only constraint in swimming placement was the exclusion zones that maintain a minimum nearest neighbour distance. If the model included some parameters to actively optimize swimmer placement, downstream swimmers might seek the drag region of a wavelet wake or avoid peak flows of a Gaussian wake. Continued work to study the stability of these systems could incorporate discrete time step dynamics to investigate how collective flow-inducing systems evolve.

This model is adaptable to different wake profiles and aggregation configurations, allowing future exploration of flows generated by other organisms with different wake profiles and collective behaviors. The current formulation explicitly represents negatively buoyant swimmers that produce sufficient thrust to overcome gravity, resulting in wakes characterized by a net vertical momentum surplus. However, the wavelet wake shape, in particular, reembles a potentially momentumless condition because of its region of momentum surplus and deficit. In a momentumless wakes—where thrust and drag precisely balance, resulting in zero net momentum downstream—while still generating some wake structure [85–87]. Extension to this case, however, may require adjustments to the numerical convergence strategy.

Chapter 5

CONCLUSION

> *"When we try to pick out anything by itself, we find it hitched to everything else in the Universe."*
>
> – John Muir, *My First Summer in the Sierra, 1911*

The 3D scanning method in Chapter 2 revealed that swimmers consistently maintained dominant and consistent upward vertical velocities across varying environmental conditions, simplifying further modeling assumptions. Detailed trajectory analysis identified distinct types of turning behaviors among swimmers. Although these turning behaviors were not globally coordinated, they demonstrated clear spatial dependence, enhancing an understanding of individual-level dynamics within collective swimming aggregations. The inward radial movement, likely driven by phototaxis, balanced with dispersive behaviors, resulted in a Gaussian-like spatial distribution. However, the co-location of variables like light intensity, flow speed, swimmer density, and velocity variability made distinguishing specific causal relationships challenging.

Changing swimmer buoyancy through controlled environmental salinity manipulations, revealing an inverse correlation between swimmer buoyancy and induced jet velocities. In particular, deviations from the actuator disk model predictions under low salinity conditions may highlight critical limitations related to spatial averaging. The semi-analytical model (Chapter 4) provided context for these deviations, explicitly demonstrating the dependence of induced flow on spatial distributions of individual wakes and swimmer arrangements. These findings underscore the necessity of moving beyond spatial averaging toward detailed spatial analyses when modeling collective hydrodynamics.

The semi-analytical wake superposition model developed in Chapter 4 allowed precise control over parameters such as wake shape, swimmer number, spatial distribution, and group configuration. Despite this control, inherent parameter coupling was still observed. Maintaining animal density while varying group length required adjustments in swimmer numbers, while altering animal densities with a fixed number of swimmers required changes in volume. Crucially, spatial distri-

bution significantly affected collective hydrodynamics, with apparent differences observed between wavelet and Gaussian wake models. These analyses emphasized the critical role of the spatial structure and the inadequacy of spatial averaging for capturing detailed hydrodynamic interactions.

The findings highlight the intricate interplay between swimmer behaviors, spatial distributions, and environmental parameters in shaping collective hydrodynamic outcomes. The research emphasizes the challenges and necessity of integrating detailed spatial structure into experimental and theoretical frameworks to accurately capture collective swimming.

To contextualize the magnitude of the induced vertical flows measured during collective vertical migration in our laboratory experiments, it is useful to consider typical swimming capabilities documented for organisms performing DVM. Typical migration speeds for small marine organisms, normalized by body length (BL), provide a biologically meaningful reference. Small copepods (1–5 mm body length) migrate at sustained vertical speeds ranging approximately from 0.2 to 2 BL/s. Larger organisms such as krill (2–6 cm body length) commonly sustain cruising speeds between about 0.5 and 2 BL/s during DVM [88].

The induced vertical flows measured in our experiments are approximately an order of magnitude lower, though highly dependent on the number of swimmer and fluid density. This clear difference indicates that the flows generated by collective swimmer interactions in our experiments, while notable, remain modest relative to typical swimming speeds. Thus, these induced flows would likely not significantly impede vertical migration in natural settings.

Typical oceanic zooplankton such as copepods and krill migrate under intermediate Reynolds numbers ranging from 10 to 1000 [89–91], placing them within a regime characterized by laminar to transitional flows, consistent with brine shrimp swimming. The dimensionless buoyancy parameter, Λ, reflects the balance between inertia (due to swimming speed) and buoyancy-driven momentum transfer and is an analog to the Froude number. Oceanic observations suggest that zooplankton operate primarily in buoyancy-dominated to transitional regimes (Λ from 1 to 100) [18, 92]. Our experiments in which Λ is approximately unity represnet a transitional balance between inertial and buoyant forces.

The aspect ratio (height/width) of oceanic zooplankton aggregations typically ranges from about 0.03 to 0.2. Field acoustics show that small, compact swarms can be

somewhat thicker relative to their width, whereas large-area aggregations form very "flat" layers [93, 94]. In our laboratory setting, swimmer distributions formed similarly thin layers, strongly resembling the Gaussian distribution observed in field studies of plankton swarms. Our experiments have an aspect ratio of 5 using the height of the tank and width of scanning window. Packing fractions in the ocean rarely exceed 1%, typically ranging from 0.001% to around 0.1%. Our experiments, though slightly denser (reaching fractions on the order of 0.1%–1%). Lastly, the ratio of vertical migration distance to the swimmer body length typically falls between 10^5 and 10^3 [95, 96], our experiments are about 100. So the physics of intermediate Reynolds swimming in buoyancy-dominated to transitional regimes aligns well with our experiments. However, the geometry of the swarm, such as aspect ratio, distance traveled, and packing fraction, differs from those observed in DVM. However, development of the semi-analytical chapter allows for experimentation with a wide range of these geometric characteristics.

5.1 Opportunities for further exploration

Future experiments could benefit from longer-duration and higher-resolution recordings. The initial use of a high-speed camera operating at 10,000 fps was chosen without a priori knowledge of scanning constraints. As the experiments evolved, accurate tracking was achieved at significantly lower frame rates (2000 fps), suggesting that lower-cost imaging systems or real-time streaming architectures could be used to extend recording times without sacrificing resolution. Longer data obtained from 3-D scanning could be used to further classify and characterize swimming behavior. Advanced statistical modeling, machine learning techniques, and behavioral phenotyping methods can distinguish subtle patterns and their ecological implications, offering more profound insights into swimmer-environment interactions.

Once most of the swimmers have reached the top of the tank, a dense aggregation forms near the free surface. All measurements presented in this thesis were taken prior to the onset of this free surface interaction region to avoid associated boundary effects. However, in observations beyond the measurement window, swimmers are frequently seen being swept downward in large groups. These qualitative observations, while not captured in the quantitative dataset, may provide useful context for interpreting the results of the semi-analytical model, particularly the regimes in which the induced flow speed exceeds the prescribed swimmer speed. However, the maximum flow measurements in this thesis are around 0.4 BL s^{-1} which is nearly an order of magnitude less than the maximum swimming speed observed in the dis-

tributions of vertical swimming speeds with no flow (4 BL s^{-1} figure A.1). So, in addition to hydrodynamic explanations, behavioral transitions may also contribute to this phenomenon. Possible factors include unmeasured changes in metachrony, reduced swimming efficiency due to crowding or fatigue, or decreased response resulting from limited access to the light source.

Capturing these transitions would likely require higher spatial resolution tracking targeted at the later stages of the migration. Higher spatial resolution over shorter time windows could allow for detailed quantification of fine motor behaviors, such as pleopod motion or changes in metachrony, as indicators of dynamic behavioral states. With current technology, these two directions, prolonged duration or enhanced spatial resolution, are trade-offs in camera capabilities and data handling.

In addition, simple behavioral manipulations may allow for independent control of parameters and isolation of specific causal relationships. For example, since swimmers are positively phototactic, different lighting shapes, spreads, and structures could manipulate behavior without directly impacting the flow or swimmers. This would help contextualize the results from Chapter 3 and elucidate causal relationships from the currently drawn correlations. Furthermore, field measurements of biogenic mixing during DVM events could be contextualized with the nondimensional parameter lambda and the density of the fluid at the time of measurement to better determine the flows ranges generated by these events on a larger scale.

For the developed semi-analytical model, future work could expand the model to include non-aligned trajectories and active behavioral responses to local flow structures. Insights could be drawn from wind turbine wake modeling methodologies to study wake deflection and its implications for collective flow dynamics. Further incorporating discrete time-step dynamics would enhance the model's realism and clarify how swimmer distributions and flow interactions evolve and stabilize over time.

Ultimately, rigorous field measurements remain crucial for contextualizing and validating these laboratory and theoretical insights. Comprehensive field validations in diverse ecological conditions are essential to ensure the ecological relevance and broader applicability of our findings. Integrating such empirical field data with laboratory and theoretical approaches will create a robust framework capable of accurately capturing the complexity and variability inherent in natural collective swimming phenomena.

BIBLIOGRAPHY

[1] M. K. Fu, I. A. Houghton, and J. O. Dabiri. "A single-camera, 3D scanning velocimetry system for quantifying active particle aggregations". en. In: *Experiments in Fluids* 62.8 (Aug. 2021), p. 168. ISSN: 0723-4864, 1432-1114. DOI: 10.1007/s00348-021-03256-x. URL: https://link.springer.com/10.1007/s00348-021-03256-x (visited on 06/09/2022).

[2] K. B. Catton et al. "The hydrodynamic disturbances of two species of krill: implications for aggregation structure". In: *Journal of Experimental Biology* 214.11 (June 2011), pp. 1845–1856. ISSN: 0022-0949. DOI: 10.1242/jeb.050997. URL: https://doi.org/10.1242/jeb.050997 (visited on 05/29/2022).

[3] M. M. Wilhelmus and J. O. Dabiri. "Observations of large-scale fluid transport by laser-guided plankton aggregationsa)". In: *Physics of Fluids* 26.10 (Sept. 2014), p. 101302. ISSN: 1070-6631. DOI: 10.1063/1.4895655. URL: https://doi.org/10.1063/1.4895655 (visited on 01/11/2024).

[4] I. A. Houghton and J. O. Dabiri. "Alleviation of hypoxia by biologically generated mixing in a stratified water column". en. In: *Limnology and Oceanography* 64.5 (2019). _eprint: https://onlinelibrary.wiley.com/doi/pdf/10.1002/lno.11176, pp. 2161–2171. ISSN: 1939-5590. DOI: 10.1002/lno.11176. URL: https://onlinelibrary.wiley.com/doi/abs/10.1002/lno.11176 (visited on 08/10/2022).

[5] P. Anderson. "More Is Different". en. In: *Science* 177 (1972).

[6] J. K. Parrish and L. Edelstein-Keshet. "Complexity, Pattern, and Evolutionary Trade-Offs in Animal Aggregation". In: *Science* 284.5411 (Apr. 1999). Publisher: American Association for the Advancement of Science, pp. 99–101. DOI: 10.1126/science.284.5411.99. URL: https://www.science.org/doi/10.1126/science.284.5411.99 (visited on 10/04/2023).

[7] T. Vicsek and A. Zafeiris. "Collective motion". In: *Physics Reports*. Collective motion 517.3 (Aug. 2012), pp. 71–140. ISSN: 0370-1573. DOI: 10.1016/j.physrep.2012.03.004. URL: https://www.sciencedirect.com/science/article/pii/S0370157312000968 (visited on 10/13/2023).

[8] H. Ko, G. Lauder, and R. Nagpal. "The role of hydrodynamics in collective motions of fish schools and bioinspired underwater robots". en. In: *Journal of The Royal Society Interface* 20.207 (Oct. 2023), p. 20230357. ISSN: 1742-5662. DOI: 10.1098/rsif.2023.0357. URL: https://royalsocietypublishing.org/doi/10.1098/rsif.2023.0357 (visited on 10/22/2024).

[9] D. Weihs. “Hydromechanics of Fish Schooling”. en. In: *Nature* 241.5387 (Jan. 1973). Number: 5387 Publisher: Nature Publishing Group, pp. 290–291. ISSN: 1476-4687. DOI: 10.1038/241290a0. URL: https://www.nature.com/articles/241290a0 (visited on 11/02/2023).

[10] I. Ashraf et al. “Simple phalanx pattern leads to energy saving in cohesive fish schooling”. In: *Proceedings of the National Academy of Sciences* 114.36 (Sept. 2017). Publisher: Proceedings of the National Academy of Sciences, pp. 9599–9604. DOI: 10.1073/pnas.1706503114. URL: https://www.pnas.org/doi/10.1073/pnas.1706503114 (visited on 05/14/2025).

[11] A. J. T. M. Mathijssen et al. “Collective intercellular communication through ultra-fast hydrodynamic trigger waves”. en. In: *Nature* 571.7766 (July 2019). Number: 7766 Publisher: Nature Publishing Group, pp. 560–564. ISSN: 1476-4687. DOI: 10.1038/s41586-019-1387-9. URL: https://www.nature.com/articles/s41586-019-1387-9 (visited on 11/01/2023).

[12] K. Katija. “Biogenic inputs to ocean mixing”. eng. In: *The Journal of Experimental Biology* 215.Pt 6 (Mar. 2012), pp. 1040–1049. ISSN: 1477-9145. DOI: 10.1242/jeb.059279.

[13] Y. Zhang and G. V. Lauder. “Energetics of collective movement in vertebrates”. In: *Journal of Experimental Biology* 226.20 (Oct. 2023), jeb245617. ISSN: 0022-0949. DOI: 10.1242/jeb.245617. URL: https://doi.org/10.1242/jeb.245617 (visited on 11/06/2023).

[14] F. Berlinger, M. Gauci, and R. Nagpal. “Implicit coordination for 3D underwater collective behaviors in a fish-inspired robot swarm”. In: *Science Robotics* 6.50 (Jan. 2021). Publisher: American Association for the Advancement of Science, eabd8668. DOI: 10.1126/scirobotics.abd8668. URL: https://www.science.org/doi/10.1126/scirobotics.abd8668 (visited on 03/08/2024).

[15] L. Stemmann and E. Boss. “Plankton and Particle Size and Packaging: From Determining Optical Properties to Driving the Biological Pump”. In: *Annual Review of Marine Science* 4.1 (2012). _eprint: https://doi.org/10.1146/annurev-marine-120710-100853, pp. 263–290. DOI: 10.1146/annurev-marine-120710-100853. URL: https://doi.org/10.1146/annurev-marine-120710-100853 (visited on 01/08/2024).

[16] W. H. Munk. “Abyssal recipes”. In: *Deep Sea Research and Oceanographic Abstracts* 13.4 (Aug. 1966), pp. 707–730. ISSN: 0011-7471. DOI: 10.1016/0011-7471(66)90602-4. URL: https://www.sciencedirect.com/science/article/pii/0011747166906024 (visited on 03/22/2025).

[17] E. Kunze et al. “Observations of Biologically Generated Turbulence in a Coastal Inlet”. In: *Science* 313.5794 (Sept. 2006). Publisher: American Association for the Advancement of Science, pp. 1768–1770. DOI: 10.1126/

science.1129378. URL: https://www.science.org/doi/full/10.1126/science.1129378 (visited on 11/14/2022).

[18] A. Visser. "Biomixing of the Oceans?" In: *Science (New York, N.Y.)* 316 (June 2007), pp. 838–9. DOI: 10.1126/science.1141272.

[19] M. Huntley and M. Zhou. "Influence of animals on turbulence in the sea". en. In: *Marine Ecology Progress Series* 273 (2004), pp. 65–79. ISSN: 0171-8630, 1616-1599. DOI: 10.3354/meps273065. URL: http://www.int-res.com/abstracts/meps/v273/p65-79/ (visited on 11/14/2022).

[20] W. Dewar et al. "Does the marine biosphere mix the ocean?" In: *Journal of Marine Research* 64 (July 2006). DOI: 10.1357/002224006778715720.

[21] M. M. Wilhelmus et al. "Effect of swarm configuration on fluid transport during vertical collective motion". en. In: *Bioinspiration & Biomimetics* 15.1 (Nov. 2019), p. 015002. ISSN: 1748-3190. DOI: 10.1088/1748-3190/ab435b. URL: https://iopscience.iop.org/article/10.1088/1748-3190/ab435b (visited on 01/19/2023).

[22] I. A. Houghton et al. "Vertically migrating swimmers generate aggregation-scale eddies in a stratified column". en. In: *Nature* 556.7702 (Apr. 2018). Number: 7702 Publisher: Nature Publishing Group, pp. 497–500. ISSN: 1476-4687. DOI: 10.1038/s41586-018-0044-z. URL: https://www.nature.com/articles/s41586-018-0044-z (visited on 08/10/2022).

[23] K. Bandara et al. "Two hundred years of zooplankton vertical migration research". en. In: *Biological Reviews* 96.4 (2021). _eprint: https://onlinelibrary.wiley.com/doi/pdf/10.11 pp. 1547–1589. ISSN: 1469-185X. DOI: 10.1111/brv.12715. URL: https://onlinelibrary.wiley.com/doi/abs/10.1111/brv.12715 (visited on 11/17/2022).

[24] B. Fernández Castro et al. "Intense upper ocean mixing due to large aggregations of spawning fish". en. In: *Nature Geoscience* 15.4 (Apr. 2022). Number: 4 Publisher: Nature Publishing Group, pp. 287–292. ISSN: 1752-0908. DOI: 10.1038/s41561-022-00916-3. URL: https://www.nature.com/articles/s41561-022-00916-3 (visited on 09/15/2023).

[25] D. D. Farmer, G. B. Crawford, and T. R. Osborn. "Temperature and velocity microstructure caused by swimming fish1". en. In: *Limnology and Oceanography* 32.4 (1987). _eprint: https://onlinelibrary.wiley.com/doi/pdf/10.4319/lo.1987.32.4.0978, pp. 978–983. ISSN: 1939-5590. DOI: 10.4319/lo.1987.32.4.0978. URL: https://onlinelibrary.wiley.com/doi/abs/10.4319/lo.1987.32.4.0978 (visited on 01/29/2024).

[26] M. C. Gregg and J. K. Horne. "Turbulence, Acoustic Backscatter, and Pelagic Nekton in Monterey Bay". EN. In: *Journal of Physical Oceanography* 39.5 (May 2009). Publisher: American Meteorological Society Section: Journal of Physical Oceanography, pp. 1097–1114. ISSN: 0022-3670, 1520-0485. DOI: 10.1175/2008JPO4033.1. URL: https://journals.ametsoc.

org/view/journals/phoc/39/5/2008jpo4033.1.xml (visited on 01/29/2024).

[27] S. Simoncelli, S. J. Thackeray, and D. J. Wain. "On biogenic turbulence production and mixing from vertically migrating zooplankton in lakes". en. In: *Aquatic Sciences* 80.4 (July 2018), p. 35. ISSN: 1420-9055. DOI: 10.1007/s00027-018-0586-z. URL: https://doi.org/10.1007/s00027-018-0586-z (visited on 09/15/2023).

[28] B. Cisewski et al. "Vertical Migration of Pelagic and Mesopelagic Scatterers From ADCP Backscatter Data in the Southern Norwegian Sea". English. In: *Frontiers in Marine Science* 7 (Jan. 2021). Publisher: Frontiers. ISSN: 2296-7745. DOI: 10.3389/fmars.2020.542386. URL: https://www.frontiersin.orghttps://www.frontiersin.org/journals/marine-science/articles/10.3389/fmars.2020.542386/full (visited on 04/29/2025).

[29] G. A. Tarling and S. E. Thorpe. "Oceanic swarms of Antarctic krill perform satiation sinking". In: *Proceedings of the Royal Society B: Biological Sciences* 284.1869 (Dec. 2017). Publisher: Royal Society, p. 20172015. DOI: 10.1098/rspb.2017.2015. URL: https://royalsocietypublishing-org.eu1.proxy.openathens.net/doi/10.1098/rspb.2017.2015 (visited on 05/15/2025).

[30] M. K. Fu and J. O. Dabiri. "Magnetic Signature of Vertically Migrating Aggregations in the Ocean". en. In: *Geophysical Research Letters* 50.5 (Mar. 2023), e2022GL101441. ISSN: 0094-8276, 1944-8007. DOI: 10.1029/2022GL101441. URL: https://agupubs.onlinelibrary.wiley.com/doi/10.1029/2022GL101441 (visited on 01/08/2024).

[31] G. V. Lauder and P. G. Madden. "Advances in Comparative Physiology from High-Speed Imaging of Animal and Fluid Motion". In: *Annual Review of Physiology* 70.1 (2008). _eprint: https://doi.org/10.1146/annurev.physiol.70.113006.100438, pp. 143–163. DOI: 10.1146/annurev.physiol.70.113006.100438. URL: https://doi.org/10.1146/annurev.physiol.70.113006.100438 (visited on 01/01/2024).

[32] J. O. Dabiri. "On the estimation of swimming and flying forces from wake measurements". In: *Journal of Experimental Biology* 208.18 (Sept. 2005), pp. 3519–3532. ISSN: 0022-0949. DOI: 10.1242/jeb.01813. URL: https://doi.org/10.1242/jeb.01813 (visited on 01/22/2024).

[33] N. J. Derr et al. "Reciprocal swimming at intermediate Reynolds number". en. In: *Journal of Fluid Mechanics* 952 (Dec. 2022). Publisher: Cambridge University Press, A8. ISSN: 0022-1120, 1469-7645. DOI: 10.1017/jfm.2022.873. URL: https://www.cambridge.org/core/journals/journal-of-fluid-mechanics/article/reciprocal-swimming-at-intermediate-reynolds-number/DB26C467722B4DE45441ACBB92FD34B3 (visited on 10/03/2023).

[34] T. Y. Wu. "Fish Swimming and Bird/Insect Flight". In: *Annual Review of Fluid Mechanics* 43.1 (2011). _eprint: https://doi.org/10.1146/annurev-fluid-122109-160648, pp. 25–58. DOI: 10.1146/annurev-fluid-122109-160648. URL: https://doi.org/10.1146/annurev-fluid-122109-160648 (visited on 01/22/2024).

[35] T. J. Pedley and S. J. Hill. "Large-amplitude undulatory fish swimming: fluid mechanics coupled to internal mechanics". In: *Journal of Experimental Biology* 202.23 (Dec. 1999), pp. 3431–3438. ISSN: 0022-0949. DOI: 10.1242/jeb.202.23.3431. URL: https://doi.org/10.1242/jeb.202.23.3431 (visited on 01/01/2024).

[36] J. D. Eldredge. "Numerical simulation of the fluid dynamics of 2D rigid body motion with the vortex particle method". In: *Journal of Computational Physics* 221.2 (Feb. 2007), pp. 626–648. ISSN: 0021-9991. DOI: 10.1016/j.jcp.2006.06.038. URL: https://www.sciencedirect.com/science/article/pii/S0021999106003093 (visited on 01/22/2024).

[37] A. Bajpayee and A. H. Techet. "Fast volume reconstruction for 3D PIV". en. In: *Experiments in Fluids* 58.8 (July 2017), p. 95. ISSN: 1432-1114. DOI: 10.1007/s00348-017-2373-3. URL: https://doi.org/10.1007/s00348-017-2373-3 (visited on 05/15/2025).

[38] Q. Gao, H. Wang, and G. Shen. "Review on development of volumetric particle image velocimetry". en. In: *Chinese Science Bulletin* 58.36 (Dec. 2013), pp. 4541–4556. ISSN: 1861-9541. DOI: 10.1007/s11434-013-6081-y. URL: https://doi.org/10.1007/s11434-013-6081-y (visited on 05/15/2025).

[39] D. Schanz, S. Gesemann, and A. Schröder. "Shake-The-Box: Lagrangian particle tracking at high particle image densities". en. In: *Experiments in Fluids* 57.5 (Apr. 2016), p. 70. ISSN: 1432-1114. DOI: 10.1007/s00348-016-2157-1. URL: https://doi.org/10.1007/s00348-016-2157-1 (visited on 05/15/2025).

[40] A. M. Lehn. "Volumetric analysis of lamprey hydrodynamics using synthetic aperture particle image velocimetry". eng. Accepted: 2019-07-18T20:31:00Z. Thesis. Massachusetts Institute of Technology, 2019. URL: https://dspace.mit.edu/handle/1721.1/121805 (visited on 05/15/2025).

[41] L. Mendelson and A. H. Techet. "Jumping archer fish exhibit multiple modes of fin–fin interaction". en. In: *Bioinspiration & Biomimetics* 16.1 (Nov. 2020). Publisher: IOP Publishing, p. 016006. ISSN: 1748-3190. DOI: 10.1088/1748-3190/abb78e. URL: https://dx.doi.org/10.1088/1748-3190/abb78e (visited on 05/15/2025).

[42] D. Murphy, D. Webster, and J. Yen. "A high-speed tomographic PIV system for measuring zooplanktonic flow". en. In: *Limnology and Oceanography: Methods* 10.12 (2012). _eprint: https://onlinelibrary.wiley.com/doi/pdf/10.4319/lom.2012.10.1096,

pp. 1096–1112. ISSN: 1541-5856. DOI: 10.4319/lom.2012.10.1096. URL: https://onlinelibrary.wiley.com/doi/abs/10.4319/lom.2012.10.1096 (visited on 05/15/2025).

[43] B. E. Flammang et al. "Volumetric imaging of fish locomotion". In: *Biology Letters* 7.5 (Apr. 2011). Publisher: Royal Society, pp. 695–698. DOI: 10.1098/rsbl.2011.0282. URL: https://royalsocietypublishing.org/doi/10.1098/rsbl.2011.0282 (visited on 10/24/2024).

[44] I. K. Bartol et al. "Volumetric flow imaging reveals the importance of vortex ring formation in squid swimming tail-first and arms-first". In: *Journal of Experimental Biology* 219.3 (Feb. 2016), pp. 392–403. ISSN: 0022-0949. DOI: 10.1242/jeb.129254. URL: https://doi.org/10.1242/jeb.129254 (visited on 05/15/2025).

[45] V. Stin et al. "Measuring the 3D wake of swimming snakes (Natrix tessellata) using volumetric particle image velocimetry". In: *Journal of Experimental Biology* 226.13 (July 2023), jeb245929. ISSN: 0022-0949. DOI: 10.1242/jeb.245929. URL: https://doi.org/10.1242/jeb.245929 (visited on 05/15/2025).

[46] D. Adhikari, M. Hallberg, and E. Longmire. "Simultaneous 3D PTV and infrared tomographic PIV measurement of zooplankton distribution in unsteady flow fields". en. In: (2013).

[47] N. Oyama, J. J. Molina, and R. Yamamoto. "Purely hydrodynamic origin for swarming of swimming particles". en. In: *Physical Review E* 93.4 (Apr. 2016), p. 043114. ISSN: 2470-0045, 2470-0053. DOI: 10.1103/PhysRevE.93.043114. URL: https://link.aps.org/doi/10.1103/PhysRevE.93.043114 (visited on 05/15/2025).

[48] J. Zhou, J.-H. Seo, and R. Mittal. "Effect of schooling on flow generated sounds from carangiform swimmers". en. In: *Bioinspiration & Biomimetics* 19.3 (Apr. 2024). Publisher: IOP Publishing, p. 036015. ISSN: 1748-3190. DOI: 10.1088/1748-3190/ad3a4e. URL: https://dx.doi.org/10.1088/1748-3190/ad3a4e (visited on 04/16/2024).

[49] Z.-M. Qian et al. "An effective and robust method for tracking multiple fish in video image based on fish head detection". In: *BMC Bioinformatics* 17.1 (June 2016), p. 251. ISSN: 1471-2105. DOI: 10.1186/s12859-016-1138-y. URL: https://doi.org/10.1186/s12859-016-1138-y (visited on 05/15/2025).

[50] A. Mathis et al. "DeepLabCut: markerless pose estimation of user-defined body parts with deep learning". en. In: *Nature Neuroscience* 21.9 (Sept. 2018). Publisher: Nature Publishing Group, pp. 1281–1289. ISSN: 1546-1726. DOI: 10.1038/s41593-018-0209-y. URL: https://www.nature.com/articles/s41593-018-0209-y (visited on 05/15/2025).

[51] J. Lauer et al. “Multi-animal pose estimation, identification and tracking with DeepLabCut”. en. In: *Nature Methods* 19.4 (Apr. 2022). Publisher: Nature Publishing Group, pp. 496–504. ISSN: 1548-7105. DOI: 10.1038/s41592-022-01443-0. URL: https://www.nature.com/articles/s41592-022-01443-0 (visited on 05/15/2025).

[52] Y.-L. Fan et al. “Exploring the use of deep learning models for accurate tracking of 3D zebrafish trajectories”. In: *Frontiers in Bioengineering and Biotechnology* 12 (Sept. 2024), p. 1461264. ISSN: 2296-4185. DOI: 10.3389/fbioe.2024.1461264. URL: https://www.ncbi.nlm.nih.gov/pmc/articles/PMC11463218/ (visited on 05/15/2025).

[53] A. Engel et al. “In situ three-dimensional video tracking of tagged individuals within site-attached social groups of coral-reef fish”. en. In: *Limnology and Oceanography: Methods* 19.9 (2021). _eprint: https://onlinelibrary.wiley.com/doi/pdf/10.1002/lom3. pp. 579–588. ISSN: 1541-5856. DOI: 10.1002/lom3.10444. URL: https://onlinelibrary.wiley.com/doi/abs/10.1002/lom3.10444 (visited on 05/15/2025).

[54] D. Adhikari et al. “Simultaneous measurement of 3D zooplankton trajectories and surrounding fluid velocity field in complex flows”. In: *Journal of Experimental Biology* 218.22 (Nov. 2015), pp. 3534–3540. ISSN: 0022-0949. DOI: 10.1242/jeb.121707. URL: https://doi.org/10.1242/jeb.121707 (visited on 05/15/2025).

[55] Y. Pan and G. V. Lauder. “Combining Computational Fluid Dynamics and Experimental Data to Understand Fish Schooling Behavior”. en. In: *Integrative And Comparative Biology* 64.3 (Sept. 2024), pp. 753–768. ISSN: 1540-7063, 1557-7023. DOI: 10.1093/icb/icae044. URL: https://academic.oup.com/icb/article/64/3/753/7676182 (visited on 10/17/2024).

[56] R. Ouillon et al. “Active swimmers interacting with stratified fluids during collective vertical migration”. en. In: *Journal of Fluid Mechanics* 902 (Nov. 2020). Publisher: Cambridge University Press, A23. ISSN: 0022-1120, 1469-7645. DOI: 10.1017/jfm.2020.618. URL: https://www.cambridge.org/core/journals/journal-of-fluid-mechanics/article/active-swimmers-interacting-with-stratified-fluids-during-collective-vertical-migration/A3A33B41129A9CDA92C7EB7CA808908C (visited on 03/17/2023).

[57] J. Johansen et al. “Kinematics and energetic benefits of schooling in the labriform fish, striped surfperch Embiotoca lateralis”. en. In: *Marine Ecology Progress Series* 420 (Dec. 2010), pp. 221–229. ISSN: 0171-8630, 1616-1599. DOI: 10.3354/meps08885. URL: http://www.int-res.com/abstracts/meps/v420/p221-229/ (visited on 05/14/2025).

[58] G. Van Stappen. *Manual on the Production and Use of Live Food for Aquaculture 4.1. Introduction, biology and ecology of Artemia*. Food and Agriculture

Organization of the United Nations, 1996. ISBN: 92-5-103934-8. URL: https://www.fao.org/4/w3732e/w3732e0m.htm (visited on 06/01/2025).

[59] A. E. Scofield, J. M. Watkins, and L. G. Rudstam. "Heterogeneity in zooplankton distributions and vertical migrations: Application of a laser optical plankton counter in offshore Lake Michigan". In: *Journal of Great Lakes Research* 46.4 (Aug. 2020), pp. 780–797. ISSN: 0380-1330. DOI: 10.1016/j.jglr.2020.01.005. URL: https://www.sciencedirect.com/science/article/pii/S0380133020300083 (visited on 06/01/2025).

[60] Z. Tao et al. "The diel vertical distribution and carbon biomass of the zooplankton community in the Caroline Seamount area of the western tropical Pacific Ocean". en. In: *Scientific Reports* 12.1 (Nov. 2022). Publisher: Nature Publishing Group, p. 18908. ISSN: 2045-2322. DOI: 10.1038/s41598-022-23522-0. URL: https://www.nature.com/articles/s41598-022-23522-0 (visited on 06/01/2025).

[61] N. Smirnov. "Table for Estimating the Goodness of Fit of Empirical Distributions". In: *The Annals of Mathematical Statistics* 19.2 (June 1948). Publisher: Institute of Mathematical Statistics, pp. 279–281. ISSN: 0003-4851, 2168-8990. DOI: 10.1214/aoms/1177730256. URL: https://projecteuclid.org/journals/annals-of-mathematical-statistics/volume-19/issue-2/Table-for-Estimating-the-Goodness-of-Fit-of-Empirical-Distributions/10.1214/aoms/1177730256.full (visited on 05/16/2025).

[62] J. Delcourt, N. W. F. Bode, and M. Denoël. "Collective Vortex Behaviors: Diversity, Proximate, and Ultimate Causes of Circular Animal Group Movements". en. In: *The Quarterly Review of Biology* 91.1 (Mar. 2016), pp. 1–24. ISSN: 0033-5770, 1539-7718. DOI: 10.1086/685301. URL: https://www.journals.uchicago.edu/doi/10.1086/685301 (visited on 05/16/2025).

[63] R. M. Alexander. "Buoyancy". en. In: *Locomotion of Animals*. Ed. by R. M. Alexander. Dordrecht: Springer Netherlands, 1982, pp. 39–53. ISBN: 978-94-011-6009-4. DOI: 10.1007/978-94-011-6009-4_3. URL: https://doi.org/10.1007/978-94-011-6009-4_3 (visited on 03/25/2025).

[64] A. G. Larson et al. "Inflation-induced motility for long-distance vertical migration". English. In: *Current Biology* 0.0 (Oct. 2024). Publisher: Elsevier. ISSN: 0960-9822. DOI: 10.1016/j.cub.2024.09.046. URL: https://www.cell.com/current-biology/abstract/S0960-9822(24)01287-9 (visited on 10/24/2024).

[65] C. Feucher, G. Maze, and H. Mercier. "Subtropical Mode Water and Permanent Pycnocline Properties in the World Ocean". en. In: *Journal of Geophysical Research: Oceans* 124.2 (2019). _eprint: https://onlinelibrary.wiley.com/doi/pdf/10.1029/2018JC pp. 1139–1154. ISSN: 2169-9291. DOI: 10.1029/2018JC014526. URL:

https://onlinelibrary.wiley.com/doi/abs/10.1029/2018JC014526 (visited on 03/25/2025).

[66] H. U. Sverdrup, M. W. Johnson, and R. H. Fleming. *The Oceans Their Physics, Chemistry, and General Biology*. New York: Prentice-Hall, 1942. URL: http://ark.cdlib.org/ark:/13030/kt167nb66r/ (visited on 03/25/2025).

[67] M. J. W. Rankine. "On the Mechanical Principles of the Action of Propellers". In: *Transactions of the Institution of Naval Architects* 6 (1865). URL: https://cir.nii.ac.jp/crid/1572824499691577600 (visited on 04/29/2025).

[68] B. Cisewski et al. "Seasonal variation of diel vertical migration of zooplankton from ADCP backscatter time series data in the Lazarev Sea, Antarctica". In: *Deep Sea Research Part I: Oceanographic Research Papers* 57.1 (Jan. 2010), pp. 78–94. ISSN: 0967-0637. DOI: 10.1016/j.dsr.2009.10.005. URL: https://www.sciencedirect.com/science/article/pii/S0967063709001976 (visited on 04/29/2025).

[69] M. M. Omand, D. K. Steinberg, and K. Stamieszkin. "Cloud shadows drive vertical migrations of deep-dwelling marine life". en. In: *Proceedings of the National Academy of Sciences* 118.32 (Aug. 2021), e2022977118. ISSN: 0027-8424, 1091-6490. DOI: 10.1073/pnas.2022977118. URL: https://pnas.org/doi/full/10.1073/pnas.2022977118 (visited on 04/29/2025).

[70] R. Pawlowicz. *Key Physical Variables in the Ocean: Temperature, Salinity, and Density*. en. Cg_cat: Key Physical Variables in the Ocean: Temperature, Salinity, and Density Cg_level: MED Cg_topic: Key Physical Variables in the Ocean: Temperature, Salinity, and Density. 2013. URL: https://www.nature.com/scitable/knowledge/library/key-physical-variables-in-the-ocean-temperature-102805293/ (visited on 05/14/2025).

[71] J. Davenport and A. Healy. "Relationship Between Medium Salinity, Body Density, Buoyancy and Swimming in Artemia franciscana Larvae: Constraints on Water Column Use?" en. In: *Hydrobiologia* 556.1 (Feb. 2006), pp. 295–301. ISSN: 1573-5117. DOI: 10.1007/s10750-005-9118-7. URL: https://doi.org/10.1007/s10750-005-9118-7 (visited on 06/02/2025).

[72] J. F. Brady and G. Bossis. "Stokesian Dynamics". In: *Annual Review of Fluid Mechanics* 20.1 (1988). _eprint: https://doi.org/10.1146/annurev.fl.20.010188.000551, pp. 111–157. DOI: 10.1146/annurev.fl.20.010188.000551. URL: https://doi.org/10.1146/annurev.fl.20.010188.000551 (visited on 11/03/2023).

[73] T. Ishikawa, M. P. Simmonds, and T. J. Pedley. "Hydrodynamic interaction of two swimming model micro-organisms". en. In: *Journal of Fluid Mechanics* 568 (Dec. 2006). Publisher: Cambridge University Press, pp. 119–160. ISSN: 1469-7645, 0022-1120. DOI: 10.1017/S0022112006002631. URL: https://www.cambridge.org/core/journals/journal-of-fluid-mechanics/article/hydrodynamic-interaction-of-two-swimming-model-microorganisms/B4C5A833548A87F4F4CDE74A7E3D3E4F (visited on 10/13/2023).

[74] D. O. Pushkin, H. Shum, and J. M. Yeomans. "Fluid transport by individual microswimmers". en. In: *Journal of Fluid Mechanics* 726 (July 2013). Publisher: Cambridge University Press, pp. 5–25. ISSN: 0022-1120, 1469-7645. DOI: 10.1017/jfm.2013.208. URL: https://www.cambridge.org/core/journals/journal-of-fluid-mechanics/article/fluid-transport-by-individual-microswimmers/B10922DDDCCFA74A67C523D25D6DFD2B (visited on 10/24/2023).

[75] E. Lauga and T. R. Powers. "The hydrodynamics of swimming microorganisms". en. In: *Reports on Progress in Physics* 72.9 (Sept. 2009), p. 096601. ISSN: 0034-4885, 1361-6633. DOI: 10.1088/0034-4885/72/9/096601. URL: https://iopscience.iop.org/article/10.1088/0034-4885/72/9/096601 (visited on 03/11/2024).

[76] D. Weihs. "The hydrodynamics of dolphin drafting". In: *Journal of Biology* 3.2 (May 2004), p. 8. ISSN: 1475-4924. DOI: 10.1186/jbiol2. URL: https://doi.org/10.1186/jbiol2 (visited on 10/14/2023).

[77] P. B. S. Lissaman. "Energy Effectiveness of Arbitrary Arrays of Wind Turbines". In: *Journal of Energy* 3.6 (1979). _eprint: https://doi.org/10.2514/3.62441, pp. 323–328. DOI: 10.2514/3.62441. URL: https://doi.org/10.2514/3.62441.

[78] A. Crespo, J. Hernández, and S. Frandsen. "Survey of modelling methods for wind turbine wakes and wind farms". en. In: *Wind Energy* 2.1 (1999). _eprint: https://onlinelibrary.wiley.com/doi/pdf/10.1002/%28SICI%291099-1824%28199901/03%292%3A1%3C1%3A%3AAID-WE16%3E3.0.CO%3B2-7, pp. 1–24. ISSN: 1099-1824. DOI: 10.1002/(SICI)1099-1824(199901/03)2:1<1::AID-WE16>3.0.CO;2-7. URL: https://onlinelibrary.wiley.com/doi/abs/10.1002/%28SICI%291099-1824%28199901/03%292%3A1%3C1%3A%3AAID-WE16%3E3.0.CO%3B2-7 (visited on 01/01/2024).

[79] I. Katic, J. Højstrup, and N. Jensen. "A Simple Model for Cluster Efficiency". In: 1987. URL: https://www.semanticscholar.org/paper/A-Simple-Model-for-Cluster-Efficiency-Katic-H%C3%B8jstrup/2cca97939f6f584994bc17ede0f06c957f7fb213 (visited on 01/01/2024).

[80] S. Voutsinas, K. Rados, and A. Zervos. "On the Analysis of Wake Effects in Wind Parks". In: *Wind Engineering* 14.4 (1990). Publisher: Sage Publications, Ltd., pp. 204–219. ISSN: 0309-524X. URL: https://www.jstor.org/stable/43749429 (visited on 01/01/2024).

[81] H. Zong and F. Porté-Agel. "A momentum-conserving wake superposition method for wind farm power prediction". en. In: *Journal of Fluid Mechanics* 889 (Apr. 2020), A8. ISSN: 0022-1120, 1469-7645. DOI: 10.1017/jfm.2020.77. URL: https://www.cambridge.org/core/product/identifier/S0022112020000774/type/journal_article (visited on 05/10/2022).

[82] P. Weber et al. "Optimal Flow Sensing for Schooling Swimmers". en. In: *Biomimetics* 5.1 (Mar. 2020). Number: 1 Publisher: Multidisciplinary Digital Publishing Institute, p. 10. ISSN: 2313-7673. DOI: 10.3390/biomimetics5010010. URL: https://www.mdpi.com/2313-7673/5/1/10 (visited on 01/23/2024).

[83] P. Oteiza et al. "A novel mechanism for mechanosensory-based rheotaxis in larval zebrafish". en. In: *Nature* 547.7664 (July 2017). Number: 7664 Publisher: Nature Publishing Group, pp. 445–448. ISSN: 1476-4687. DOI: 10.1038/nature23014. URL: https://www.nature.com/articles/nature23014 (visited on 01/23/2024).

[84] C. R. Shapiro, D. F. Gayme, and C. Meneveau. "Modelling yawed wind turbine wakes: a lifting line approach". en. In: *Journal of Fluid Mechanics* 841 (Apr. 2018), R1. ISSN: 0022-1120, 1469-7645. DOI: 10.1017/jfm.2018.75. URL: https://www.cambridge.org/core/product/identifier/S0022112018000757/type/journal_article (visited on 05/10/2022).

[85] E. Naudascher. "Flow in the wake of self-propelled bodies and related sources of turbulence". en. In: *Journal of Fluid Mechanics* 22.4 (Aug. 1965), pp. 625–656. ISSN: 1469-7645, 0022-1120. DOI: 10.1017/S0022112065001039. URL: https://www.cambridge.org/core/journals/journal-of-fluid-mechanics/article/flow-in-the-wake-of-selfpropelled-bodies-and-related-sources-of-turbulence/FE1C019D1BB226A7F046E4FED387F6FA (visited on 06/02/2025).

[86] A. I. Sirviente and V. C. Patel. "Wake of a Self-Propelled Body, Part 1: Momentumless Wake". en. In: *AIAA Journal* 38.4 (Apr. 2000), pp. 613–619. ISSN: 0001-1452, 1533-385X. DOI: 10.2514/2.1032. URL: https://arc.aiaa.org/doi/10.2514/2.1032 (visited on 06/02/2025).

[87] M. R. Arbie, U. Ehrenstein, and C. Eloy. "Stability of momentumless wakes". en. In: *Journal of Fluid Mechanics* 808 (Dec. 2016), pp. 316–336. ISSN: 0022-1120, 1469-7645. DOI: 10.1017/jfm.2016.645. URL: https://www.cambridge.org/core/product/identifier/S0022112016006455/type/journal_article (visited on 06/02/2025).

[88] C. Lalli and T. R. Parsons. *Biological Oceanography: An Introduction*. en. Google-Books-ID: c6J5hlcjFaAC. Elsevier, Apr. 1997. ISBN: 978-0-08-052799-4.

[89] J. Yen. "Life in transition: balancing inertial and viscous forces by planktonic copepods". eng. In: *The Biological Bulletin* 198.2 (Apr. 2000), pp. 213–224. ISSN: 0006-3185. DOI: 10.2307/1542525.

[90] K. B. Catton et al. "Quantitative analysis of tethered and free-swimming copepodid flow fields". In: *Journal of Experimental Biology* 210.2 (Jan. 2007), pp. 299–310. ISSN: 0022-0949. DOI: 10.1242/jeb.02633. URL: https://doi.org/10.1242/jeb.02633 (visited on 06/02/2025).

[91] D. W. Murphy, D. R. Webster, and J. Yen. "The hydrodynamics of hovering in Antarctic krill". en. In: *Limnology and Oceanography: Fluids and Environments* 3.1 (Feb. 2013), pp. 240–255. ISSN: 2157-3689, 2157-3689. DOI: 10.1215/21573689-2401713. URL: https://aslopubs.onlinelibrary.wiley.com/doi/10.1215/21573689-2401713 (visited on 06/02/2025).

[92] E. Kunze. "Biologically Generated Mixing in the Ocean". en. In: *Annual Review of Marine Science* 11.Volume 11, 2019 (Jan. 2019). Publisher: Annual Reviews, pp. 215–226. ISSN: 1941-1405, 1941-0611. DOI: 10.1146/annurev-marine-010318-095047. URL: https://www.annualreviews.org/content/journals/10.1146/annurev-marine-010318-095047 (visited on 06/02/2025).

[93] S. Nicol. "Living krill, zooplankton and experimental investigations: a discourse on the role of krill and their experimental study in marine ecology". In: *Marine and Freshwater Behaviour and Physiology* 36.4 (Dec. 2003). Publisher: Taylor & Francis _eprint: https://doi.org/10.1080/10236240310001614420, pp. 191–205. ISSN: 1023-6244. DOI: 10.1080/10236240310001614420. URL: https://doi.org/10.1080/10236240310001614420 (visited on 06/02/2025).

[94] W. M. Hamner et al. "Behavior of Antarctic Krill, *Euphausia superba:* Chemoreception, Feeding, Schooling, and Molting". en. In: *Science* 220.4595 (Apr. 1983), pp. 433–435. ISSN: 0036-8075, 1095-9203. DOI: 10.1126/science.220.4595.433. URL: https://www.science.org/doi/10.1126/science.220.4595.433 (visited on 06/02/2025).

[95] G. C. Hays. "A review of the adaptive significance and ecosystem consequences of zooplankton diel vertical migrations". en. In: *Hydrobiologia* 503.1 (Aug. 2003), pp. 163–170. ISSN: 1573-5117. DOI: 10.1023/B:HYDR.0000008476.23617.b0. URL: https://doi.org/10.1023/B:HYDR.0000008476.23617.b0 (visited on 01/01/2024).

[96] J. Ringelberg. *Diel Vertical Migration of Zooplankton in Lakes and Oceans: causal explanations and adaptive significances*. en. Google-Books-ID: vK-

MeiTu18p0C. Springer Science & Business Media, Dec. 2009. ISBN: 978-90-481-3093-1.

[97] J. Schindelin et al. “Fiji: an open-source platform for biological-image analysis”. en. In: *Nature Methods* 9.7 (July 2012). Number: 7 Publisher: Nature Publishing Group, pp. 676–682. ISSN: 1548-7105. DOI: 10.1038/nmeth.2019. URL: https://www.nature.com/articles/nmeth.2019 (visited on 01/19/2024).

[98] S. J. Husson. “Keeping track of worm trackers”. In: *WormBook* (Sept. 2012), pp. 1–17. ISSN: 15518507. DOI: 10.1895/wormbook.1.156.1. URL: http://www.wormbook.org/chapters/www_tracking/tracking.html (visited on 01/19/2024).

Appendix A

SUPPLEMENTARY MATERIALS FOR CHAPTER 1

Swimmers involved in vertical migration patterns are subject to varying degrees of light exposure and background flow, influenced by the presence of upstream swimmers that obstruct the light source and create wakes. However, brine shrimp consistently maintained swimming speeds irrespective of flow conditions and light intensities tested (figure A.1). Consequently, in subsequent simulations, swimmers were posited to maintain constant velocity.

Individual swimmer response to light intensity

A high-speed camera (Edgertronic SC1) was set up with a 20 cm x 25 cm (1024 pixel x 1280 pixel) field of view, 60 cm above the bottom of the tank. For each test, a recording was manually triggered once the first swimmer entered the camera field of view and captured for 30 seconds at 40 frames per second (fps). Four trials were carried out with each of the three filters (800, 1500, 2300 lumens per square meter (lux)), without a filter present (4000 lux), and without the target light (0 lux). An

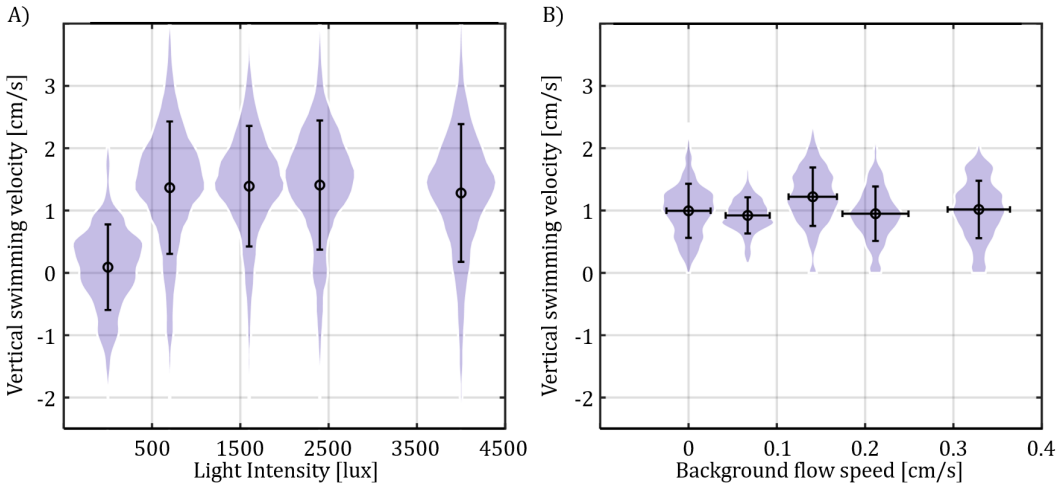

Figure A.1: Brine shrimp maintain a constant vertical velocity under varying environmental conditions. A) Distribution, mean and standard deviation of vertical swimming speed as a function of light intensity, measured in lux. The control condition, with only an infrared lamp (0 lux), is also shown for comparison. B) Distribution, mean and standard deviation of vertical swimming speed as a function of background flow. Horizontal error bars represent range of flows experienced.

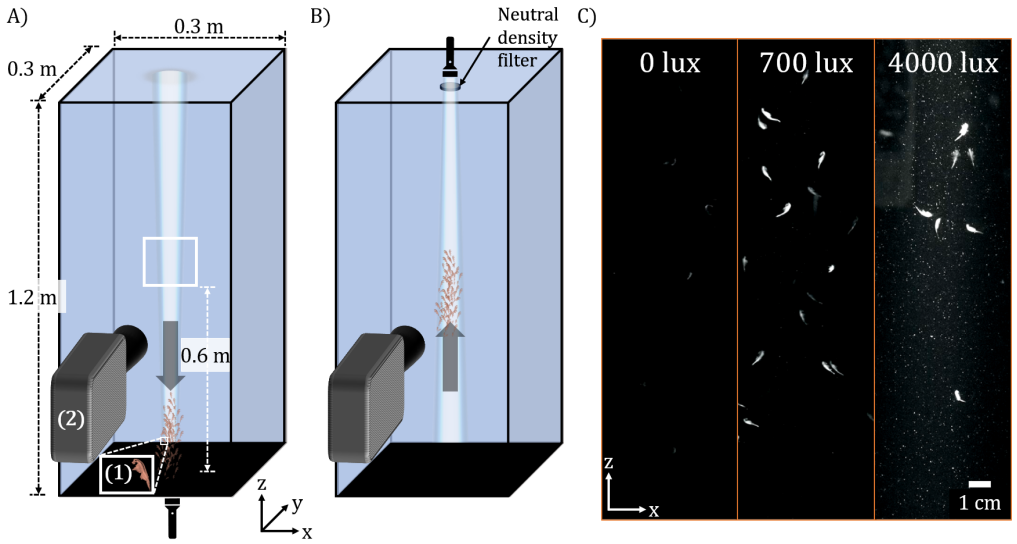

Figure A.2: Schematic of experimental protocol for characterization of phototactic response of brine shrimp. A) Brine shrimp (1) were gathered at the bottom of a 1.2 m tall tank using a flashlight positioned at the base. B) To induce vertical migration, the bottom flashlight was turned off, and the top flashlight was turned on. The light intensity of the top flashlight was varied using neutral density filters. Recording was manually initiated once the swimmers entered the field of view of the high-speed camera (2). C) Example frames from the x-z plane captured during vertical migrations under different light intensities, adjusted with neutral density filters. All trials were conducted with an infrared tank illuminator, which was used exclusively in the 0 lux condition. Three trials were performed for each light intensity: 0, 800, 1500, 2300, and 4000 lux.

infrared (850 nm) light was used to illuminate the tank and collect control data for the case in which no visible illumination was present. For consistency across all tests, this infrared illumination remained on for all tests.

Individual swimmer response to background flow

To simulate the vertical flows induced during collective vertical migration of brine shrimp, water was drained from a 2.4 m tall tank with a cross section of 0.5 m x 0.5 m, producing uniform flows in the range of 0.05-0.5 cm s^{-1} (figure A.3). These flow speeds correspond to those observed in vertical migrations of brine shrimp, with animal number densities between 100,000 and 600,000 animals per cubic meter [4]. The uniformity produced by this set-up reflects the uniform jet produced by steadily moving dilute swarms in discrete swimmer simulations [56].

Before testing, the tank was filled with 10 μm silver-coated glass spheres (CONDUCT-O-FIL, Potters Industries, Inc.) to facilitate imaging of the flow field with a laser

sheet. To confirm the quiescence of the tank, particle image velocimetry (PIV) was employed after introducing the animals with a 15 mL centrifuge tube. The tank was considered quiescent when the maximum time-averaged streamwise velocity was below 0.02 cm s^{-1}. Flow rate control was achieved using two series connected flow valves (1 in. NPT PVC Ball Valve), one for flow control and one for shut-off, and an inline flow meter (FLOMEC Flowmeter/Totalizer 5-50 gpm).

Once the tank was confirmed to be quiescent with PIV, a migration was induced with the same procedure explained in §2. A high-speed camera (Edgertronic SC1) was set up with a field of view of 21 cm x 26 cm (1024 pixel x 1280 pixel), 90 cm up from the bottom of the tank. Once the first swimmer entered the camera field of view, the shut-off valve was manually opened to initiate the flow, and the camera was manually triggered to record for 30 seconds at 15 fps. Three trials were carried out for each of the five target speeds: 0, 0.07, 0.14, 0.21 and 0.3 cm s^{-1}. The trials were carried out on different days using different animals, considering the limited number of trials achievable with the volume of the tank.

To identify potential sources of measurement uncertainty, two significant factors were addressed. First, before the onset of the flow, a streamwise velocity variation of 0.02 cm s^{-1} was allowed. Second, the flow speed was manually set using a ball valve and changed during each test due to variations in the height of the water column during draining. To address these uncertainties, an additional camera recorded flow rates displayed on the inline flow meter during each test. Both of these sources of variability were accounted for in the error bars of all flow measurements.

The captured videos of the vertical migration of brine shrimp were analysed using FIJI [97] and the wrMTrck plugin [98]. The resulting swimming trajectories were fitted in MATLAB with a smoothing spline algorithm, which minimizes a combination of squared residuals and curvature penalties utilizing cubic smoothing spline interpolation to fit a curve to the provided data points. A smoothing parameter of 0.95 (figure A.4) was selected to prioritize the reduction of oscillations, effectively smoothing out the fitted curve while preserving the overall trend of the data.

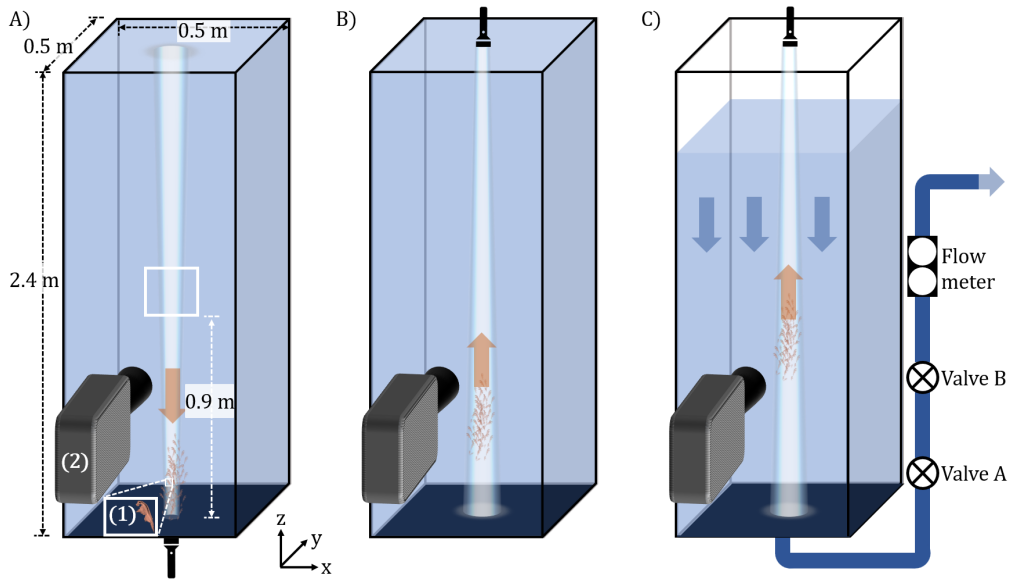

Figure A.3: Schematic of the experimental protocol for characterizing the flow response of brine shrimp. A) Brine shrimp (1) were initially gathered at the bottom of a 1.2 m tall tank using a flashlight positioned at the base. B) Brine shrimp (1) were initially gathered at the bottom of a 1.2 m tall tank using a flashlight positioned at the base. C) Once the swimmers entered the field of view of the high-speed camera (2), a flow valve was opened, introducing bulk flow in the opposite direction of the swimmers' motion. Recording was manually initiated at this point. The flow rate was controlled using a system of two flow valves and a flow meter arranged in series. Three trials were conducted for each target flow speed: 0, 0.07, 0.14, 0.21, and 0.3 cm s^{-1}.

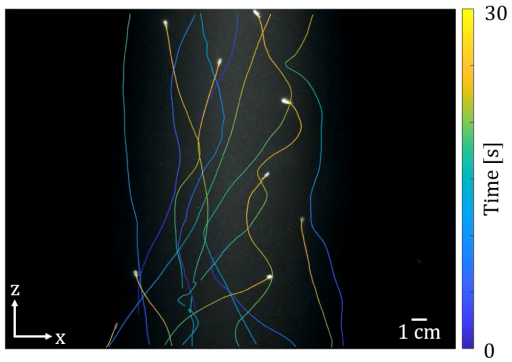

Figure A.4: Plot of brine shrimp swimming trajectories generated with ImageJ's wrMTrck plugin over a 30-second interval on top of the final frame in the image sequence. Colour transitions from blue to yellow represent progression in time, illustrating the trajectory of each swimmer within the tank. Brine shrimp present in the final frame can be identified as the white silhouettes at the end of the trajectories. Gradations in the background shading are due to the illumination used to induce phototaxis.